

# Faculty of Physics and Astronomy

University of Heidelberg

Diploma thesis  
in physics

submitted by  
Sebastian Hofferberth  
born in Herford

Heidelberg, 2004



# Experiments with ultracold atoms and Bose-Einstein condensates in microtraps near surfaces

This diploma thesis has been carried out by Sebastian Hofferberth at the  
Physikalisches Institut der Universität Heidelberg  
under the the supervision of  
Prof. Jörg Schmiedmayer.



## **Zusammenfassung**

### **Experimente mit ultrakalten Atomen und Bose-Einstein Kondensaten in Oberflächen-Mikrofallen**

Neutrale Atome sind ein vielversprechender Kandidat für die Realisierung eines vollständig kontrollierten Quantensystems. Das Konzept des *Atomchips* erlaubt das Fangen und Manipulieren von Atomen auf mikroskopischer Skala. In dieser Arbeit werden die ersten Atomchip-Experimente an einem neuen  $^{87}\text{Rb}$  Aufbau beschrieben. Es wurde ein Verfahren zur verlässlichen Produktion von Bose-Einstein Kondensaten (BEC) in Chip-basierten Fallen entwickelt. Darauf aufbauend wurden eine Reihe von Experimenten durchgeführt, welche den Einfluss von Oberflächen-Störpotentialen auf BECs untersuchen. Eine Verringerung störender Effekte um zwei Größenordnungen für lithographisch hergestellte Chips im Vergleich zu galvanischen Herstellungsmethoden wurde beobachtet. Erste Experimente mit einem Atom-Wellenleiter Interferometer werden vorgestellt, auf denen aufbauend Atom-Interferenz in Chipfallen realisiert werden kann.

## **Abstract**

### **Experiments with ultracold atoms and Bose-Einstein condensates in microtraps near surfaces**

Neutral atoms are a promising candidate for the realization of controlled quantum systems. The concept of the atom chip allows the trapping and manipulating of atoms on a microscopic scale. In this thesis the first atom chip experiments with a new  $^{87}\text{Rb}$  setup are presented. A procedure for the reliable production of Bose-Einstein condensates (BEC) in chip-based traps has been developed. Based on this a number of experiments studying the influence of surface disorder potentials on BECs were carried out. A reduction of disturbing effects by two orders of magnitude for a lithographic fabrication process over electroplating is found. First experiments with a guided matter wave interferometer potential are discussed that open the way to on-chip atom interferometry.



# Contents

<b>1</b>	<b>Introduction</b>	<b>1</b>
<b>2</b>	<b>Microscopic traps for neutral atoms</b>	<b>5</b>
2.1	Magnetic trapping of neutral atoms . . . . .	5
2.1.1	Atoms in magnetic fields . . . . .	6
2.1.2	Common trapping configurations . . . . .	7
2.2	Planar wire traps . . . . .	9
2.2.1	The side guide . . . . .	11
2.2.2	The U-trap . . . . .	13
2.2.3	The Z-trap . . . . .	13
2.2.4	Multi-wire guides . . . . .	15
2.3	The atom chip . . . . .	17
2.3.1	Chip fabrication . . . . .	18
2.3.2	Chip design . . . . .	20
2.3.3	Finite size effects . . . . .	22
<b>3</b>	<b>The experiment</b>	<b>25</b>
3.1	Experimental setup . . . . .	25
3.1.1	Experiment control . . . . .	25
3.1.2	Laser system . . . . .	26
3.1.3	Vacuum chamber . . . . .	28
3.1.4	Current carrying structures . . . . .	29
3.1.5	Imaging system . . . . .	31
3.2	Experimental procedure . . . . .	32
3.2.1	Magneto-optical trap . . . . .	33
3.2.2	Optical molasses . . . . .	37
3.2.3	Optical pumping . . . . .	37
3.2.4	Magnetic Cu-Z trap . . . . .	37
3.2.5	Chip experiments . . . . .	42
3.2.6	Imaging of the atom distribution . . . . .	43

<b>4</b>	<b>Bose-Einstein condensation in microtraps</b>	<b>47</b>
4.1	Bose-Einstein condensation in an external potential . . . . .	47
4.1.1	Effects of the confining potential . . . . .	48
4.1.2	The Gross-Pitaevskii equation . . . . .	48
4.1.3	The Thomas-Fermi approximation . . . . .	49
4.1.4	Observation of Bose-Einstein condensation . . . . .	50
4.2	BEC in the Cu-Z trap . . . . .	51
4.2.1	The trapping potential . . . . .	51
4.2.2	The evaporative cooling process . . . . .	51
4.2.3	Results . . . . .	54
4.3	Transfer to the chip . . . . .	54
4.3.1	The transfer procedure . . . . .	54
4.3.2	Adiabaticity of the transfer . . . . .	57
4.4	BEC in the $100\mu\text{m}$ -Z chip trap . . . . .	58
4.4.1	The potential . . . . .	58
4.4.2	Cooling and condensation . . . . .	59
4.5	BEC in the $10\mu\text{m}$ -wire chip trap . . . . .	61
4.5.1	The trapping geometry . . . . .	61
4.5.2	Trap loading . . . . .	63
4.5.3	Results . . . . .	64
<b>5</b>	<b>Fragmentation potentials</b>	<b>67</b>
5.1	Fragmentation observed in other experiments . . . . .	68
5.2	Atom distributions near the chip surface . . . . .	70
5.2.1	Imaging near reflecting surfaces . . . . .	71
5.2.2	Bias field strength determination . . . . .	72
5.2.3	Temperature measurement from in situ images . . . . .	72
5.3	Experiments with thermal atoms . . . . .	73
5.4	Experiments with BEC . . . . .	74
5.5	BEC as ultra-sensitive magnetic surface microscope . . . . .	77
<b>6</b>	<b>Atom chip interferometer</b>	<b>81</b>
6.1	Guided matter wave interferometer . . . . .	81
6.2	Implementation on our chip . . . . .	83
6.3	Present experimental status . . . . .	86
6.3.1	Potential testing with thermal atoms . . . . .	86
6.3.2	BEC in a guide . . . . .	89
<b>7</b>	<b>Summary and outlook</b>	<b>93</b>
	<b>Bibliography</b>	<b>97</b>



# 1 Introduction

Since its formulation in the early twentieth century, quantum mechanics has become the main building block of modern physics. It is now the basis of virtually all areas of physics and even neighboring disciplines like chemistry or molecular biology. Commonplace applications like semiconductor microchips or computer tomography have only become possible after quantum mechanics provided an understanding of the underlying physical systems.

The immense technological advance of the last decades, which was driven mainly by devices ultimately based on quantum mechanical effects, like for example lasers and superconductors, has in turn allowed the continuously more detailed study of a widening range of quantum systems. This increasing control over quantum systems leads towards an application of quantum mechanics on a wholly new level. So far applications of quantum mechanics typically only involve a rough level of control over a bulk sample containing enormous numbers of individual quantum systems, none of them directly accessible. For example, although the behavior of the above mentioned semiconductor microchips can be explained exclusively with quantum mechanics, in the operation of present computers only the collective effects of a huge number of quantum systems is exploited, with the individual constituent quantum systems, i.e. single atoms and electrons, being completely inaccessible. Current research works on isolating and studying ever smaller quantum mechanical systems, with the ultimate goal being the complete control over a single quantum system.

One possible application of such systems is *quantum information processing* (QIP). Here, individual quantum systems are used for storing information, with two quantum levels forming a system analogous to a classical bit. These *qubits* are processed by controlled interaction between different systems. It has been shown that the quantum nature of such systems allows the implementation of specific efficient *quantum algorithms* that cannot be realized on classical computers [31, 115, 52]. Hence, quantum computing will result in an immense increase of computation power at least in some cases. However, the true importance of QIP will be the possibility of simulating other quantum systems that cannot be isolated. The observation of the Mott insulator transition, a phenomenon known from solid state physics, in a quantum gas [48] is a first example of this approach. A wide range of candidate physical systems exists that may be suitable for manipulation on the quantum level. These include for example solid state superconductors, single photon optics, or trapped ions. Currently most advanced are nuclear magnetic resonance techniques using molecules in liquid solution, which

have already been used for basic quantum computation [23], and single photon optics, which has been used to implement first commercial devices for *quantum cryptography* [90], i.e. the quantum mechanical encoding and transmitting of information.

Neutral atoms are another promising candidate for controlled quantum manipulation, their main advantage being their inherently weak coupling to the uncontrolled environment. However, because of their relatively large mass, substantial cooling is required before their quantum nature becomes visible. This became possible with the invention of the magneto-optical trap (MOT) in 1986 [108], which lead to a rapid growth of the field of *quantum optics*. Within a few years the first observation of Bose-Einstein condensation (BEC) was reported [1, 26, 15], a phenomenon that had been predicted 70 years before [14]. Since then the study of this collective quantum mechanical effect, where a single quantum state (the trap ground state) becomes macroscopically populated because of the bosonic nature of the atoms, has been one of the main research areas of quantum optics [74]. A highly interesting aspect of neutral atoms is the possibility of tuning the inter-particle interaction at will, for example by means of Feshbach resonances [71]. This can be used for the controlled formation of cold molecules, which has recently lead to the first observation of molecular BEC [70, 49]. Of particular interest are (bosonic) molecules formed by fermionic atoms. By tuning the interaction strength one can adiabatically cross over from a molecular BEC to an ensemble of Cooper-pairs, which allows the study of the superfluid BCS (Bardeen-Cooper-Schrieffer) phase known from solid state superconductors [6, 66, 8]. This is another example of using an experimentally more accessible quantum system to simulate an analogous system in a completely different environment.

To use degenerate quantum gases of neutral atoms for QIP, ways have to be found of coherently manipulating and addressing atomic ensembles and ultimately single atoms. For this, a precise control over the position and the movement of the atoms is required. One possible approach are optical lattices, where the atoms are confined to potential wells formed by a standing light wave. In these systems first steps towards QIP have been realized, for example the collective controlled collision between atoms in neighboring potential wells [89]. A second possible realization, the use of miniaturized potentials generated by microfabricated elements integrated in a chip-like structure, is the topic of this thesis. Such *atom chips* allow the realization of non-periodic, built-to purpose potentials on a sub-micrometer scale. This approach has the potential to be as successful as integrated microscopical devices are in electronics and photonics.

The feasibility of the atom chip concept has been demonstrated by the on-chip creation of BEC [100, 55] and the controlled manipulation of atom movement with various chip structures like atomic conveyor belts, waveguides, and beam-splitters [109, 40]. Based on previous experiments, a new setup using  $^{87}\text{Rb}$  atoms was built in our group to continue the development of new atom chip components. This thesis describes the experiments carried out with this setup over the

last year.

In Chapter 2 the concept of magnetic microtraps will be discussed and specific trapping configurations used in our setup will be introduced. Also the layout of the atom chip currently used in the experiment will be presented.

The experimental procedure to produce ultra-cold atoms for chip experiments that is employed in our setup has been greatly simplified compared to prior realizations [126]. The different steps of the experiment and the experimental setup used to implement them are presented in Chapter 3. In the course of this thesis a number of experiments were carried out to characterize and optimize this procedure, the results of these experiments are also discussed in this chapter.

Chapter 4 describes the experiments carried out to create BECs in chip-based trapping potentials. Since its first realization we have improved the BEC creation process, and are now able to routinely produce BECs of  $N \approx 10^5$  atoms in various chip traps for use in further experiments.

To fully exhaust the capabilities of micromanipulating atoms with miniaturized structures, the distance between the chip surface and the trapped atoms has to be reduced to  $\sim 1\mu\text{m}$  and below. Only at such distances the potentials become sufficiently confining to allow a localization of atoms on the micrometer scale. Hence it is of great importance to understand any disturbing influences of the chip surface on the trapped atoms. The problematic effects observed so far, can be divided into two categories. On the one hand static deviations from the ideal potential shape have been observed that are attributed to fabrication imperfections of the chip structures, on the other hand potential fluctuations caused by technical and thermal noise in the atom chip can lead to unwanted coupling of the atoms to the surface. We have conducted experiments to study both types of effects in our setup. In this thesis, the static surface effects are covered (Chapter 5), while the noisy potentials will be discussed in [54]. We have found that the unwanted static effects caused by our atom chip are two orders of magnitude smaller compared to previous observations in other groups. In the course, it has turned out that BECs can be used as ultra-sensitive microscopic probes of subtle surface disorder effects.

One of the most interesting aspects of quantum mechanics is the wave nature of massive particles. The investigation and exploitation of atom interferometry is of great interest both for fundamental and applied research. The sensitivity of matter wave interferometers has been shown to be much better than that of light interferometers in several areas such as for example the measurement of inertial forces or rotations, making them useful tools in high-precision metrology [102, 53]. Beyond that atom interferometers may be used for tests of modern quantum gravitation theories and general relativity [117, 13]. The atom chip concept offers the realization of miniaturized, robust interferometers that can be integrated with other chip elements. In Chapter 6 we discuss the implementation of a guided matter wave interferometer [3] on our chip as well as first experiments carried out with this chip structure. In these preliminary steps we have

demonstrated the splitting and recombining of a propagating ensemble of thermal atoms, which lays the foundation for interference experiments with this setup. This thesis concludes with a summary of the obtained results and an outlook on future experiments that are now possible with our setup (Chapter 7).

## 2 Microscopic traps for neutral atoms

The trapping of neutral atoms is based on the interactions between inhomogeneous electromagnetic fields and an atomic multipole moment. These interactions are well-known as the Zeeman effect for magnetic and the Stark effect for electric fields. For trapping with static electric fields the atoms must have an electric dipole moment [34], which unperturbed neutral atoms do not have because of their inversion symmetry. Therefore electric traps require an induced dipole moment which can be produced by mixing states of opposite parity. This is for example done in optical traps by a nearly resonant laser beam. Electric trapping is also possible with dynamic fields, but this approach is impractical and unnecessary, because magnetic and optical traps with static fields provide a much easier solution.

Magnetic traps do not face the problem of electric traps, because most ground state atoms already have inherent magnetic dipole moments that can be used for trapping them magnetically. As a consequence the coupling of magnetic fields to the atoms is in general much stronger than for electric fields, because the electric coupling is a second order effect based on an induced dipole moment.

The experiments described in this thesis rely exclusively on magnetic trapping. In this chapter we will describe the mechanisms of this trapping method and introduce the most common trapping configurations (Section 2.1). We will then discuss the advantages of miniaturizing magnetic traps and will introduce some trap configurations that are suitable to be realized on a microscopic scale (Section 2.2). The implementation of such *micro-traps* in our experiment, the *atom chip*, will be described in Section 2.3.

### 2.1 Magnetic trapping of neutral atoms

The trapping of a particle always requires the transformation of kinetic energy into potential energy. In magnetic traps for neutral atoms this potential energy is stored as internal atomic energy. The atom experiences a shift of its internal levels based on the strength of the external field (Zeeman effect). An inhomogeneous field will thus create a spatially-varying potential able to confine the atoms.

The order of magnitude of the Zeeman effect and thus of the energy depth of magnetic traps is given by the Bohr magneton  $\mu_B = 9.27 \times 10^{-24} \text{J/T} = k_B \times$

670mK/T<sup>1</sup>. From this follows that to trap atoms with  $T = 1\text{K}$ , magnetic field variations of the order of 1T are required. Typical field variations in experiments are of the order  $10^0 - 10^2\text{G} = 10^{-4} - 10^{-2}\text{T}$  (the unit Gauss is better suited for these typical field strengths, hence we will express all magnetic fields in Gauss in this thesis), so that typical trap depth of realistic magnetic traps is of the order  $E = k_B \times 10^2\mu\text{K}$ . To magnetically trap atoms therefore substantial pre-cooling of a thermal atomic sample is required. In our case this is done in a magneto-optical trap (MOT) followed by an optical molasses (Chapter 3).

### 2.1.1 Atoms in magnetic fields

In the most general treatment of the interaction of neutral atoms with magnetic fields the internal structure of the atoms has to be taken into account. If the magnetic field varies on a length scale typical of the extension of the atom, the nucleus and the electrons have to be treated separately. This is the case for example when highly excited Rydberg-Atoms are placed in extremely inhomogeneous fields. Such systems have been studied in detail in [80, 82, 81].

For this treatment to become necessary, field gradients of  $\sim 10^9\text{G/cm}$  are needed. While micro-traps such as those used in our experiment offer the most extreme parameters available, the field gradients they produce are orders of magnitude below this regime.

In current experiments the atoms can hence be treated as point-like particles with total spin  $\mathbf{F}$  and the external field as a perturbation of the atomic states. The Zeeman energy is then given by

$$U_{mag} = -\mu_F \cdot \mathbf{B} = g_F \mu_B \mathbf{F} \cdot \mathbf{B}, \quad (2.1)$$

where  $\mu_F$  is the magnetic moment of the atom, and  $g_F$  the Landé factor of the atomic hyperfine state.

The atomic spin permanently precesses around the quantization axis given by the magnetic field with the Lamor frequency

$$\omega_{Lamor} = \frac{\mu \cdot \mathbf{B}}{\hbar}. \quad (2.2)$$

When the change of the direction of the magnetic field in the rest frame of the atom is small compared to this precession frequency,

$$\frac{d\mathbf{B}}{dt} < \omega_{Lamor} |\mathbf{B}|, \quad (2.3)$$

---

<sup>1</sup>Here  $k_B = 1.38 \times 10^{-23}\text{J/K}$  is Boltzmann's constant. In the context of trapped atoms it is convenient to express energy values in the form of temperatures. These two quantities are connected by the expression  $E = k_B T$ . We will use this convention throughout the whole text.

the spin *adiabatically* follows the magnetic field. In this case an approximation holds that treats the magnetic quantum number  $m_F$  of the atomic hyperfine state as a constant of motion. The potential then becomes proportional to the absolute value of the magnetic field

$$U = g_F \mu_B m_F |\mathbf{B}|. \quad (2.4)$$

The sign of the potential energy depends on the magnetic quantum number  $m_F$  and the according Landé factor  $g_F$ . The magnetic states can be categorized into two groups depending on the relative orientation of the magnetic moment to the external field, i.e. those with  $g_F m_F < 1$  and those with  $g_F m_F > 1$ <sup>2</sup>. Atoms in magnetic states belonging to the first group are drawn towards regions of maximum field strength (*high-field seekers*) while states belonging to the second group are drawn toward minima in the field strength (*low-field seekers*).

An application of the Earnshaw theorem [34], the so-called *Wing theorem* [128] shows that Maxwell's equations allow no field extrema in free space for (quasi)static fields. This theorem is a consequence of the fact that the divergence of the electromagnetic fields is zero in source free space. While this forbids maxima in the absolute magnetic field strength, the vector nature of the magnetic field still allows local minima in the absolute value of the field. Therefore it is only possible to create static trapping potentials with external fields for low-field seeking states.

Trapping of high-field seekers is also possible when there is a current inside the trapping area. This has been shown for atoms trapped on stable orbits around a current carrying wire [29]. For most experiments, including the ones described in this thesis, low field-seekers are used.

### 2.1.2 Common trapping configurations

As has been explained in the last section the design of a magnetic trap reduces to finding a field configuration whose modulus has a minimum. The resulting traps can be divided into two classes: those with vanishing magnetic field strength at the trap center and those with non-vanishing magnetic field everywhere [10]. These groups are known as *quadrupole-type* and *Ioffe-Pritchard-type* traps, respectively.

#### Quadrupole type traps

Magnetic field configurations with a field zero at their center usually can be approximated around the minimum by a linear function of the form

---

<sup>2</sup>In the case of  $^{87}\text{Rb}$  in the  $|5S_{1/2}, F=2\rangle$  which we use for magnetic trapping, we have  $g_F = 1/2$ , so that the magnetic states with  $m_F > 0$  are low-field seekers.

$$\mathbf{B} = (B'_x x, B'_y y, B'_z z). \quad (2.5)$$

The Maxwell equation  $\nabla \cdot \mathbf{B} = 0$  requires that  $B'_x + B'_y + B'_z = 0$ . This approximation basically means that only the usually dominant quadrupole term of a multipole expansion of the potential is considered. Although field configurations with zero field at the minimum exist, for which the quadrupole term vanishes, for example an ideal hexapole minimum, the term quadrupole trap is used in general for potentials with vanishing field at the center. An ideal quadrupole field can be realized for example with a pair of coils in ‘anti-Helmholtz’ configuration. Indeed this was the configuration used for the first magnetic trapping of neutral atoms [94].

Assuming that magnetic traps in general can be described by a power-law potential around the trap center, it is clear that the linear field offers the steepest possible gradients, leading to the strongest realizable confinement. Both this and the simple practical realization make this trap type appealing for experiments, but the field zero at the center turns out to be a problem which greatly reduces the usability of quadrupole fields for magnetic traps, unless specific care is taken. The adiabatic approximation is only valid when the condition given by Equation 2.3 is fulfilled. At a point with  $|\mathbf{B}| = 0$  this is not the case, because the Larmor frequency is zero. As a consequence, transitions between different magnetic states are possible, in particular atoms in low-field seeking states may be transferred to high-field seeking states, and thereby be ejected from the trap. Such transitions are known as *Majorana spin-flips* [88]. The quadrupole trap effectively has a hole at the field node through which atoms can escape from the trap. The resultant loss rate scales with the temperature as  $T^{-2}$  [25, 104], because colder atoms are confined closer to the center and thus spend more time close to the hole.

Various methods exist to ‘plug’ the hole to make the quadrupole field useful for magnetic traps, for example by using a dynamic magnetic field (*time-orbiting potential (TOP) trap*) [1] or a laser beam repelling atoms from the trap center [24]. An easier solution is to use trapping configurations that have non-zero field everywhere. The situation is different in magneto-optical traps. There, the vanishing field at the center is necessary for the MOT to work, as will be shown in Section 3.2.1. Hence quadrupole traps are present in all experiments that start with a MOT.

### Ioffe-Pritchard traps

The hole present in the quadrupole traps can be avoided by using trap configurations with nonzero field at the minimum. It is not possible to simply ‘lift’ the quadrupole potential without changing its shape. Instead the lowest-order potential that does not vanish at the minimum is of harmonic shape. In other words the closing of the hole at the trap center leads to less strongly confining traps.



A modification of the quadrupole trap that leads to a harmonic potential around the minimum was first proposed by Pritchard [107], based on the similar Ioffe configuration discussed decades earlier for plasma confinement [46]. Today the designation ‘Ioffe-Pritchard trap’ is used in general for traps that are harmonic around their center. Typically the potential becomes linear at a certain distance from the minimum. When a specific field component can be identified to provide the nonzero field at the center, this offset field is called the *Ioffe*-field.

A harmonic potential is fully described by its oscillation frequencies, which are given by the curvature of the field along the axes of the trap:

$$\omega_i = \sqrt{\frac{1}{m} \frac{d^2 U}{dx_i^2}} = \sqrt{\frac{\mu}{m} \frac{d^2 B}{dx_i^2}} \quad (2.6)$$

where  $m$  is the mass of the trapped atoms. These frequencies give an indication of both the steepness of the potential around the center and the size of the harmonic area. In many realizations of the Ioffe-Pritchard trap, including those in our experiment, two of the trapping frequencies are of roughly the same size (usually called the *transverse* frequencies  $\omega_t$ ), while the third (*longitudinal* frequency  $\omega_l$ ) is significantly smaller. This leads to a ‘cigar-shaped’ potential.

At points where the field strength is finite but small, a certain probability of a Majorana spin flip to a non-trapped state remains. For an harmonic potential the rate of such transitions can be calculated analytically [118, 47] and is given by:

$$\Gamma_M = 4\pi\omega_t \exp\left(-\frac{\omega_{Larmor}}{\omega_t}\right). \quad (2.7)$$

For realistic numbers ( $B = 0.1\text{G}$  and  $\omega_t = 2\pi 10^3\text{Hz}$ ) the flip rate is practically zero. Even small offset fields of the order of Milligauss are enough to prevent atom loss due to spin flips in typical traps. However, for extremely high compression (very large  $\omega_t$ ), as it may be realized in future microscopic traps, this effect will be the dominant lifetime limitation.

All magnetic confining potentials in our experiment are of the Ioffe-Pritchard type. The configuration we use to generate these traps will be discussed in the next section.

## 2.2 Planar wire traps

In most experiments the magnetic fields are generated by macroscopic current-carrying structures at distances of  $> 10\text{cm}$  from the trap center. To provide large field gradients at the trap center the field variation over the whole extension of the experiment area must be extremely strong. Creating traps with strong enough confinement for effective cooling requires large electric currents, resulting in high

power consumption and heat dissipation.

These problems can be alleviated by reducing the size of the setup. Bringing the field generating structures closer to the trap center reduces the area over which an inhomogeneous field must be created. The miniaturization of conventional three-dimensional setups consisting mainly of pairs of coils quickly reaches its limit. Small scale structures are difficult to manufacture and hamper the optical access to the experiment area.

Instead planar arrangements of current carrying wires can be used to create the trapping potentials [124]. Such a two dimensional system of wires mounted on an isolating surface is robust and can be easily miniaturized [110, 39]. It can be placed directly inside the vacuum chamber resulting in a distance of the trapped atoms to the wire of the order of  $1 - 100\mu\text{m}$ .

The restriction of the wire geometries to two dimensions does not reduce the complexity of the realizable potentials. Indeed, for the creation of simple traps a single wire suffices, as will be shown in this section. Arbitrarily complex potentials for the controlled manipulation of trapped atoms can be realized by multi-wire structures.

The motivation of miniaturizing such wire traps can be illustrated by looking at the magnetic field produced by a single infinitely long wire. A current flowing through the wire generates a circular field whose strength decreases with the distance from the wire:

$$\mathbf{B} = \frac{\mu_0 I}{2\pi r} \mathbf{e}_\varphi = 2 \cdot 10^{-7} \cdot \frac{I}{r} \mathbf{e}_\varphi \quad (2.8)$$

where  $I$  is the current through the wire,  $r$  the distance from the wire, and  $\mu_0 = 4\pi \times 10^{-7} \frac{\text{Vs}}{\text{Am}}$  is the magnetic field constant. The strength and gradient of the field are given by:

$$B(r) = \frac{\mu_0 I}{2\pi r} \quad (2.9)$$

$$\frac{dB(r)}{dr} = -\frac{\mu_0 I}{2\pi r^2} \quad (2.10)$$

It can be seen that both quantities are limited by the maximum current  $I_{max}$  the wire can sustain and the finite size  $2R$  of the wire. In particular, the maximum field gradient is proportional to the current density in the wire:

$$\frac{dB(r)}{dr} \propto \frac{I}{R^2} = j \quad (2.11)$$

Because of the quadratic dependence on the wire radius the most efficient way to increase the wire field gradient is to reduce the wire size. Hence miniaturization of the current-carrying structures leads to stronger confinement in the traps [124]. To simplify the required wire structures usually a hybrid approach is chosen to

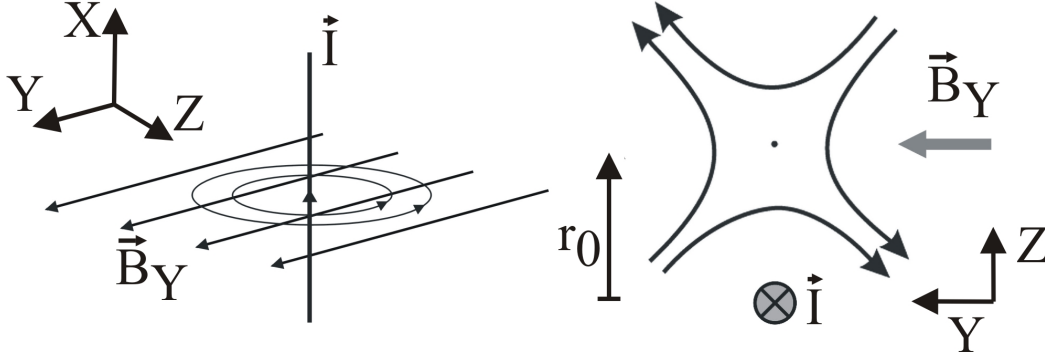


**Figure 2.1: Left:** A straight current and a homogeneous field form a two-dimensional magnetic trap. **Right:** The resulting magnetic field is a quadrupole field in the plane perpendicular to the wire. The trap center lies a distance  $r_0$  above the wire.

produce the magnetic traps. The inhomogeneous field of the wires are combined with external homogeneous fields, which are easily generated by pairs of coils in Helmholtz configuration. The advantage of strong confinement is not lost in this approach because the field gradients are determined by the inhomogeneous wire fields. Also because of the low currents in the wires the external fields usually need to be only of the order of a few Gauss, i.e. orders of magnitude smaller than for conventional setups, eliminating the problems of heating and power consumption such macroscopic experiments have.

In the following a number of wire traps are described that are relevant for our experiment. More exhaustive reviews of possible wire traps can be found in [40, 109].

### 2.2.1 The side guide

The simplest wire trap is the *side guide* [42]. It consists of a single straight wire and a homogeneous *bias* field  $B_b$  perpendicular to the wire as shown in Figure 2.1(left), creating a two-dimensional magnetic trap. The bias field cancels the wire field at a distance  $r_0$  from the wire:

$$r_0 = \frac{\mu_0}{2\pi} \frac{I}{B_b} \quad (2.12)$$

Around this trap center the combined field is a quadrupole field in the plane perpendicular to the wire (Figure 2.1(right)). The radial field gradient is given by

$$\left. \frac{dB}{dr} \right|_{r_0} = \frac{B_b}{r_0} = \frac{2\pi}{\mu_0} \frac{B_b^2}{I} \quad (2.13)$$

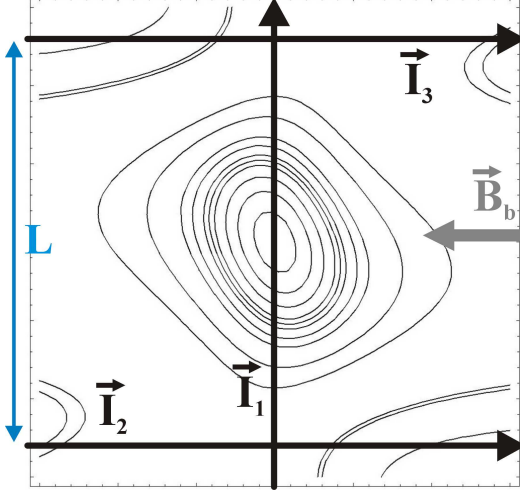


**Figure 2.2:** By adding two wires perpendicular to the side guide, a three-dimensional trap is created. The trap type depends on the orientation of the currents in the two new wires. Here the case of parallel currents is shown, which results in a point-symmetric Ioffe-Pritchard type trap.

The fact that the steepness of the trap increases with smaller current on first sight seems to be in contradiction to Equation 2.11, which states that the wire field gradient decreases with decreasing  $I$ . But a reduction of the current (while  $B_b$  is unchanged) also leads to a smaller distance  $r_0$  of the trap center to the wire. Because of the quadratic dependence on  $r$  in Equation 2.11, this increases the wire field gradient despite the smaller current.

Adding a homogeneous field parallel to the wire lifts the field minimum to a finite value without destroying the trapping geometry. In that case the side guide becomes a Ioffe-Pritchard type trap that is characterized by the curvature of the field at the trap center:

$$\left. \frac{d^2 B}{dr^2} \right|_{r_0} = \left( \frac{2\pi}{\mu_0} \right)^2 \frac{B_b^4}{B_0 I^2} = \frac{B_b^2}{r_0^2 B_0}, \quad (2.14)$$

where  $B_0$  is the magnetic field strength at the minimum. Because the field does not change in the direction parallel to the wire the atoms are trapped only in two dimensions. The side guide can be used as wave guide for neutral atoms [29, 28]. A three-dimensional trap can be created by adding two more wires, parallel to each other at a distance  $L$  and perpendicular to the original wire, so that a H-structure is formed (Figure 2.2). The new wires create a field component parallel to the original wire, which closes the open ends of the side guide.

Depending on the direction of the currents in the two new wires, a quadrupole or a Ioffe-Pritchard type trap is formed. When the currents run in opposite directions, a point exists where all fields cancel, so that a quadrupole trap is formed. When the currents run in the same direction, no point with zero magnetic field exists, so that a point symmetric Ioffe-Pritchard trap is formed. The scaling behavior of both the trap height and gradients do not change significantly in both cases. In many situations the basic behavior of a wire trap can be understood by considering the side guide case.

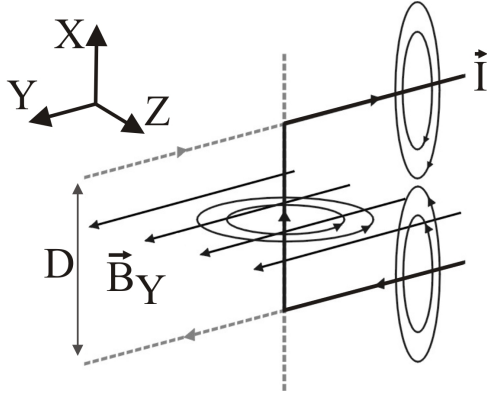


**Figure 2.3:** A single wire bend into a U-shape can replace the three-wire H-structure with opposite currents in the outer wires. Together with a homogeneous field this configuration creates a magnetic quadrupole trap.

### 2.2.2 The U-trap

The H-trap can be simplified without changing its general behavior. The three wires forming the trap are replaced by a single wire bent either in a U- or Z-shape. The advantage of this simplification is that no crossing of different wires is required, which would prevent the wire geometry to be truly two-dimensional. The U-shaped single wire replaces the H-structure with opposite currents in the outer wires (Figure 2.3). The missing parts of the outer wires do not change the general behavior of these wires. They provide a field component parallel to the central part of the wire (in the x-direction in the figure) which has a maximum above each of the outer wires, while it vanishes in the center, thus providing the potential well in the longitudinal direction. Since the outer wires do not contribute to the field component in the direction of the external bias field, the potential shape in the direction perpendicular to the wire plane is not significantly altered compared to the side guide.

A shift of the trap center away from its position above the central bar happens because of the field in z-direction produced by the outer wires. This field component must be canceled by the central wire which happens only on one side of this wire. Hence the trap center must lie in the half space not containing the outer wires. An external homogeneous field in z-direction can be added to undo this effect and move the center back above the middle wire.

In our experiment we use such a U-wire configuration to create the quadrupole field for the magneto-optical trap (Section 3.2.1), for which such a field type is required. For purely magnetic trapping the U-trap is not suitable because of the Majorana losses due to the field zero. Instead another trapping configuration, the Z-trap, is used.

### 2.2.3 The Z-trap

The H-trap with parallel currents in the outer wires can be replaced by a single Z-shaped wire (Figure 2.4(left)). In this configuration the x-components of the magnetic fields created by the outer wires are always parallel, which means

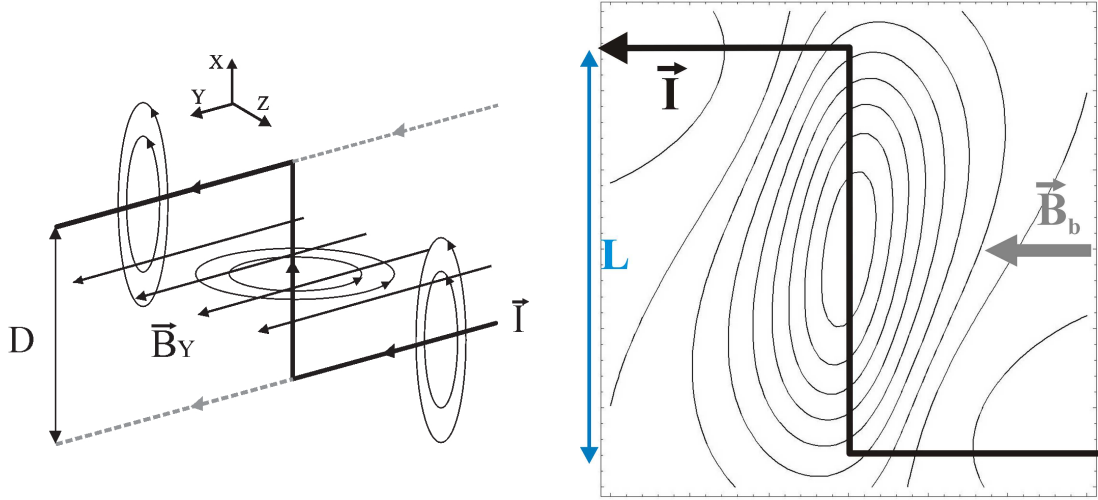


**Figure 2.4:** **Left:** A Z-shaped wire and a homogeneous field perpendicular to the central wire create a trapping potential analogous to a H-structure with parallel currents in the outer wires. **Right:** Top view of the Z-trap, the contours show the strength of the magnetic field in a plane above the wire structure. It can be seen that the trap center lies directly above the central wire, but is tilted because of the asymmetry in the outer wires.

$|\mathbf{B}| > 0$  everywhere. Thus the Z-trap is of the Ioffe-Pritchard type with the Ioffe field being generated by the outer parts of the wire. This Ioffe field causes the shape of the potential at the center to be harmonic.

The trap center automatically lies directly above the central wire, because of the symmetry of the configuration (Figure 2.4(right)). The trap height in z-direction is mainly determined by the bias field, as was described for the side guide (Equation 2.12).

The *trap bottom*, the field strength  $B_0$  at the trap center, is determined by the x-component of the wire field. It can be altered by adding a x-component to the external homogeneous field in the opposite direction to the wire field. By partially cancelling the Ioffe field of the wire, the trap bottom can be lowered, up to the point where it vanishes when the fields cancel completely. In that case the trap becomes a quadrupole trap. This tunable transition allows to change the size of the harmonic area of the potential, which plays an important role during evaporative cooling, which is explained in Section 3.2.4.

The trap frequencies of the potential are given by the curvature of the field along its principal axes, which do not fall together with the axes defined by the wire, but are rotated slightly around the z-axis (this is due to the fact that the Z-wire is only point symmetric). Therefore to calculate the trap frequencies the Hessian of the potential has to be diagonalized. This calculation is for example carried out in [114]. In the two transverse directions (perpendicular to the central wire) the confinement of the Z-trap is similar to the side guide. The transverse frequencies diverge for small distances of the trap to the central wire. The longitudinal

(parallel to the central wire) frequency instead approaches zero when the trap distance is reduced. This is caused by the vanishing x-component of the outer wire field close to the wire plane. Because of this the aspect ratio of the trapping potential will become more extreme with closer distance to the wire, resulting in highly elongated traps.

In our experiment the Z-trap is the trapping geometry used for initial trapping and cooling of the atoms. Z-structures of different sizes exist both on and underneath the atom chip (Sections 2.3.2 and 3.1.4).

### 2.2.4 Multi-wire guides

Next to potentials confining the atoms in a single minimum, geometries are of interest that can be used to guide the atoms along controlled paths. This allows for example the transport of the trapped atom cloud between spatially separated traps. The ability to move the atoms to different sites of the planar wire structure greatly increases the usability of such devices.

The side guide described in Section 2.2.1 is the simplest realization of such a guiding potential. It suffers from the limitation of allowing guiding along straight paths only, because the external bias field must always be perpendicular to the wire. This problem can be solved by using more complex guides consisting of multiple wires [87, 17].

For such two-dimensional traps a formalism exists that allows a systematic description of the trap geometry for any number of wires [27]. Applications of this formalism and an extensive treatment of guiding potentials can be found in [44, 75]. Here only two guiding schemes directly relevant for the experiments described in this thesis are covered.

#### Two-wire guide

A guide which does not suffer from the limitation of the side guide, but which instead can be of arbitrary shape, can be realized by two parallel wires with counter-propagating equal currents and a bias field perpendicular to the wire plane [87].

In the central plane between the wires the field component parallel to the wire plane vanishes, because both wires exactly compensate each other. The field component perpendicular to the wire plane instead points in the same direction for both wires. When this component is now compensated by the external bias field a line of zero field along the guide is created. Since the field in the center plane consists only of a component perpendicular to the wire plane, the resulting guide is independent of the orientation of the wires in this plane.

It should be noted that for too large bias field the trap can be overcompensated. When the bias field is increased the field minimum moves closer to and finally into the wire plane. For bias fields even stronger than this critical value, two separate

minima in the wire plane exist. In this case the two wires form independent side guides.

The potential suffers from the same problem as all traps with zero field strength at the minimum: the trap lifetime is limited by Majorana losses. For a straight two-wire guide this problem can be solved by adding a homogeneous field parallel to the wire, but this is not possible for a curved guide. The Ioffe field would have to point parallel to the guide at all points in space, which is in general not realizable with an external Ioffe field for a guide of arbitrary shape. A solution to this problem is proposed in [17], which suggests using periodically varying currents in the two wires. This modulation leads to the field zero permanently rotating about the center of the guide on a (nearly) circular orbit, similar to TOP-traps whose feasibility has already been demonstrated experimentally [1]. Atoms cold enough to be confined within the radius of this rotation see a time averaged potential of harmonic shape whose field strength always remains finite. This scheme allows the smooth transport of cold thermal atoms and even BECs in guides of arbitrary shape.

The static two-wire guide has been thoroughly tested in previous experiments in our group carried out with lithium atoms [87]. Because of the relatively hot temperature of the atoms Majorana losses were negligible in those experiments. The atoms were guided along a spiral-shaped path of total length 25mm, showing the feasibility of multi-directional two-wire guides. The dynamic potential applied to BEC guiding remains to be shown.

### Four-wire guide

The combination of two guides of the kind described in the last paragraph allows the creation of a splitting potential which can be used to divide an atom ensemble moving along the guide. This is illustrated in Figure 2.5. Two guides are placed next to each other, resulting in four parallel wires with alternating currents. At a certain point the wires split up into two separate two-wire guides, creating two identical arms into which the guided atoms can pass.

What kind of guide is formed by the four parallel wires depends on the strength of the bias field. Based on the number and the position of the resulting minima, different regimes can be defined. A detailed derivation can be found in [44]. The current in and the (fixed) distance between the wires define a critical value for the bias field. For field strengths above this value two horizontally separated minima exist. In essence, in this regime the wires act as two parallel two-wire guides which slightly modify each others potential. When the bias field strength is smaller than the critical value, the four wires form a single guide. In that case two minima exist which lie on a vertical line through the center of the four wire structure. The potential around these minima is not identical. Because of the proximity to the wires the lower guide is more tightly confining. In the case of the bias field being equal to the critical value, the minima fall together, forming



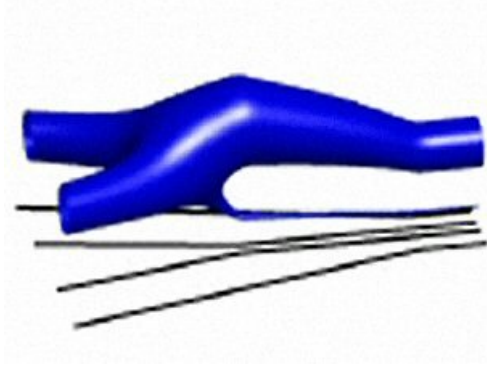


**Figure 2.5:** Beam splitter formed by four wires. The black lines represent the wire layout, the guide formed by four parallel wires is split into separate two-wire guides. The contour plot shows a representative equipotential surface for the experimentally relevant case of  $B_{bias} < B_{crit}$  (see text). The two vertically separated incoming minima can be seen, with the lower one clearly being more tightly confined. These minima merge at the point where the wires split and then evolve into two symmetric horizontally separated minima.

a single hexapole potential minimum along the guide.

Although the case of a single incoming channel would be favorable, its experimental realization requires a very accurately stabilized bias field to avoid the uncontrolled splitting of the guided atom cloud due to field fluctuations. To circumvent this problem one can work in the regime of vertically separated minima, with only the upper guide being used as input channel. However, the unused input channel may disturb the splitting process because it now basically acts as a third output channel, leading to undesirable atom loss in the actual output guides.

The problem of Majorana losses due to zero fields along the guide minima can be solved by a homogeneous field parallel to the four wires again only for the case of small splitting angles. It is important to note that such a field does not destroy the symmetry of the beam splitter arms, which is required to guarantee equal splitting of an atom cloud.

A four-wire guide is used in our experiment to form the main interferometer potential on the atom chip. The combination of two Y-shaped beam splitters creates a potential which first splits and then recombines an atom cloud moving along the guide (see Section 2.3.2 for the implementation and Chapter 6 for the actual experiments carried out with this structure).

## 2.3 The atom chip

To miniaturize wire structures as those described in the previous section to micrometer size, fabrication techniques known from semiconductor microchip production can be used. This allows to create arrangements of current-carrying wires mounted on an isolating semiconductor wafer. Because of this close similarity to standard microchips these structures are called *atom chips* [39].

The minimal size of the wire structures is given by the current resolution limit of nanofabrication technology, which already lies below 100nm. This makes extremely confined traps with ground state sizes  $< 10\text{nm}$  possible. Such precise

localization of the atoms allows the exact addressing of individual sites on the atom chip for manipulation of small numbers of atoms down to single atom operations required for quantum information processing.

The atom chip concept also opens the possibility of integrating other tools of atom manipulation in addition to electromagnets. The addition of electric fields to modify magnetic traps has already been demonstrated in our group [76], while the addition of permanent magnets has been carried out in other groups [113, 122]. Also promising is the combination of magnetic traps with micro-optical elements, such as fibers or micro-lenses, on the chip [12]. Light can be used to create optical micro-traps or wave guides [7, 50] which can be loaded from magnetic micro-traps. Integrated micro-cavities are already being tested in our and other groups [127, 65, 85], they promise the ability of non-destructive single-atom detection on future chips [67].

### 2.3.1 Chip fabrication

The chips used in our group are produced at the microfabrication center of the Weizmann Institute of Science, Rehovot. The chips consist of multiple layers, deposited on a substrate in a multi-stage process.

The substrate material used for our chips is silicon, because it offers good heat conductivity. Standard wafers for microchip production with a thickness of 0.6mm are used. As silicon tends to leak currents, especially in the presence of light, the substrate is factory covered with a thin (40nm) isolating layer of  $\text{SiO}_2$ .

Onto this a 40nm titanium adhesion layer is evaporated before the final conducting layer is applied. The material of choice for the conducting layer is gold, which offers low electric resistance and good fabrication properties. The wire structures are defined by 1 – 10 $\mu\text{m}$  thick grooves in the titanium and gold layers. To produce these grooves the chip is first covered completely with a layer of image reversal photoresist and is then exposed to ultraviolet light shined through an electron beam patterned mask that blocks the light in the areas of the future grooves. In a standard development procedure the photo resist is removed in the areas where it was exposed to the ultraviolet light, while it is left in place in the areas of the future grooves. After the evaporation of the titanium and gold layers the remaining resist is removed in a chemical bath, leaving the desired free spaces between the gold wires.

The thickness of the gold layer is limited due to the evaporation process to  $< 3\mu\text{m}$ . Thicker wires can be created by repeating the production process with a second mask to deposition a second gold layer onto the first. Typical wire widths on currently used chips range from 1 to 100 $\mu\text{m}$ , with fabrication errors of the order of 100nm. The grain size in the evaporated gold layer is 50 – 80nm.

Figure 2.6 shows microscope images of chips produced with the lithography technique described above. For comparison images of chips produced with the alterna-

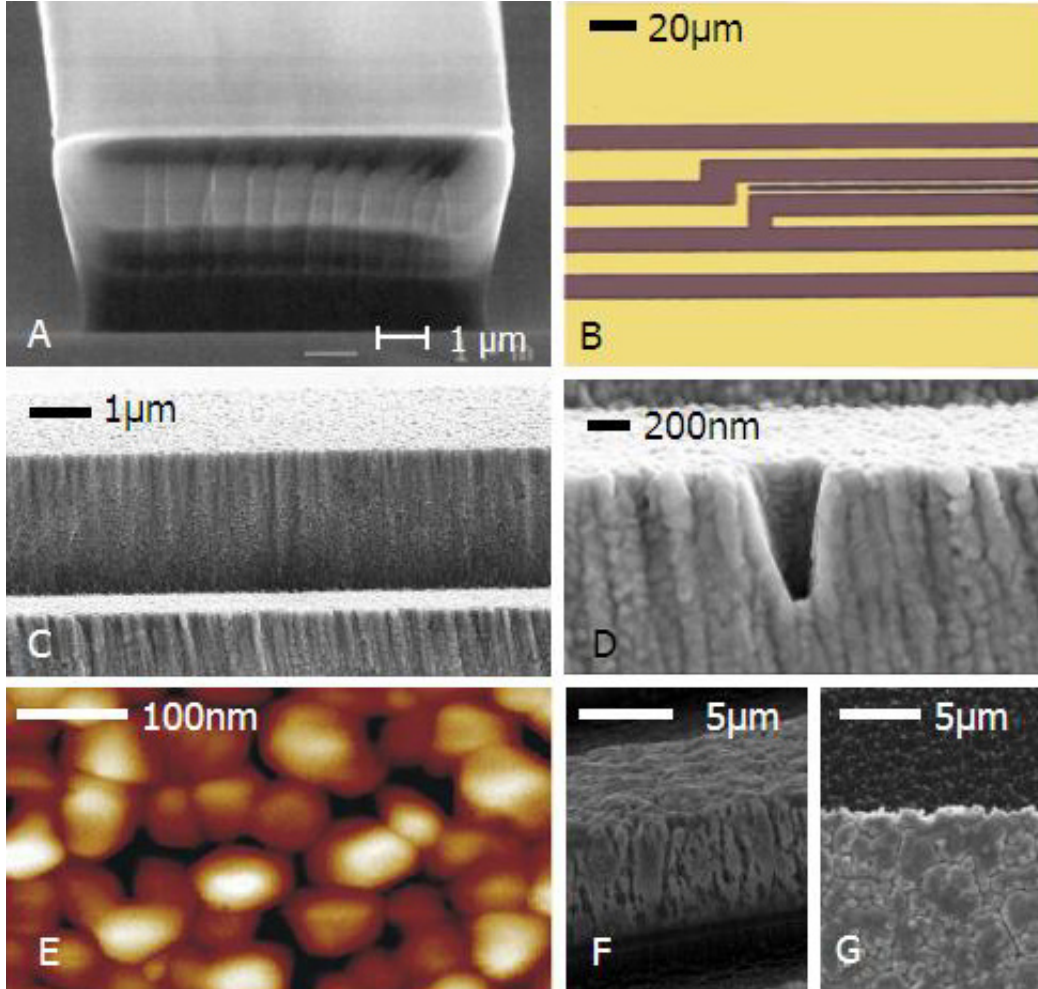


**Figure 2.6:** Microscope images of chip details during and after the fabrication. (A) Scanning microscope (SEM) image of the photoresist defining a future groove on the chip. (B) Light microscope image of a detail of a fully produced chip. The gold wires have widths of 1, 5, 10 μm. (C) SEM image of a double layer wire. The top layer wire is smaller in width, hence a step is visible. (D) SEM image of a rare defect in the wire edge. Typically, edge and surface roughness are both < 100 nm. (E) Atomic force microscope (AFM) image of the gold surface. The grainsize is 50 – 80 nm. (F) For comparison, the surface of an electroplated wire exhibits roughness on a much larger scale (SEM image). (G) Same wire viewed from the top. F and G taken from [37].

tive technique of *electroplating* are shown. Clearly our chip wires exhibit smoother surfaces than wires produced with such electro-chemical methods [32, 41, 83]. The electrical and thermal properties of our atom chips are extensively studied in [51].

### 2.3.2 Chip design

The chip currently in use in our experimental setup was designed with the goal of observing atom interference in chip-based traps. Hence a number of wire arrangements suitable for interferometer experiments can be found on the chip. This chip was produced with a double gold layer to increase the wire thickness. For the top layer a mask was used in which all wire widths have been reduced by  $2\mu\text{m}$ , to guarantee the avoidance of misplacement of the mask on top of the first layer. The use of a different mask also allows to selectively leave out wires onto which a second layer is applied. This makes it possible to increase the height of wide structures, while for the narrow wires 'tower'-like structures with greater height than width can be avoided. The thickness of the gold layers is  $1.3\mu\text{m}$  (bottom) and  $1.8\mu\text{m}$  (top). The increase of the wire height increases the maximal currents through the wires that can be used safely in the experiments. The whole center region of the chip design containing all relevant parts for the experiments is shown in Figure 2.7. The letter designations used in the figure and in the following text correspond to the labels used in the laboratory.

The largest structures on the chip are two Z-shaped wires of  $100\mu\text{m}$  (T - H) and  $50\mu\text{m}$  (U - H) width. The Z-trap (Section 2.2.3) created by the  $100\mu\text{m}$ -wire ( $100\mu\text{m}$ -trap) plays a central role in many of the experiments described in this thesis. It serves as the initial trap from which atoms are then transferred to other chip potentials. Also many experiments were carried out directly in this trap (Section 4.4).

Four parallel wires of  $10\mu\text{m}$  width (X, Y, Z, G) are situated next to the Z-wires. These wires form a four-wire guide of the type discussed in Section 2.2.4, containing a splitting and recombining region consisting of two Y-beam splitters, which functions as an interferometer for guided atoms (Chapter 6). There are two structures perpendicular to the four wires at the splitting region, a U-shaped wire (V - W) and a single electrode (a). These can be used to provide a magnetic and/or electric potential to break the symmetry of the two interferometer paths. The two outer wires of the four-wire guide can be used individually (X - G or Z - G) to form an L-shaped wire. In combination with one of the  $20\mu\text{m}$  wide U-shaped wires (A - B) this creates a Z-trap like confining potential ( $10\mu\text{m}$ -wire trap), which we have used extensively in the surface experiments described in Chapter 5. The four U-shaped wires (A, B, C, D, E, F) can in general be used to provide confining or pushing fields for potentials formed by the four  $10\mu\text{m}$  wires. There are two more wire structures which form interferometers on the chip, but they have not been used so far. The  $10\mu\text{m}$ -Z (S - J) next to the  $100\mu\text{m}$ -Z has a smaller, also Z-shaped, substructure at the center with which a time-dependent

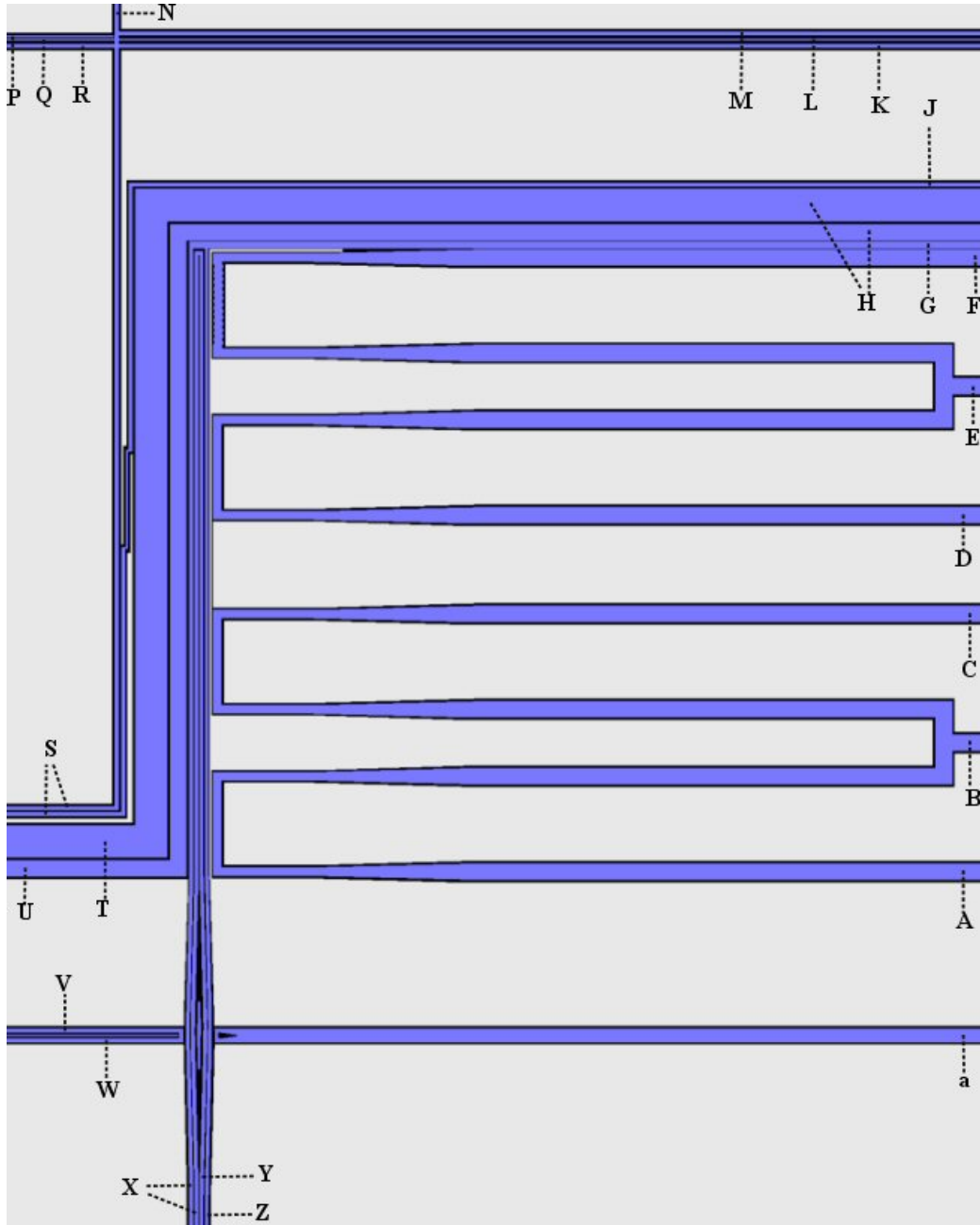


**Figure 2.7:** Central region ( $3.1 \times 3.9 \text{ mm}^2$ ) of the chip design used in this experiment. Outside the field of view the wires broaden towards the 2.2mm wide connection pads. The groves in the gold layer which define the wires are shown in black. The gold wires are shown in blue, while the grey areas are gold parts that are grounded. The letters are used to label the connections and correspond to the labels used in the laboratory.

interferometer can be realized. Another Z-trap can be realized with the  $10\mu\text{m}$  wires shown in the top left corner of the image (K, M, P, R). The Z-potential can be split into a double well potential by the central  $5\mu\text{m}$ -wire (Q - L). The vertical wire (S - N) is intended for loading this trap. The interferometer schemes for these two traps are detailed in [75].

### 2.3.3 Finite size effects

In the discussion of magnetic potentials in this chapter the wires providing the magnetic fields were always assumed to be both infinitely thin and long. Naturally neither is the case for realistic chip wires. Hence actual potentials will differ from idealized calculations to some extent. In general these deviations become significant when the distance of the trap center to the wire is on the order of the wire size. Since this is fulfilled in many of our experiments, better approximations of the trapping potentials are required.

#### Rectangular wires

The wires on our chip are all of rectangular shape. The magnetic field of an infinitely long wire with width  $W$  and height  $H$ , through which a homogeneous current  $I$  flows ( $j = I/WH = \text{const}$ ), can be calculated analytically. Assuming that the wire lies along the  $z$ -axis and extends along the  $x$ -axis from  $-W/2$  to  $W/2$  and along the  $y$ -axis from  $-H/2$  to  $H/2$ , the field components are given by

$$\begin{aligned} B_x(x, y, W, H) = & j \left[ 2y_- \left( \arctan \frac{x_-}{y_-} - \arctan \frac{x_+}{y_-} \right) \right. \\ & + 2y_+ \left( \arctan \frac{x_+}{y_+} - \arctan \frac{x_-}{y_+} \right) \\ & \left. + x_- \ln \left( \frac{x_-^2 + y_-^2}{x_-^2 + y_+^2} \right) + x_+ \ln \left( \frac{x_+^2 + y_+^2}{x_+^2 + y_-^2} \right) \right] \end{aligned} \quad (2.15)$$

$$B_y(x, y, W, H) = -B_x(-y, x, H, W). \quad (2.16)$$

Here the abbreviations  $x_{\pm} = x \pm W/2$  and  $y_{\pm} = y \pm H/2$  have been introduced. For many experimental situations  $H \ll h$  holds, where  $h = y - H/2$  is the distance of the trap center from the wire edge. In that case the wire can be treated as infinitely flat but broad. The field of such a wire is obtained in the limit  $H \rightarrow 0$  in equations 2.15 and 2.16, which leads to the simpler expressions:

$$B_x(x, y, W) = -j \left( \operatorname{arccot} \frac{-y}{y_-} + \operatorname{arccot} \frac{y}{y_+} \right) \quad (2.17)$$

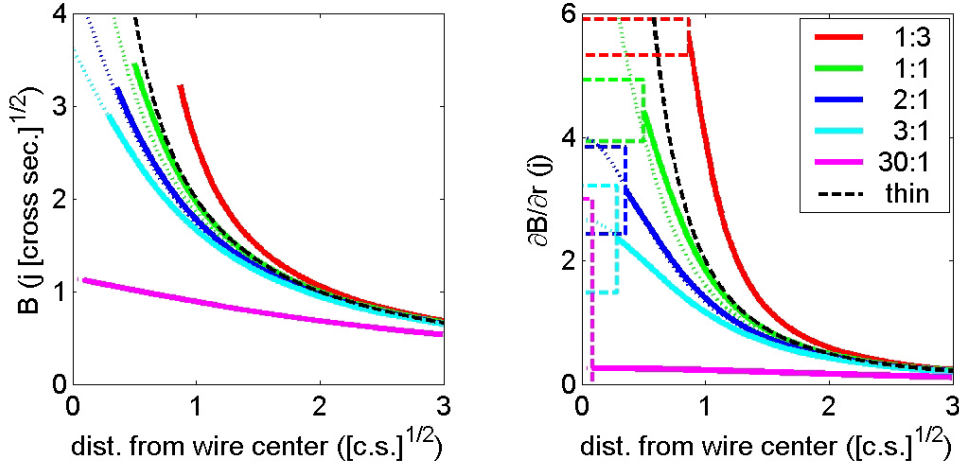


**Figure 2.8:** Behavior of the magnetic field above rectangular wires of different width to height aspect ratios. **Left:** Field strength over the center of the wire ( $x = 0$ ) as a function of the height above the wire. The solid lines represent the field calculated according to equations 2.15 and 2.16 and end at the wire surfaces. The dotted lines show the flat wire approximation (equations 2.17 and 2.18). The black dashed line shows the field of an infinitely thin wire. All wires are normalized to equal cross section, thus the fields are equally normalized to current and current density. **Right:** Corresponding field gradients above the wire center. The wires are shown to scale (dashed lines).

$$B_y(x, y, W) = j \left[ \ln(x_-^2 + y^2) - \ln(x_+^2 + y^2) \right]. \quad (2.18)$$

Here the current density is defined as  $j = I/W$ . In the additional limit  $W \rightarrow 0$  the formulas for the infinitely thin wire are recovered.

In Figure 2.8 the behavior of the magnetic field above the wire center ( $x = 0$ ) is shown for rectangular wires of various width to height ratios. For comparison the flat wire approximations and the infinitely thin wire are also shown. It can be seen that the finite size of the wires only becomes important for distances comparable to the wire dimensions.

How specific chip wire potentials are modeled for calculation depends on the desired accuracy of the results and the experimental parameters. For example for the BEC experiments in the  $100\mu\text{m}$ -trap (Section 4.4) a simple thin wire model suffices to give an accurate description of the potential. On the other hand, for the surface experiments in the same trap more sophisticated models are required, because of the much smaller distance to the wire.

### Non-uniform current density

A further finite size effect arises from the fact that the current flow through wires of arbitrary shape is not homogeneous, even for ideal materials. Figure 2.9 shows examples of numerical calculations of the current density in planar wires. It can

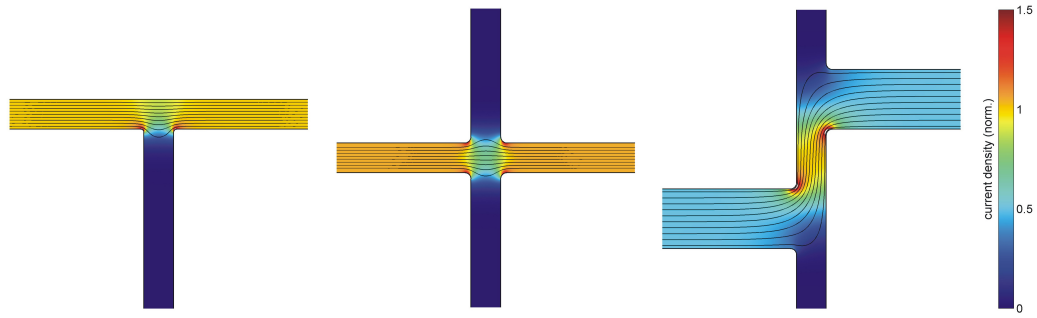


**Figure 2.9:** Numerical calculation of the (planar) current density distribution in different wire geometries. **Left:** The current flow through a straight wire widens at a junction. **Center:** At a wire crossing the behavior is similar. **Right:** The current density in a Z-wire shows a significant deviation from a homogeneous current flow.

be seen that the current density fluctuates at crossings, junctions, and bends in the wires.

In general it would be possible to use such numerically obtained current densities to calculate the resulting magnetic fields, but the required computation power quickly makes this impractical. Instead the current density profiles can be used to improve thin-wire models to more closely resemble the main current flow through the wires.



## 3 The experiment

In this chapter the apparatus used for the atom chip experiments is introduced (Section 3.1). This includes the vacuum setup in which the experiments are carried out and the laser system used to produce the required laser light for the manipulation of  $^{87}\text{Rb}$  atoms.

The second part of this chapter (Section 3.2) covers the different steps of the experiment cycle up to the point when the atoms are loaded to chip-based magnetic traps. Because of the limited trap depths of the chip-wire traps ( $U \leq k_B \times 1\text{mK}$ ), a number of preceding experimental phases are required to prepare atoms sufficiently cold to be confined by these magnetic trapping potentials. The techniques employed in these steps are introduced and their implementation and optimization in our experiment are discussed.

### 3.1 Experimental setup

This section intends to give an overview over the most important hardware components of the experiment. Most of these have been described in detail in previous diploma theses, to which references are given throughout the text.

#### 3.1.1 Experiment control

To simultaneously control all the instruments needed for the experiment an external control system (Adwin-Pro-System) connected to a personal computer with an optical LAN cable is used. The Adwin-Box has its own processor and calculates signal values based on parameters passed to it by the control computer at the start of each experiment cycle. Using an external system greatly reduces the technical noise and facilitates high update frequencies of the output signals.

The system currently has 32 digital output channels, 16 analog (16bit) output channels, and 8 analog input channels. Because of a modular structure both additional channels and extra processor units can be added in the future if necessary.

The system is controlled by a user interface written in MATLAB, which allows the control of all digital and analog output channels with a time resolution of currently  $12.5\mu\text{s}$ . The software supports constant values, linear ramps and splines. The user interface and the Adwin system are described in detail in [16].

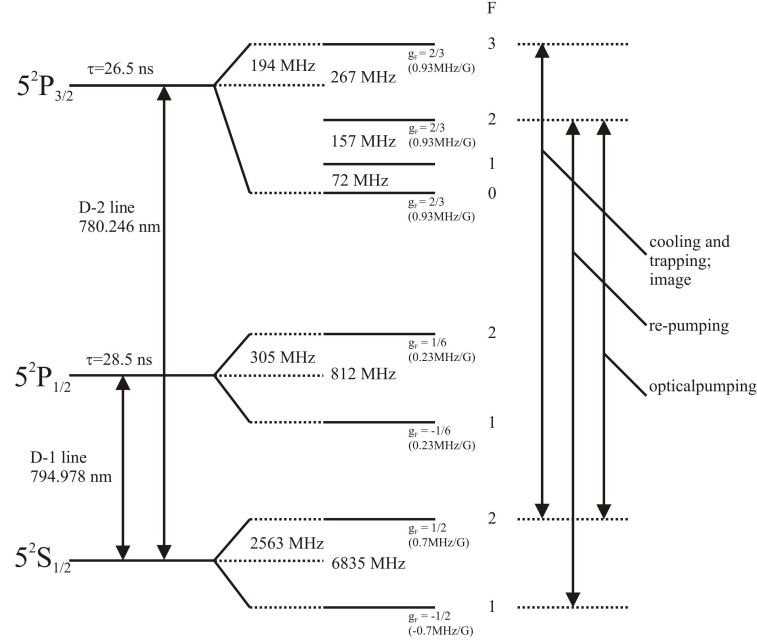


**Figure 3.1:** The hyperfine energy scheme of the  $^{87}\text{Rb}$  D1 and D2 lines. On the right the transitions used in this experiment are shown.

### 3.1.2 Laser system

For the manipulation of atoms with light, frequencies are needed that stimulate transitions between internal states of the atoms. Figure 3.1 shows the D1 and D2 lines of the  $^{87}\text{Rb}$  isotope. As can be seen in the figure we use for the experiment the hyperfine transitions of the D2 line. These transitions have wavelengths around 780nm, which can be produced conveniently by semiconductor diode lasers.

We currently use two separate laser systems, one self-built master/slave diode laser pair with an output power of 20mW and one commercial tapered amplifier system <sup>1</sup> with an output power of 500mW.

To ensure the selective driving of specific hyperfine transitions the frequency of the laser light must be accurate to a precision well below the natural line width. Thus both lasers are stabilized with spectroscopic locking techniques. For the TA 100 frequency-modulation spectroscopy is used to lock the laser on the 1-3 crossover spectroscopy line of the  $|5S_{1/2}, F = 2\rangle \rightarrow |5P_{3/2}\rangle$  transition [44]. The self-built laser is locked on the  $|5S_{1/2}, F = 1\rangle \rightarrow |5P_{3/2}, F = 2\rangle$  transition with saturation spectroscopy [57].

A total of four different frequencies are necessary for this experiment: *cooling* and *repumping* frequencies for the magneto-optical trap, plus frequencies for *imaging*

<sup>1</sup>Toptica, TA100 system

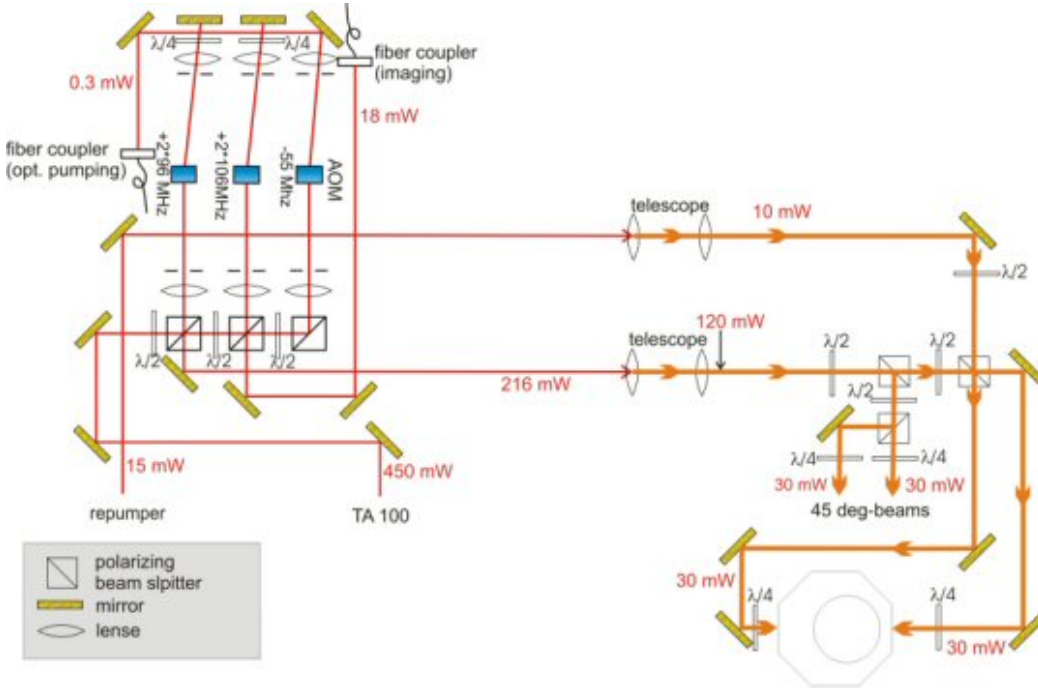


**Figure 3.2:** Overview of the optics system used in our experiment. Three of the required frequencies are produced by AOM setups in a separate preparation area before being guided to the experiment area. The optical pumping and imaging beams are transmitted through optical fibers, the cooling and repumping beams are guided to the vacuum chamber via mirrors. Typical beam intensities are shown for different stages of the beam preparation.

and *optical pumping*. The output beam of the TA 100 is split into three parts which are frequency-shifted by acousto-optical modulators (AOMs) to the desired frequencies to produce the cooling, imaging, and optical pumping beams.

The cooling and the imaging beam pass twice through the respective AOMs, to provide total frequency shifts of  $+2 \times 96\text{MHz}$  (cooling) and  $+2 \times 106\text{MHz}$  (imaging). This *double-pass* setup allows a change of the frequency shift without changing the direction of the outgoing beam, so that the detuning can be changed during the experiment, usable for example for off-resonance imaging (Section 3.2.6).

For the optical pumping beam a single pass setup is used with a frequency shift of  $-55\text{MHz}$ , because only one fixed frequency is required here.

Using AOMs to generate the required frequencies offers a number of advantages. The number of lasers that need independent spectroscopy setups is reduced, the AOM frequency shift is tunable over a range of  $\sim 100\text{MHz}$ <sup>2</sup>, and the AOMs act as light shutters with cut-off times in the nano-second range.

For the repumper beam using an extra laser is more convenient, because the re-

<sup>2</sup>Larger shifts up to 1GHz are possible with special AOMs, but only at the cost of large intensity loss.

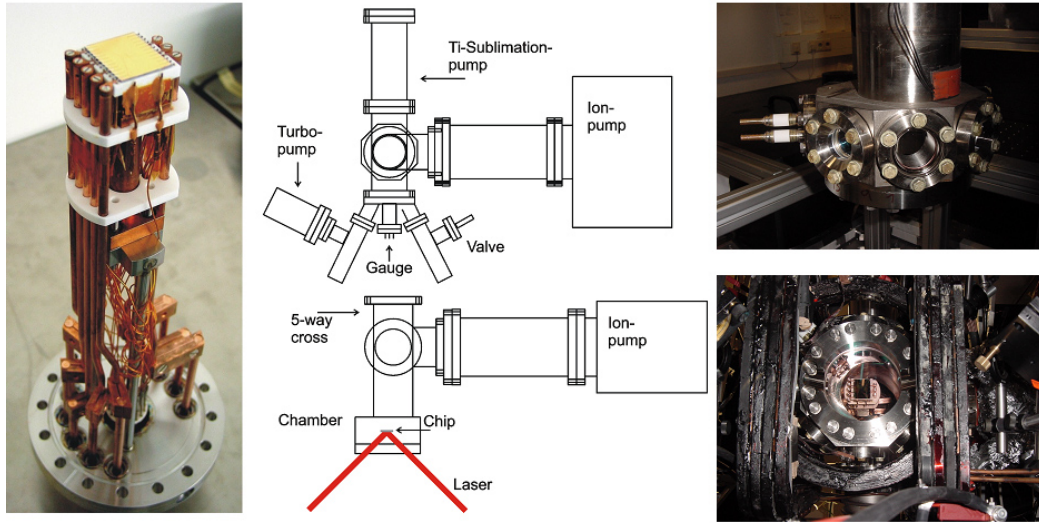


**Figure 3.3:** **Left:** Chip mount: The atom chip on top of the structure is connected to high-current vacuum feedthrough. The whole assembly is hanging upside down in the vacuum chamber. **Center:** Top and side view of the vacuum chamber design. The actual experiment area is the small chamber at the bottom of the setup. **Right:** Photograph of the vacuum chamber before (top) and after (bottom) the assembly of the external coils and optics.

quired frequency shift from the TA 100 transition to the repumping frequency is too large to be done efficiently with AOMs or EOMs (electro-optical modulators).

The disadvantage of using AOMs is the loss of light intensity. Approximately 30% of the incoming intensity are lost with each pass for the frequency shifts we apply. The output power of the used laser must be sufficient to account for this loss.

After the splitting and frequency shifting the different beams are guided to the physics chamber. The optical pumping and the imaging beam are passed through polarisation-preserving fibers to improve their beam-shape to a gaussian profile, while the cooling and the repumper beam are sent through telescopes to widen their beams to diameters of approximately 2cm before they reach the experiment area. A schematic drawing of the optics setup is shown in Figure 3.2.

### 3.1.3 Vacuum chamber

Experiments with ultracold atoms have to be performed in ultrahigh vacuum (UHV) to avoid perturbation of the trapped atoms by background gas. For this experiment a single chamber setup was chosen, meaning that all experiment steps take place at the same location. This sets stringent requirements on the vacuum pumps, between the MOT-phase and the magnetic trapping phase the vacuum has to be improved significantly within a few seconds. To achieve this an ion

pump is used, which restores pressures in the range of  $10^{-11}$  mbar with the required speed. Additionally, once per week a titanium filament inside the chamber is used to emit a two minute pulse of titanium which condenses on the chamber walls and then absorbs impurities in the chamber. This pump combination achieves a vacuum pressure below  $7 \times 10^{-12}$ , the lowest value we can measure with our vacuum gauge.

The *physics chamber*, where the actual experiments take place, sits at the bottom of the vacuum chamber (Figure 3.3). The atom chip is build onto a mounting hanging upside down into this area [9]. Feedthroughs for connecting the chip wires are positioned on the top side of the chamber. The physics chamber has an octagonal shape with openings on each side. On seven sides windows allow optical access to the experiment area. The four of these windows which coincidence with the axes of the magnetic coils (Section 3.1.4) have special anti-reflection coatings to ensure loss free passing of the laser beams. The eighth side of the chamber is used for feedthroughs to connect the rubidium dispensers. We use three dispensers connected in parallel which can be heated by running a current through them. At the bottom of the chamber there is a further window, so that the experiment area can also be accessed from a vertical direction. A detailed description of the chamber design and the vacuum creation process can be found in [57].

### 3.1.4 Current carrying structures

In addition to the wires on the atom chip inside the vacuum chamber, other current-carrying structures are used to create magnetic fields for trapping of the atoms. Pairs of parallel coils outside the vacuum chamber create homogeneous fields in the experiment area, while a set of copper wire structures placed underneath the atom chip generate inhomogeneous fields for the initial trapping phases of the experiment.

#### Magnetic coils

Three pairs of coils are positioned around the vacuum chamber in Helmholtz configuration. The field parallel to the chip surface and perpendicular to the central bars of the Z-structures on the chip is called the *bias* field. The *backward-forward* (b-f) field is also directed parallel to the chip, but perpendicular to the bias field. The *up-down* (u-d) field points perpendicular to the chip surface and the two other fields. The coils are constructed such that they can create fields in the center of the chamber of up to 120G for the bias and the up-down coils and 80G for the backward-forward coils [16].

Because the power supplies used for these coils are unipolar, the direction of each field can only be inverted by switching the connectors. Since this is impractical during the experiment, smaller extra coils were added to each coil. These coils

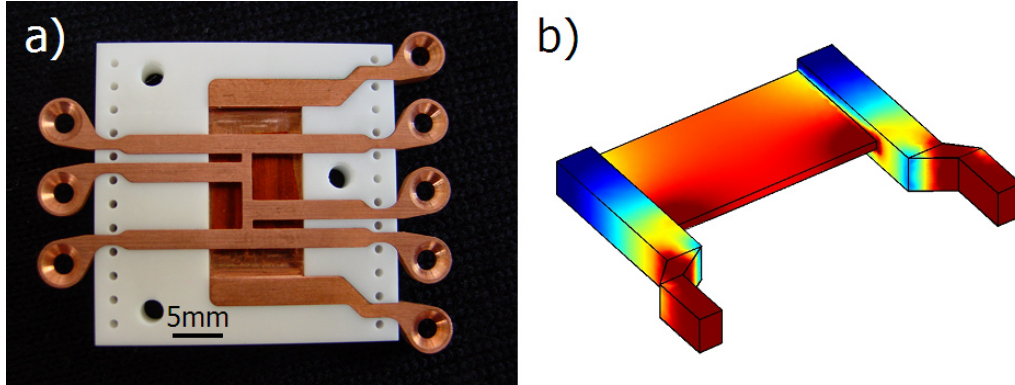


**Figure 3.4:** **Left:** Photograph of the copper structures fitted into the chip holder. The broad U-structure can be seen underneath the smaller H-structure. The atom chip is directly mounted on top of this. **Right:** Visualization of numerical calculations for the current density in the U-structure. Dark red (blue) corresponds to high (low) current density. The thick outer bars lead to a more homogeneous flow of the current through the central plate [9].

can create constant fields of up to 10G in the opposite directions of the original coils.

Electronic switches are used to achieve turn off times for the currents through the coils below  $100\mu\text{s}$ . These are specifically designed to take into account the inductivity of the large coils which requires special means of fast energy dissipation (details can be found in [114]).

Another set of three coil pairs around the whole apparatus is used to create compensation fields that cancel outside fields, like the earth magnetic field and laboratory stray fields. This is necessary to avoid outside effects during the experiment phases without magnetic fields, e.g. the optical molasses (3.2.2). These coil pairs can create fields of up to 3G each and are running continuously during the experiment.

### Copper structures

A set of copper wires is built into the chip mounting underneath the atom-chip, as shown in Figure 3.4. A U-shaped structure build from a single copper piece is integrated into the MACOR block holding the atom chip. The quadratic outer leads ( $3 \times 3\text{mm}^2$  cross-section) are thicker than the central plate ( $0.7 \times 10 \times 18\text{mm}^3$ ) to make the current flow through the central plate more homogeneous. This structure is used together with the bias coils to create the magnetic field for the magneto-optical trap (Section 3.2.1).

A second H-shaped structure of 1mm thickness with six connections is placed on top of the U-structure, from which it is isolated by a thin Kapton foil. Depending on which connectors are used either a Z- or U-shaped wire can be realized. The Z-wire can have a central bar of either 4mm or 10mm (8mm can also be realized with

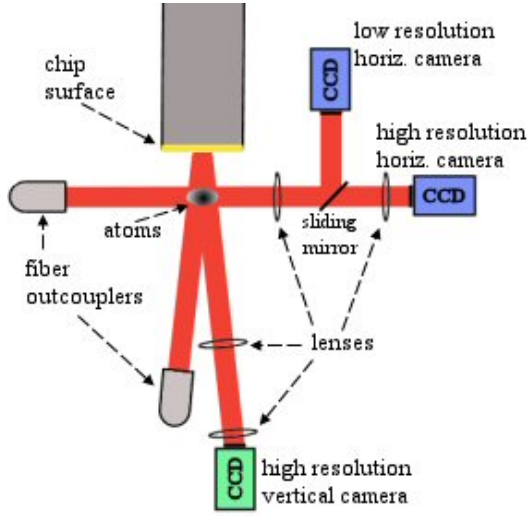


**Figure 3.5:** Schematic of the imaging system. Two independent systems allow the imaging of the atom cloud from two different angles. Both systems consists of a fiber outcoupler providing the imaging beam, a lens system for magnification and a CCD camera. For the horizontal imaging two CCD cameras with different magnification can be used.

an off-center configuration). The 4mm-Z is used to generate the inhomogeneous field for the initial magnetic trap in the experiment procedure (Section 3.2.4. Both structures are designed to carry currents of up to 100A, although currently the currents are limited to 60A by the power supplies used. Details on the design of the copper structures and the chip mounting can be found in [9] and [126].

### 3.1.5 Imaging system

To gain information about the trapped atoms the experiment area is imaged with CCD cameras. Two independent systems allow imaging from two angles. The line of sight of the *horizontal* imaging system is parallel to the chip surface, while the *vertical* system points onto the chip surface from below the vacuum chamber, as is shown in Figure 3.5.

For the horizontal imaging a fast frame-transfer 16-bit CCD-camera<sup>3</sup> is used that can take two images of  $1024 \times 1024$  pixels within 10ms. This camera has a quantum efficiency of 70% at 780nm, the pixel size is  $13 \times 13 \mu\text{m}^2$ . In front of the camera two lenses function as an objective to focus and magnify the image. The lenses currently used have focal lengths of 145mm and 250mm respectively, resulting in a magnification factor of 1.7 (currently being changed to 3.5). The lenses are mounted on a motorized translation stage with a positioning accuracy of  $2.5 \mu\text{m}$  to guarantee optimal focussing on the atom cloud. On the other side of the vacuum chamber a fiber outcoupler is positioned to send the imaging light beam required for absorption imaging through the chamber into the camera.

The horizontal imaging can be switched to an additional low-resolution 8-bit CCD camera<sup>4</sup> by a sliding mirror that can be moved between the two lenses. The first lens combined with a 50mm camera objective focussed on infinity results in a

<sup>3</sup>Roper Scientific MicroMAX 1024BFT

<sup>4</sup>Pulnix TM6AS



demagnification factor of 3. We use this camera for overview images during the early stages of the experiment when the atom cloud is too large to be imaged with the high-resolution camera.

For the vertical imaging a  $1340 \times 400$  pixel 16-bit CCD camera <sup>5</sup> is used. A pixel size of  $20 \times 20 \mu\text{m}^2$  combined with a magnification factor of 5 provided by two lenses (140mm and 700mm focal length) in front of the camera give a resolution of  $4 \mu\text{m}$ . The vertical imaging beam is pointed at the chip surface from which it is reflected into the camera (a small angle of  $\sim 5^\circ$  is necessary for the reflected beam to pass the fiber outcoupler (Figure 3.5)). Due to the non-reflecting grooves on the chip the wire structure is imprinted onto the imaging beam, reducing the quality of the images. Hence we use the vertical imaging mainly to survey the position of the atom cloud in relation to the chip structures during chip trap experiments instead of for quantitative analysis.

## 3.2 Experimental procedure

A single run of our experiment currently lasts 40 seconds. Under normal operation these runs are automatically repeated continuously. Each experimental cycle consists of a number of different steps, which are listed in table (3.1).

The experiment starts with a magneto-optical trap (MOT) to capture and cool atoms down to  $\sim 100 \mu\text{K}$ . The atoms are then further cooled by an optical molasses and transferred to the desired spin-state for purely magnetic trapping by optical pumping. After that follows a phase of radio frequency-induced evaporative cooling in a magnetic trap created by the Cu-Z structure underneath the atom chip until temperatures below  $10 \mu\text{K}$  are reached. At this point the atoms are transferred to magnetic traps created by the atom-chip wires and the actual experiments are carried out. Each cycle ends with the imaging of the trapped

<sup>5</sup>Roper Scientific NTE/CCD-1340/400

Step	Duration	Temperature	Number of atoms
MOT	22s	$200 \mu\text{K}$	$3 \times 10^8$
Optical molasses	10ms	$\leq 50 \mu\text{K}$	$3 \times 10^8$
Optical pumping	$300 \mu\text{s}$	$\leq 50 \mu\text{K}$	$3 \times 10^8$
Copper-Z trap	10s	$1 - 10 \mu\text{K}$	$10^5 - 10^6$
Transfer to chip trap	100ms – 1s	$\leq 10 \mu\text{K}$	$10^5 - 10^6$
Chip trap	up to 8s	$100 \text{nK} - 10 \mu\text{K}$	$10^3 - 10^6$
Imaging	up to 30ms		

**Table 3.1:** Operational sequence of a typical experiment run. Also listed are typical final temperatures and numbers of atoms for each step.



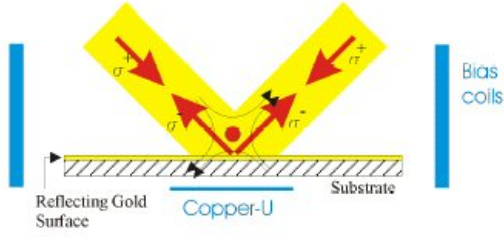


**Figure 3.6:** Beam configuration for the Mirror-MOT setup. It can be seen that the reflected beams have the right polarization to form beam pairs of opposite helicity with the incoming beams. The pair of horizontal beams travels perpendicular to the image plane. Also shown are the bias coils creating the horizontal homogeneous magnetic field.

atoms. The actual experiments in the magnetic traps will be discussed in detail in the next chapters.

### 3.2.1 Magneto-optical trap

A magneto-optical trap (MOT) is the standard starting point for experiments with ultracold atoms. It provides a highly efficient and robust trapping mechanism that can capture and cool room temperature atoms to  $\mu K$  temperatures. Detailed explanations can be found in standard textbooks, for example [93, 103]. The velocity dependence of the radiation pressure of a laser beam is used to slow and thus cool atoms. A beam red-detuned from a resonance frequency results in a net momentum transfer to the atom in the direction of the beam, causing a friction like force on the atom. Combining such beams from all six directions causes an overall slowing of the atom.

The spatial trapping of the atoms is achieved by adding a magnetic quadrupole field. Due to the Zeeman-effect the absorption rate of the atom becomes sensitive to the polarization of the laser beams. When the helicity of the beams is matched correctly to the magnetic field the radiation force acting on the atom always points toward the trap center, confining the atoms.

#### The U-MOT

We use a modification of the standard MOT setup found in the literature that is adapted to the specific configuration of our experiment [126]. Since the atom-chip blocks the optical access to the trapping area from one direction the standard arrangement of six laser beams can not be used. Instead only four beams are used, two counter-propagating ones parallel to the chip and two hitting the chip under 45 degrees, as shown in Figure (3.6), with the chip-surface acting as a mirror for these beams. Because the helicity of the beams is inverted by the reflection the incoming and reflected beams form two perpendicular pairs of beams with correct polarization in the region where all beams overlap. Together with the horizontal beam pair the standard six-beam configuration is restored in this area. This *Mirror-MOT* setup is used in many atom-chip experiment [110, 39].

Because the helicity of the two 45° beams must be opposite in this configuration,

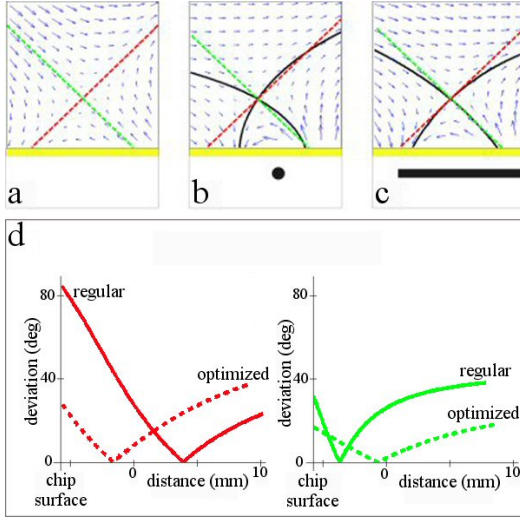


**Figure 3.7: Top:** Vector plots of different field configurations. (a) ideal quadrupole field, (b) thin U-wire with horizontal bias field, (c) optimized U-wire with tilted bias field. The red and green lines indicate the axes of the ideal quadrupole field, while the black lines show the approximated field axes of the U-wire configuration. The cross-section of the U-wires is drawn to scale under (b) and (c). **Bottom:** Angular deviation from the ideal quadrupole axes as a function of distance from the chip surface along the directions of the two  $45^\circ$  beams (green and red lines in (a)-(c)). The parameters for these plots are  $I = 55\text{A}$ ,  $B_{\parallel} = 14.5\text{G}$  ( $12.8\text{G}$ ) in the plane parallel to the wire and  $B_{\perp} = 0\text{G}$  ( $3.0\text{G}$ ) perpendicular to the wire for the regular (optimized) U.

the orientation of the magnetic quadrupole field must be oriented such that the field axis coincides with one of the  $45^\circ$  beams. When external coils are used to provide the field this means that these usually bulky coils have to be placed at an  $45^\circ$  angle outside the vacuum chamber, which greatly hinders the optical access to the experiment region. Also because of the distance to the trap center, large currents ( $\geq 100\text{A}$ ) in the coils are needed, which usually means that some way of cooling the coils is necessary. Instead of such quadrupole coils we use the U-shaped copper-structure underneath the chip (Section 3.1.4) to create a magnetic field that in combination with a horizontal homogeneous field approximates a quadrupole field, as has been shown in Section 2.2.2. The agreement with an ideal quadrupole field can be further improved by two changes to the U-trap. Broadening of the central bar of the U-structure and adding a component perpendicular to the chip surface to the bias field both enlarge the area where the resulting field well approximates the ideal quadrupole field, the effects of these improvements are shown in Figure 3.7. To verify these improvements experimentally we compared a ‘thin’ U-MOT created with the smaller Cu-H structure. Switching from the thin to the broad U increases the number of trapped atoms by a factor of 10, tilting the bias fields further enhances this number by a factor of 2 to 3. Figure 3.8 shows the measured number of trapped atoms as a function of the angle between the bias field and the U-structure. This number becomes maximal for a bias field tilt of  $13^\circ$ , for which the resulting field most closely resembles an ideal quadrupole field.

### The repumper

For the MOT to work the transition used for cooling the atoms must form a closed two-level system. In our case the  $|5S_{\frac{1}{2}}, F = 2\rangle \rightarrow |5P_{\frac{3}{2}}, F = 3\rangle$  transition is used.

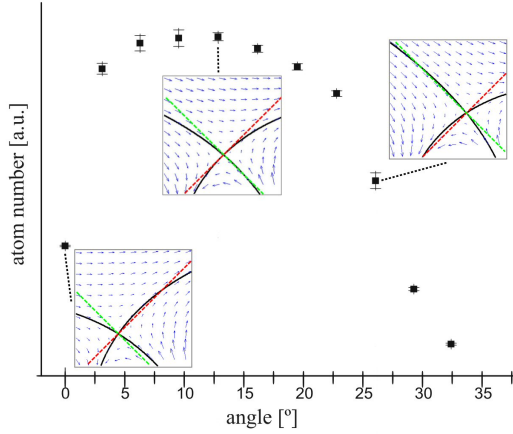


**Figure 3.8:** Number of atoms for various tilts of the bias field in the U-MOT. The inserts show the vector plots of the resulting fields for three different angles ( $0^\circ$ ,  $13^\circ$ ,  $26^\circ$ ). The calculated optimal tilt of  $13^\circ$  is well reproduced in the measurement.

Because the  $|5P_{3/2}, F = 2\rangle$  lies only 267 MHz lower than the  $F = 3$  level there is a finite probability that atoms are excited to this level from which they can decay to both the  $|5S_{1/2}, F = 1\rangle$  and  $|5S_{1/2}, F = 2\rangle$  level. Atoms in the  $F = 1$  state are not excited by the cooling light and therefore are lost from the cooling cycle. To prevent this the repumper laser is added to the MOT by overlapping its two beams with the  $45^\circ$  cooling beams. It is running on the  $|5S_{1/2}, F = 1\rangle \rightarrow |5P_{3/2}, F = 2\rangle$  transition and permanently pumps the atoms decaying into the wrong ground state back into the excited state. This effectively creates the required closed two-level system.

### MOT-loading

The U-MOT is loaded directly from the background pressure in the vacuum chamber. The Rb atoms are emitted into the chamber by three dispensers which can be heated by running a current through them. By changing this current the amount of Rb in the chamber during the MOT-loading can be changed. Higher background pressure means faster loading and greater total size of the MOT, but also a degradation of the vacuum. This in turn reduces the lifetime of the magnetic traps later in the experiment, because collisions between trapped atoms and the hot background gas become more likely.

Therefore a balance has to be found between fast MOT-loading and long magnetic trap lifetime. Another factor limiting the loading speed is the Rb dissipation rate into the chamber. The used dispensers were tested to withstand a continuous current of 25A (i.e. a current of 8.3A through each single dispenser), to avoid the risk of a burn through the dispenser temperature should not exceed the value reached in this case. We were able to make a relative heat measurement by collecting the emitted light of the glowing dispensers with a photo diode. This allowed us to optimize the dispenser current to speed up the loading phase. Using a larger current (30 – 32.5A) during the beginning of the loading phase heats the dispensers to the maximal temperature in a much shorter time. After

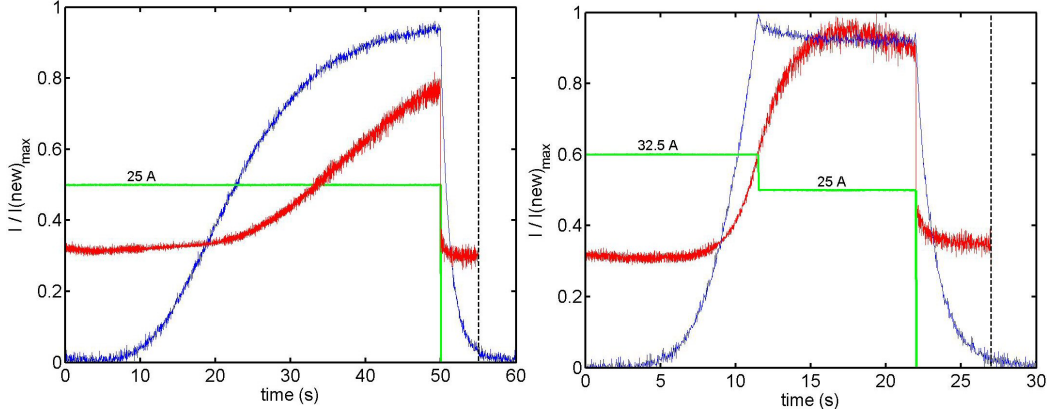


**Figure 3.9:** Comparison of the original (left) and the optimized (right) MOT-loading. Shown in blue is the light emitted by the glowing dispenser, which is an indicator of the dispenser temperature. The red curves show the fluorescence light from the atoms, which is proportional to the number of trapped atoms. The curves are normalized to the maximal values of the new loading scheme. Shown in green are the dispenser currents. The vertical black line indicates the beginning of the magnetic trapping phase. It can be seen that the dispenser are switched off 5s earlier to guarantee sufficient cooling until the start of the magnetic trap. The fluorescence signal from the atoms also drops at the same time as the dispensers are switched off which is caused by the lowering of the intensity of the MOT beams for the last 5s of the MOT-phase. By adjusting the dispenser current the MOT-loading time could be more than halved.

this temperature is reached the current is reduced to 25A to maintain a constant temperature until the dispensers are switched off. Figure 3.9 shows temperature measurements for the original and an improved loading phase. To measure the resulting numbers of atoms in the trap fluorescence light from the atoms is collected with a photo diode, again giving relative numbers. It can be seen that the total amount of atoms also increased somewhat. More importantly though, the duration of the loading phase could be reduced from over 50s to 22 – 25s. Typical observed loading rates are  $3 \times 10^7$ /s once the dispensers are heated.

During the last five seconds of the MOT loading the dispenser are turned off while the MOT continues to load from the background pressure. This is done to ensure optimal vacuum conditions for the magnetic trapping phase, which greatly prolong the lifetime of those traps (Section 3.2.4 for measurements). The dispensers are water cooled to decrease the time required for cooling.

The intensity of the MOT beams is reduced during the final five seconds to avoid atom loss due to light induced collisions which start to play a role for the atom densities achieved at the end of the MOT phase.

In the final 100ms of the loading-phase the MOT bias field is ramped up to compress the atom cloud and move it closer to the chip surface. The other two homogeneous fields can be used to displace the trap in the plane perpendicular to the chip surface, if necessary. To facilitate an effective transfer the MOT should sit directly above the center of the magnetic trap (Section 3.2.4 for more details

on this transfer).

Under normal experiment conditions there are typically  $\sim 2 \times 10^8$  in the compressed MOT, this number can be increased to  $3 \times 10^8$  when no considerations about the vacuum quality are made.

### 3.2.2 Optical molasses

After the MOT-phase all magnetic trapping fields are switched off for a duration of 10ms, while the cooling light is detuned to about 70MHz below resonance. This stronger detuning results in further cooling of the atoms. Although the atoms are no longer spatially trapped, the diffusion of the atoms is small because of the already low temperature. Even small outside magnetic field would disturb the atoms and cause an acceleration of the cloud along the field direction. Hence the compensation coils must be set to compensate such fields.

After this extra cooling step the temperature of the atom cloud is  $\sim 40\mu\text{K}$  and densities of  $10^{10}\text{cm}^{-3}$  are achieved.

### 3.2.3 Optical pumping

In the optical molasses the atoms are distributed equally over the five magnetic sublevels of the  $F = 2$  ground-state. Only the  $m_F = 1$  and  $m_F = 2$  states are low-field seekers (Section 2.1.1), with the  $m_F = 2$  state seeing a magnetic potential twice as deep as the  $m_F = 1$  state ( $U \propto m_F$ ). Hence the  $m_F = 2$  is the ideal state for magnetic trapping. To transfer the atoms to this state a small bias field is turned on to provide the quantization axis and a  $300\mu\text{s}$  optical pumping pulse of  $\sigma^+$ -polarized light resonant to the  $|5S_{\frac{1}{2}}, F = 2\rangle \rightarrow |5P_{\frac{3}{2}}, F = 2\rangle$  transition is sent through the chamber along this axis. Because of the circular polarization we have  $\Delta m = +1$  for the excitation, while for the spontaneous decay back to the ground state all possible transitions are equally probable ( $\Delta m = -1, 0, +1$ ). Over time this results in an accumulation of the atoms in the  $m_F = 2$  state, which is a ‘dark’-state for  $\sigma^+$ -light. To prevent the loss of atoms decaying into the  $|5S_{\frac{1}{2}}, F = 2\rangle$  state the repumper must be left on during this phase.

In the course of the experiment it turned out that very small intensities of  $< 20\mu\text{W}$  are sufficient to achieve complete polarization of the atom cloud. Higher intensities actually can have the negative effect of displacing the atom cloud, reducing the loading efficiency into the magnetic trap.

### 3.2.4 Magnetic Cu-Z trap

At this stage the atoms can be trapped by a purely magnetic trap. Instead of transferring the atoms directly to a chip-based trap, as is done in other chip-experiments [100, 55], we use an intermediate step. The initial magnetic trap for all our experiments is generated by the Cu-Z structure underneath the chip.

Together with homogeneous fields it creates a Ioffe-Pritchard type Z-trap as described in Section 2.2.3. Due to its larger size and the much larger possible currents, both the effective capture area and the trap depth of the Cu Z-trap are larger than what can be achieved with the chip traps. This allows a nearly complete transfer of the optical molasses to the magnetic trap. Only after a further cooling stage the atoms are transferred to the chip traps.

The calculation of the trapping potential and the actual BEC experiments in this trap will be the topic of Section 4.2. Here the trap loading and experiments to characterize the trap are described. Also the utilized cooling mechanism, *radio frequency induced evaporative cooling*, is explained.

### Trap loading

To guarantee an efficient transfer from the optical molasses to the magnetic trap, two factors have to be considered. Firstly, the center of the trap should overlap with the molasses center as precisely as possible. Secondly the initial steepness of the magnetic trap should match the temperature and extension of the atom cloud, i.e.

$$\omega_i = \sqrt{\frac{k_B T}{m r_i^2}} \quad (3.1)$$

where  $r_i$  is the extension of the molasses in the  $i$ th dimension. If the trap is too steep, the atoms will be heated during the transfer. If it is too shallow, the atoms can expand non-adiabatically which results in reduced phase-space density. This synchronizing of the magnetic trap and the optical molasses is known as *mode-matching*.

In our case the Cu-Z trap can not be made to exactly match the molasses shape, which is determined by the U-MOT potential, so that Equation 3.1 can not be exactly fulfilled for all three dimensions. The standard approach we choose is to use a trap with too steep transverse confinement ( $\omega_x$  and  $\omega_z$  larger than suggested by Equation 3.1), because only then a sufficient longitudinal confinement is guaranteed. For this trap we use a current of 60A in the Cu-Z, a bias field of 38G, and a Ioffe field of 27G. With this trap we achieve the highest trapping efficiency, with more than  $10^8$  initially trapped atoms. The steeper confinement both compresses and heats the atoms, typical temperatures are  $\sim 350\mu\text{K}$  after 50ms magnetic trapping. Because of the higher density in the magnetic trap the phase space density (see Equation 4.1 for the definition of this quantity) stays roughly constant ( $\phi = n\lambda_{dB}^3 \approx 10^{-7}$ ). This means that the transfer to the magnetic trap is (almost) adiabatic (for good mode matching).

The second aspect of the mode-matching is the overlapping of the optical molasses with the center of the magnetic trap. Since the parameters for the magnetic trap are determined by the aforementioned matching of the trap shapes, the po-

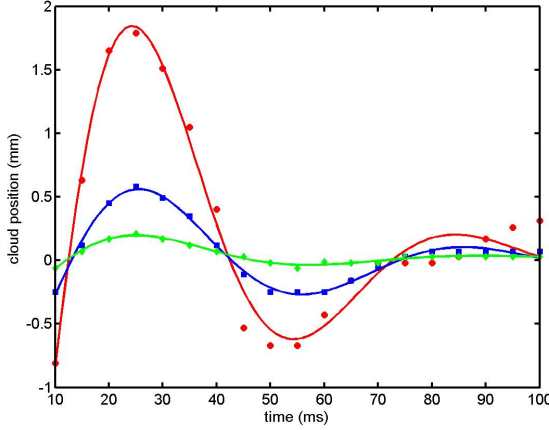


**Figure 3.10:** Measurement of the longitudinal trap frequency of the Cu-Z trap. By displacing the atom cloud along the longitudinal direction of the trap before loading, harmonic oscillations can be excited. Data sets for three different displacements are shown, the solid lines are fitted damped oscillations. The measured frequency is  $(31 \pm 1)$  Hz.

sition of the magnetic trap center is fixed. The position of the optical molasses, on the other hand, can be changed by adjusting the magnetic fields during the final compression stage of the MOT, as has been explained in Section 3.2.1. By changing the final bias field the distance of the cloud to the chip can be adjusted (this also changes the compression of the cloud). The b-f and the u-d field shift the trap center in the plane parallel to the chip. To check the final position of the molasses we image the atom cloud before the transfer to the magnetic trap, from these images we can directly see the position along the vertical and one horizontal axis. Changes in the position along the imaging direction can not be seen. The optimal molasses position along this axis is found by looking at the number of atoms in the magnetic trap after 50ms. The best position is assumed to be found when this number is maximal.

A molasses displaced in respect to the magnetic trap will lead to center-of-mass oscillations of the atoms in the magnetic trap, which causes heating of the atoms. Although in general an impedimental effect, this can be used to measure the longitudinal trap frequency. Figure 3.10 shows the position of the trapped atom cloud as a function of time for various degrees of initial displacement. The damped oscillation of the cloud can clearly be seen, the observed frequency is  $\nu = \omega/2\pi = 31 \pm 1$  Hz.

### Trap lifetime

To carry out experiments in the magnetic trap it must be ensured that the lifetime of the trap exceeds the duration of the experiments. The main limiting factor on the lifetime is the background vapor pressure in the chamber. Atoms will be expelled from the trap by collisions with hot atoms. In dense atomic ensemble other processes start to play a role, like inelastic three-body collisions [95], but this does not play a role for thermal atoms in the Cu-Z trap.

To measure the trap lifetime the number of trapped atoms is observed as a func-



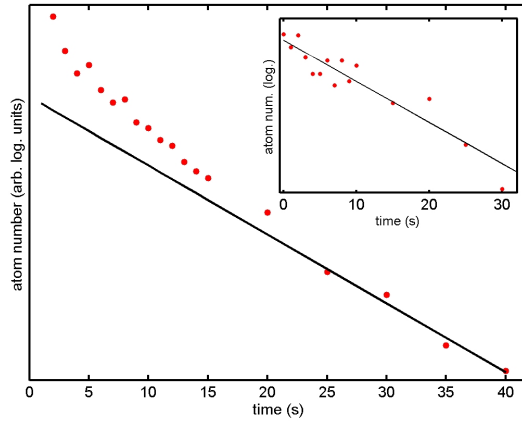


**Figure 3.11:** Lifetime measurement in the Cu-Z trap without additional cooling. During the first 20s an over-exponential loss dominates. This is due to evaporation effects as indicated by the coinciding drop of temperature ( $350\mu K \dots 150\mu K$ ). After equilibrium has been reached only the exponential loss due to the background gas plays a role. The inset shows a measurement performed with cooled atoms ( $T = 25\mu K$ ). Here a purely exponential decay can be seen. The fit yields a lifetime of  $\tau = 45s$ .

tion of time, as shown in Figure 3.11. During the first  $\sim 20s$  we observe an over-exponential decay. This is caused by the fact that the initial trap is completely filled with atoms, but the trapped ensemble is not in thermal equilibrium. Through collisions between the trapped particles the ensemble energy is redistributed until an equilibrium distribution is achieved, but in this process a fraction of the atoms receives enough energy to leave the trap (*evaporation*). During this process the temperature of the atoms falls from  $350\mu K$  to  $150\mu K$ . Once the thermal equilibrium is reached the temperature becomes constant and a normal exponential decay is observed. To more precisely measure the time constant of this decay the measurement can be done with cooled atoms. We then measure trap lifetimes of  $\tau > 45s$  which is much larger than typical experiment times.

To avoid the loss of atoms from the initial trap, the trap volume (the region of space where atoms are captured into the trap) would have to be increased. This could be done to some extent by increasing the current in the Cu-Z, but the main limiting factor is the broadness of the central wire part. The already planned next-generation mounting will contain a wider Z-structure which will provide an increased trap volume. Since this will lower the efficiency of the evaporative cooling process (see next paragraph), a second smaller Z-structure will provide the final trap better suited for cooling. This two-stage process will provide an increased number of atoms to be loaded into the chip traps.

### Radio frequency-induced evaporative cooling

Once the atoms are trapped magnetically, they must be cooled from initial temperatures around  $300\mu K$  to  $\sim 1\mu K$ . The standard technique for cooling in magnetic traps is known as *forced evaporative cooling* [63]. The basic principle is the same as for the aforementioned natural evaporation process after loading the trap. Here, the hottest atoms are intentionally removed from the trap, resulting in a reduction of the average energy, i.e. the temperature, of the remaining



atoms.

The ejection of atoms from the trap is done by inducing transitions between the spin states of the atoms from a low-field seeking to a high-field seeking state. For transitions with  $\Delta F = 0$  the corresponding frequencies lie in the MHz (radio frequency) range. More specifically for the  $|5S_{1/2}, F = 2\rangle$  hyperfine state of  $^{87}\text{Rb}$  the transition frequency between the magnetic levels is given by

$$\nu = \frac{\mu_B \Delta m_F g_F B}{h} \approx 0.7 \text{MHz} \times \Delta m_F B [\text{G}]. \quad (3.2)$$

Because of the inhomogeneity of the trapping field the required frequency to induce a spin flip depends on the position of the affected atom in the trap. Irradiation of the trapping area with a constant radio frequency (rf) will thus create a 'hole' in the trap at locations of corresponding field strength. Only atoms with sufficient kinetic energy to reach the hole are ejected from the trap. After rethermalization of the atoms the radio frequency can be reduced to lower the ejection energy and again remove the hottest fraction of atoms.

A mathematical model of this cooling process can for example be found in [103, 86, 26]. It turns out that the efficiency of the evaporative cooling depends greatly on the shape of the trapping potential. This is due to the fact that for cold atoms the collision rate is determined mainly by the atomic density. Thus evaporative cooling works best in strongly confining traps, making linear potentials more suited for cooling than harmonic potentials.

In practise the radio frequency is lowered continuously during the cooling process. In conventional experiments usually an antenna outside the vacuum chamber is used. Having current carrying structures inside the chamber allows us to use a source much closer to the atoms, greatly reducing the required emission power and resultant noise picked up by electronic equipment in the laboratory. Currently we use the same Z-wire used for the magnetic trap as antenna by adding a small sinusoidal modulation onto the dc-current flowing through the wire. The utilized function generator <sup>6</sup> is externally controlled by the experiment control system, allowing complex sweeps consisting of multiple ramps.

The cooling phase in the Cu-Z trap usually lasts 10s. A too fast evaporation process becomes inefficient because the atoms can not sufficiently rethermalize, while for a too long cooling phase trap losses due to limited lifetime start to play a role. We tested cooling phases of 5–25s, 10s turned out to be the most efficient duration for the production of cold thermal atoms ( $T \leq 15\mu\text{K}$ ) for loading into the chip traps. Cooling times as short as 5s can be used, when the atoms are transferred to the chip traps at a higher temperature ( $T = 20 - 30\mu\text{K}$ ).

We start the rf-sweep at 20MHz, which are ramped down to 5MHz in 5s, followed by a second 5s ramp from 5MHz to 0.1–3MHz depending on the trap parameters and the desired end temperature.

---

<sup>6</sup>Agilent 33220A 20MHz Function/Arbitrary Waveform Generator

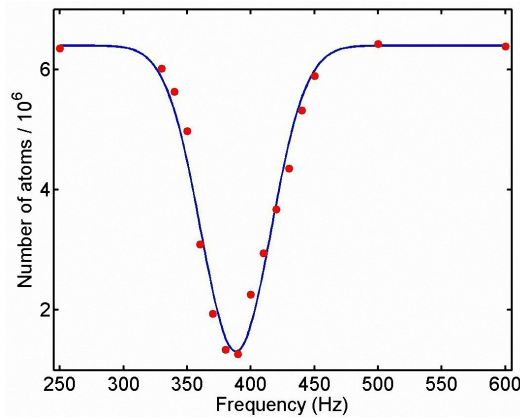


**Figure 3.12:** Measurement of the transverse trap frequency of the Cu-Z trap. A sinusoidal modulation is added to the current through the Cu-Z for the full trapping duration of 10s. When the frequency of this modulation matches the trap frequency, atoms are removed from the trap with high efficiency. The plot shows the number of atoms remaining in the trap as a function of the applied modulation, a typical resonance behavior can be seen. The gaussian fit to the data yields a trap frequency of  $\nu = 390\text{Hz}$ .

For a more detailed analysis of the cooling process the trapping potential has to be calculated, which is done in Section 4.2.

### Measurement of the transverse trap frequency

To measure the transverse frequency of the Cu-Z trap a small sinusoidal modulation is applied to the current through the Cu wire for the whole trapping duration, causing a permanent oscillating movement of the trap center. If this oscillation is in resonance with the trap frequency the atoms are very efficiently heated and thus removed from the trap. The number of atoms remaining in the trap measured as a function of the frequency of the applied modulation yields the trap frequency, as is shown in Figure 3.12. For the uncompressed Cu-Z trap the result is  $\omega_t/2\pi = 390\text{Hz}$ .

The advantage of this method is that the oscillation of the atoms in the trap needs not be observed directly. This makes it suitable for the large trap frequencies of the chip traps, which routinely reach values of  $\omega/2\pi > 1\text{kHz}$ . We plan to integrate an automated measurement routine using this technique into the experiment software, that can be applied to all traps occurring in the experiment. Since the transverse trap frequency is one of the most important parameters of any trapping potential, it is of great interest to measure it, especially for the highly compressed chip traps. Comparison of the experimentally obtained results with the calculated values from model potentials will also help to improve the accuracy of the models we use.

### 3.2.5 Chip experiments

After the first rf-cooling phase in the Cu-Z trap, the atoms are transferred to traps generated by the chip wires. The chip traps and the experiments carried out with them are the topic of the next chapters.

Typical experiment durations for the chip traps are 1 – 5s, depending on what traps are used and at what temperature the atoms are transferred to the chip. In

general the duration of the experiments is limited by the heating of the chip wires. Usually, we monitor the resistance of the used wires during the experiments. We choose the upper values for the currents and the experiment duration in such a way that we observe no change in the resistance above 1% during one experiment run to avoid the risk of permanently damaging the chip structures.

The chip currents are provided by custom built controlled current power supplies with a maximum current of 2A used together with fast switches to allow turn-off times of the order of  $10\mu\text{s}$ .

### 3.2.6 Imaging of the atom distribution

The final step of each experiment cycle is the imaging of the atom distribution. We use two different imaging techniques, *absorption* and *fluorescence* imaging. Absorption imaging measures the attenuation of a laser beam passing through the atom cloud, while fluorescence imaging detects part of the light re-emitted by the atoms after absorption.

#### Absorption imaging

To obtain an absorption image, a pulse of resonant laser light is send through the experiment area onto the imaging optics and is imaged with the corresponding CCD camera. Depending on the distribution of atoms in the beam path, the beam profile will be altered because an amount of light proportional to the number of atoms will be absorbed. After the atoms have dispersed from the imaging area, an image of a second pulse is taken, to obtain the unattenuated beam profile. This serves as a reference and accounts for inhomogeneities in the profile. A third image is taken when all laser light is switched off to measure stray light falling onto the camera (currently only implemented on the vertical imaging system). From these three images the final absorption image is calculated by the following pixel-wise operation:

$$I_{\text{absorp}} = 1 - \frac{I_{\text{withatoms}} - I_{\text{background}}}{I_{\text{withoutatoms}} - I_{\text{background}}}. \quad (3.3)$$

This process is illustrated in Figure 3.13. The final image shows the *column density* of the atom cloud, i.e. a two-dimensional projection of the three-dimensional atom distribution.

The absorption image can be taken at different points of time. So called *in situ* images are taken while the magnetic trapping fields are still on. These images show the actual atom distribution in the magnetic trap (It has to be taken into account that the inhomogeneous magnetic fields present during the imaging cause a spatial dependence of the absorption rate). Because of the high densities of the trapped atoms the atom cloud is usually *optically dense*, meaning that the imag-

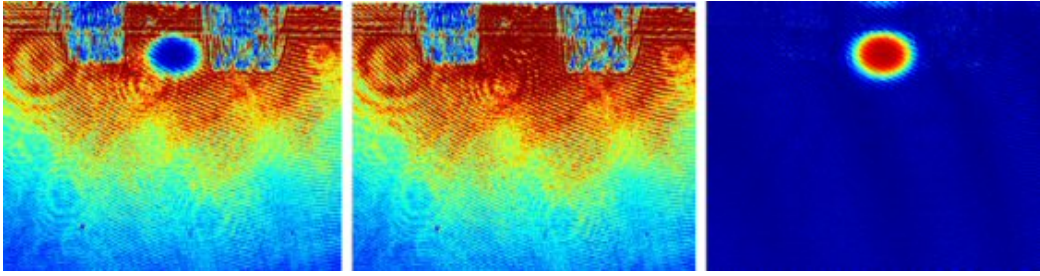


**Figure 3.13:** Demonstration of the image procession for the absorption imaging technique. The image containing the atoms (left) is divided pixel-wise by the image without atoms (center). The result is inverted to produce the final absorption image (right). It can be seen that inhomogeneities in the imaging beam, like the interference rings caused by small detriments in the imaging optics, are removed from the final picture. The atom distribution shown in these pictures is optically dense, completely absorbing the imaging light falling onto it. The structures visible at the top of the images are the bondings of the chip wires to the current leads.

ing light is fully absorbed <sup>7</sup> in the area around the trap center. This prevents a calculation of the number of atoms in the cloud because densities above a certain saturation value can not be differentiated. To avoid this problem the frequency of the imaging beam can be shifted away from resonance (*off-resonance imaging* to lower the amount of absorbed light.

An alternative is to use a *time of flight* (TOF) method. Here, the atom distribution is imaged a certain time after the magnetic trapping fields have been switched off. In this duration the atoms expand ballistically in all directions and fall down because of gravity. When the TOF is chosen long enough to ensure no optical dense areas remain, the number of atoms can be calculated from the total amount of absorbed light [36]. Here also no modification of the images due to magnetic fields occurs. From the speed of the expansion also the temperature of the atom ensemble can be calculated.

### Fluorescence imaging

Light absorbed by the atoms is re-emitted in random direction, a process known as *fluorescence*. Information about the atom distribution can be obtained by measuring the amount of light scattered into a certain solid angle (the camera objective) from each point in space. For this a (near) resonant probe beam is send through the atoms which does not fall onto the camera and an image is taken of the scattered light. Usually we use the imaging beam perpendicular to the camera, but one of the MOT beams can also be used as a probe beam of

<sup>7</sup>Because of the exponential character of the absorption law,  $I = I_0 e^{-Dx}$ , the light is never fully absorbed theoretically. In practise though no differentiation is possible anymore for absorption close to unity. An atom cloud is usually called optically dense when the absorption is larger than 95%

higher intensity.

In our experiment we use this imaging method mostly for the vertical camera. Since it does not require a beam reflected from the chip surface the fluorescence images do not show the chip structure visible in the absorption images, which can make an exact determination of the atom cloud difficult.



## 4 Bose-Einstein condensation in microtraps

In this chapter we will describe the production of Bose-Einstein condensates (BEC) in our experiment. The first BEC was realized in the Cu-Z trap introduced in the last chapter. This served as an initial test that our experimental conditions are suitable and our evaporative cooling is sufficiently efficient to cool and compress atoms to the required phase space density for BEC. After the successful transfer of atoms to magnetic traps created with the atom chip, we also achieved BEC in these potentials. We have subsequently optimized the procedure so that sizable BECs of several  $10^4$  atoms are routinely available in various chip wire based traps. The condensates form a coherent matter wave source for subsequent experiments in the surface potentials of the atom chip.

This chapter starts with an introduction to the theoretical aspects of Bose-Einstein condensation which are of importance for our experiments (Section 4.1). We will then describe the BEC production in the Cu-Z trap (Section 4.2). In Section 4.3 we will discuss the transfer of atoms to chip-based potentials, while in Sections 4.4 and 4.5 the BEC production procedure in the  $100\mu\text{m}$ -wire and the  $10\mu\text{m}$ -wire chip traps are described.

### 4.1 Bose-Einstein condensation in an external potential

The most basic approach to the process of Bose-Einstein condensation is to consider a large ( $N \rightarrow \infty$ ) ensemble of ideal bosons confined in a box potential. This calculation was first carried out by Bose [14] and Einstein [35] and can be found in standard textbooks on statistical mechanics (for example [112]).

This approach yields a value for the phase space density  $\phi$  for the onset of condensation:

$$\phi = \tilde{n}\lambda_T^3 = \zeta\left(\frac{3}{2}\right) \approx 2.612. \quad (4.1)$$

Here  $\tilde{n}$  is the average particle density,  $\zeta$  is the Riemann zeta function, and  $\lambda_T$  is the *deBroglie wavelength* of the particles, which is given by

$$\lambda_T = \left( \frac{2\pi\hbar^2}{mk_BT} \right)^{1/2}. \quad (4.2)$$

It turns out that Equation 4.1 remains valid for realistic gases and arbitrary trapping potentials and thus is a fundamental condition. Its physical interpretation is that the quantum nature of the particles becomes important when the inter-particle distance is of the same order as the extension of the particle wave functions.

For the calculation of other important quantities, like the transition temperature, this basic approach only yields approximate results. To better match experimental results, more realistic treatments are required. Most importantly the atom-atom interaction and the effect of the confining potential have to be taken into account. Detailed description of these treatments can for example be found in [103]. Here, only the important consequences for our experiments are discussed.

#### 4.1.1 Effects of the confining potential

The spatial variation of the trapping potentials used in experiments modifies both the critical temperature and the condensate fraction. Usually the effective volume available to atoms of a certain energy is smaller than in a box potential. Therefore the mean density is larger, which in turn results in an increase of the critical temperature. Also the level spacing and the ground state energy depend on the potential type, which results in different densities of energy states.

A derivation of the important thermodynamical properties for an arbitrary three-dimensional power-law potential can be found in [5]. Of interest to us is the case of a three-dimensional harmonic potential. The critical temperature in that case is given by

$$k_BT_c = 0.94\hbar(\omega_x\omega_y\omega_z)^{1/3}N^{1/3} \quad (4.3)$$

while the fraction of atoms in the condensate phase is given by

$$\frac{N_0}{N} = 1 - \left( \frac{T}{T_c} \right)^3. \quad (4.4)$$

These results differ from those obtained for the ideal gas. Most noticeable the transition temperature is raised by the external potential, slightly facilitating the condensation process.

#### 4.1.2 The Gross-Pitaevskii equation

Even in dilute ensembles in magnetic traps the interaction between particles cannot be neglected. The standard method of treating a large number of interacting



particles is to adopt a mean-field approach, describing the force acting on a single particle by introducing an average potential generated by the other particles. The *condensate wavefunction* is introduced as the product of the single particle wave functions:

$$\Psi(\mathbf{r}_1, \dots, \mathbf{r}_N) = \prod_{i=1}^N \Phi(\mathbf{r}_i). \quad (4.5)$$

The mean-field treatment then leads to a differential equation for the condensate wave function, the *Gross-Pitaevskii equation* (GPE) [103]:

$$\left[ -\frac{\hbar^2}{2m} \nabla^2 + V_{ext}(\mathbf{r}) + gN |\Phi(\mathbf{r})| \right] \Phi(\mathbf{r}) = \mu \Phi(\mathbf{r}). \quad (4.6)$$

This has the form of a Schrödinger equation with an effective potential given by the sum of the external potential and a non-linear interaction potential  $gN |\Phi(\mathbf{r})|$ . The *interaction parameter* is given by

$$g = \frac{4\pi\hbar^2 a}{m} \quad (4.7)$$

where  $a$  is the s-wave scattering length. It should be noted that the GPE is only valid when the condition  $\tilde{n}|a|^3 \ll 1$  is fulfilled, i.e. when the inter-particle distance is much larger than the scattering length.

### 4.1.3 The Thomas-Fermi approximation

When the different terms in the GPE (Equation 4.6) are compared, it turns out that even for typical trapping potentials and atom densities the interaction term dominates the kinetic term. Typical numbers are  $E_{int}/E_{kin} \approx 10^4$ , which allows to completely neglect the kinetic term in the GPE. This is known as the *Thomas-Fermi approximation*. With this simplification the solution to the GPE can be obtained easily:

$$n(\mathbf{r}) = |\Psi(\mathbf{r})|^2 = \frac{\mu - V_{ext}(\mathbf{r})}{g}. \quad (4.8)$$

This results in the density distribution of a condensate being an inverted parabola. With the chip-based magnetic micro traps regimes can be reached where the Thomas-Fermi approximation is no longer valid. This happens when the confining potential becomes so anisotropic that it can be treated as one-dimensional. This will play a role for some of the surface experiments described in Chapter 5 and will be discussed there. For the initial condensation experiments described in this chapter the Thomas-Fermi approximation is fully valid.

#### 4.1.4 Observation of Bose-Einstein condensation

To observe the creation of a BEC usually TOF images of the ensemble after an expansion of a few milliseconds are taken. The expansion of a condensate differs from that of a thermal cloud in two ways, which can be used to identify a BEC.

##### The Density Profile

From Equation 4.8 we know that the density distribution of a BEC has a parabolic shape. On the other hand for thermal atoms the bosonic nature of the particles plays no role and they can be assumed to follow the classical Boltzmann distribution, i.e.  $n = n_0 \exp(-V_{ext}/k_B T)$ . Thus the density distribution of a thermal cloud in a harmonic potential is a Gaussian. These profile shapes can be easily observed in TOF images of the expanded atom cloud. By fitting the measured density profiles a differentiation between BEC and thermal cloud is possible.

It should be noted that strictly speaking a pure condensate is only achieved for  $T = 0$ . For finite temperatures there always exist a fraction of thermal atoms. A sample with condensate and thermal fractions of similar size is called *bimodal*. The density profile is then given by a superposition of a Gaussian and a parabola. In practise, one speaks of a 'pure' condensate when the thermal fraction is smaller than  $\sim 10\%$ .

##### The aspect ratio

Due to the anisotropy of the confining potential the trapped sample has a 'cigar' shape. For the expansion of a thermal cloud this does not matter. According to the equipartition principle the kinetic energy of the atoms will be distributed equally over all degrees of freedom, resulting in an isotropic expansion. The atom-atom interaction can be neglected for thermal atoms.

It was already stated that for a BEC the opposite is the case. At the moment of release from the trap, the energy of the sample is stored mostly as interaction energy, which will be converted to kinetic energy during the expansion. The behavior of the BEC during the expansion is given by the *hydrodynamical description* [21]. The important result is that the energy of the condensate will be anisotropically distributed onto the different degrees of freedom. More precisely, the cloud will expand faster in directions in which it was more strongly confined in the magnetic trap. Hence the aspect ratio of the expanded BEC after a certain characteristic time  $\tau$  will be the inverse of the aspect ratio of the trapped sample. In our case this means that a BEC after a time of expansion will be strongly elongated in the vertical direction. This effect allows a direct identification of a BEC from the absorption images.

## 4.2 BEC in the Cu-Z trap

As has been stated in the last chapter, the starting point for all chip experiments is the magnetic trap generated by the Cu-Z structure underneath the chip. This was the first trap to attempt Bose-Einstein condensation in, even before any loading of atoms to the chip traps was tried. Realizing BEC in this trap served to show that our experiment setup was sufficiently stable and suited for the later chip experiments.

### 4.2.1 The trapping potential

As has been described in Section 2.3.3, the calculation of all wire trap potentials is complicated because of the finite size and rectangular shape of the wires. This is especially true for the Cu-Z trap because of the comparably large size of the wires. Here, the inhomogeneous current density especially at the bends of the wire are of importance.

In practise, we use simplified models for the potential calculation whose complexity is chosen according to the required precision for the appropriate experiments. Specifically for the Cu-Z trap a basic model using infinitely thin wires is sufficient because of the large distance between the trap center and the wire ( $\sim 2\text{mm}$ ).

The model can be improved by varying the distance of the outer leads and allowing a slight tilt of the central wire to simulate the main current flow in the Z. This calibration is done so that the model prediction for trap frequencies and field strength at the trap center (the trap bottom) are consistent with measurements of these values. How we measure the trap frequencies has been described in Section 3.2.4, the trap bottom can be measured directly during the evaporative cooling process (see below). Results obtained with this calibrated model are shown in Figure 4.1 and are found to be in good agreement with the experiment. The calculated trap frequencies for typical parameters used in the experiment are  $\omega_l/2\pi \simeq 40\text{Hz}$  and  $\omega_t/2\pi \simeq 400\text{Hz}$ . Using Equation 4.3 this gives a transition temperature of  $T_C \approx 0.7\mu\text{K}$  assuming  $3 \times 10^5$  atoms in the trap before condensation starts.

### 4.2.2 The evaporative cooling process

After the initial loading of the Cu-Z trap (Section 3.2.4), the potential is changed to facilitate the evaporative cooling process. While the current in the wire remains fixed at 60A, the bias field is ramped up to 45G in 1s to compress the trap. This compression increases the collision rate of the atoms, speeding up the rethermalization during the cooling process.

At the same time the external Ioffe-field is increased from the initial 24G to a value in the range of 30–32.5G, the effect of this is shown in Figure 4.2. Because the external Ioffe field is opposed to the field created by the outer wires of the

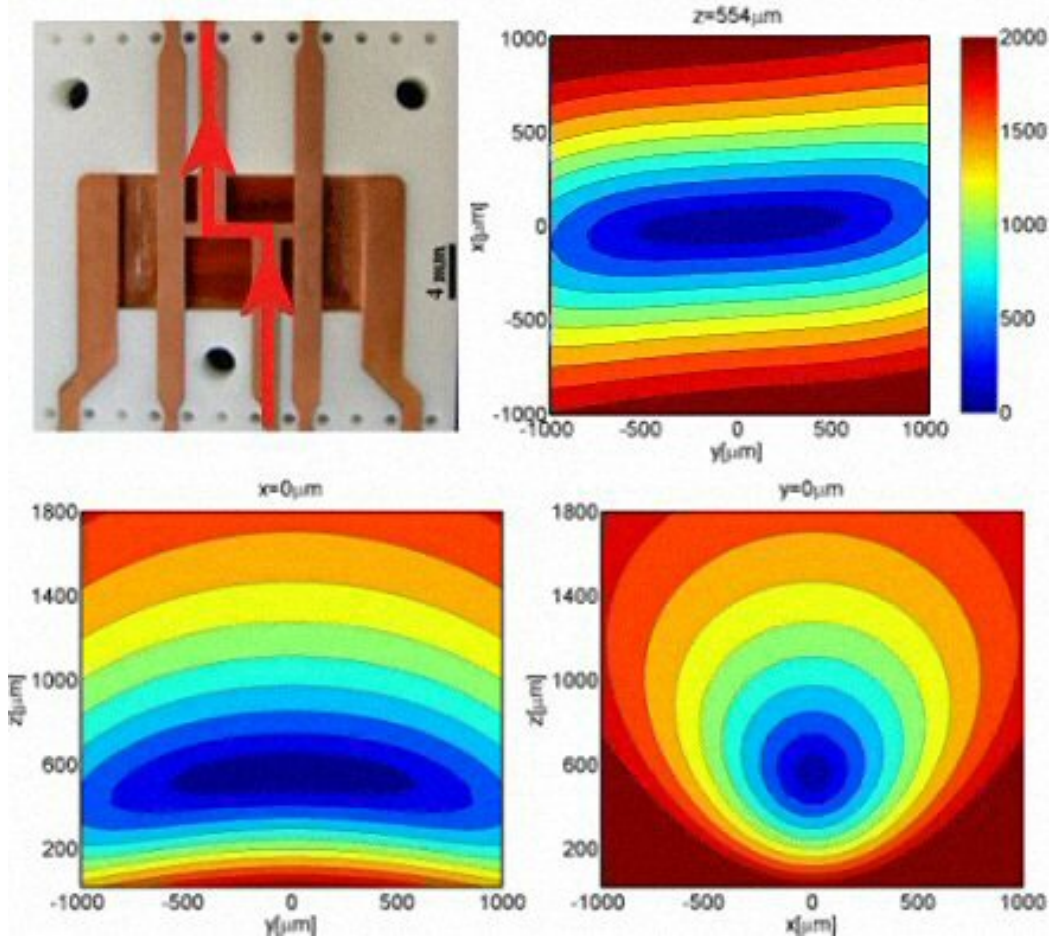


**Figure 4.1:** Trapping potential generated by the Cu-Z trap for typical parameters of 60A, 45G, and 32G for the current in the wire, bias field strength, and Ioffe-field strength, respectively. **Top left:** Photograph of the Cu-structure. The current flow through the small central Z used for this trap is indicated by the red arrows. **Top right:** Contour plot of the potential in the plane parallel to the chip surface at the position of the trap minimum. The potential energy is shown in units of  $\mu\text{K}$ . The central bar of the Z points in the y-direction. The slight tilt of the trap compared to this orientation can be seen. **Bottom left:** Side view of the potential in the central plane perpendicular to the chip and parallel to the central bar of the Z. The elongation of the potential on the longitudinal direction can be seen. **Bottom right:** Potential in the central plane perpendicular to the chip and parallel to the outer wires of the Z, showing the radial profile of the potential. The trap center can be seen to be located about  $600\mu\text{m}$  away from the chip surface.

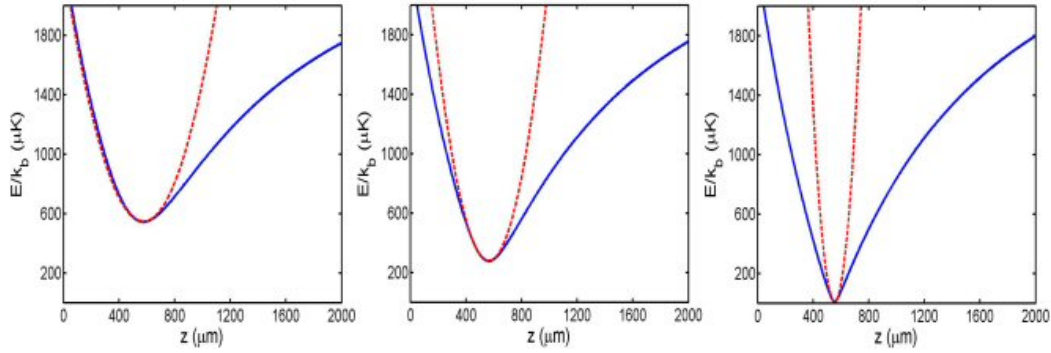


**Figure 4.2:** Cu-Z trap potential for different Ioffe-fields (from left to right 24G, 28G, 32G). Bias field and current are fixed at 45G and 60A. It can be seen how the trap bottom is lowered with increasing Ioffe-field, while the position of the trap center remains basically fixed. The red dotted lines show the harmonic approximation of the trap around the minimum. The harmonic area of the potential decreases from left to right, outside this area the potential is approximately linear.

Z, this increase reduces the total Ioffe field, i.e. the field strength at the trap center. The important aspect for the cooling process is that this also decreases the area around the minimum where the potential is harmonic. Further out from the center the linear slope of the side guide potential is recovered. As explained in Section 3.2.4 this improves the efficiency of the evaporative cooling. One has to take care not to reduce the trap bottom to zero to avoid atom loss due to Majorana spin flips.

The actual value of the trap bottom can directly be measured with the rf-sweep. The final frequency of the rf-sweep is lowered until all atoms are removed during the sweep. This frequency value can then be transformed into the field strength at the minimum by using Equation 3.2. Alternatively the trap bottom can be approached from below by using a constant frequency that is increased during each experiment run. As long as the frequency lies below the resonance no effect is observed, until the resonance is hit and all atoms are removed.

Typical values we choose for the trap bottom range from 0.1G to 1G, which is equivalent to final frequencies between 70kHz and 700kHz. While small trap bottoms increase the efficiency of the cooling process, higher values reduce the frequency span that must be covered by the rf-sweep and help to avoid field zeros during the transfer to the chip traps. Thus for the preparation of cold thermal atoms for transfer to the chip traps a trap bottom of  $\sim 1$ G turned out to be most convenient. For the reliable production of BECs in this trap though, the trap bottom has to be reduced to below  $\sim 0.5$ G with lower values being more efficient.

### 4.2.3 Results

The result of a typical rf-sweep is shown in Figure 4.3. During the cooling the phase space density increases by eight orders of magnitude until condensation is achieved. The atom density increases from  $10^{12}\text{cm}^{-3}$  to  $10^{14}\text{cm}^{-3}$ , while the temperature drops from  $350\mu\text{K}$  to  $\leq 1\mu\text{K}$ . Starting with  $5 \times 10^7$  atoms, typically condensates of  $10^5$  atoms are reached. The transition to BEC is shown in more detail in Figure 4.4. The condensate shows the elongated shape predicted by the mean-field approach (Section 4.1.4). Typical transition temperatures we measure range from  $0.5\mu\text{K}$  to  $1\mu\text{K}$ , which is what we expect from the calculated trapping potential.

Since the first realization of condensation in this trap we have optimized both the parameters and the implementation of the rf-cooling, reducing noise effects and increasing the cooling efficiency. BEC production in this trap is now virtually always possible (as long as the initial number of atoms in the trap does not drop significantly below  $3 \times 10^7$ , in which case a readjustment of the MOT is necessary).

## 4.3 Transfer to the chip

After the pre-cooling stage in the Cu-Z trap the atoms can be transferred to a chip wire trap. In almost all our experiments the initial chip trap, into which the atoms were loaded, was generated by the  $100\mu\text{m}$  Z-wire. Because this is the largest wire on the chip, it provides the deepest possible trap, making it possible to transfer relatively hot atoms ( $\sim 30\mu\text{K}$ ) to the chip. For experiments with other chip-based traps the atoms were then transferred in a second step between the chip traps.

Recently we have tested the direct loading of cold atoms directly to the smaller  $10\mu\text{m}$ -wire trap, which turned out to be of equal efficiency compared to the two-step transfer scheme. This will be discussed in Section 4.5, here we will focus on the transfer to the  $100\mu\text{m}$  Z-wire trap.

### 4.3.1 The transfer procedure

The transfer to the chip is carried out in 1s. The current through the Cu-wire is ramped down to zero, while simultaneously the current in the chip wire is ramped up to 2A. It turned out to be preferable not to ramp up the chip current from zero, but instead to already have a chip current of 1A at the start of the transfer, to provide a potential barrier of sufficient height toward the chip surface. This prevents the atom cloud from touching the chip surface during the transfer. Therefore the current through the chip-Z is ramped up to 1A together with the current in the Cu-Z at the start of the Cu-Z trap phase. Although this current is small compared to the 60A in the Cu-wire, it still has a noticeable influence on the trapping potential because of the smaller distance to the trap center. It both

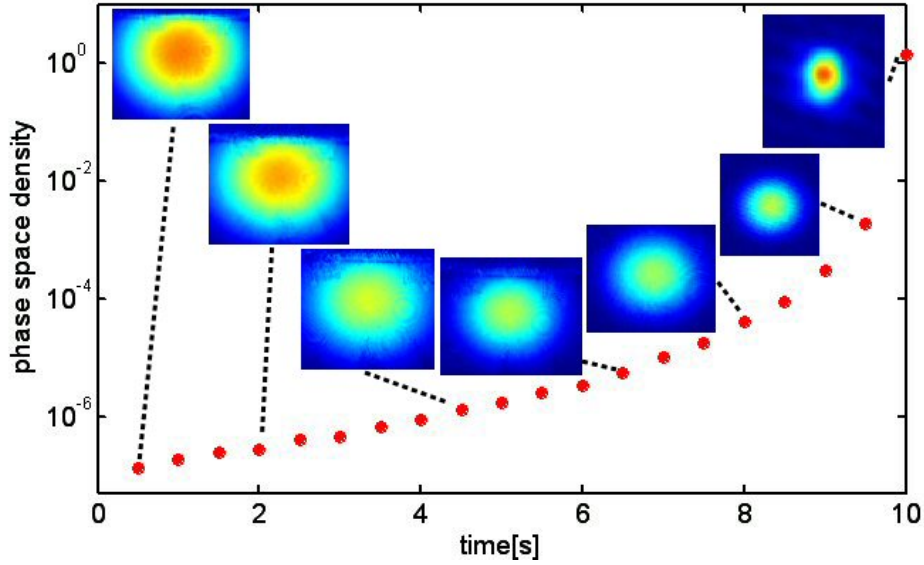


**Figure 4.3:** Evolution of the phase space density during the ten seconds of evaporative cooling in the Cu-Z trap for standard trap parameters ( $I = 60\text{A}$ ,  $B_{bias} = 45\text{G}$ ,  $B_{Ioffe} = 32\text{G}$  and starting number of atoms of  $5 \times 10^7$ ). The phase space density increases from initial values of  $\sim 5 \times 10^{-8}$  by eight orders of magnitude. The insets show the corresponding atom clouds after free expansion of 6ms. The transition to BEC once the phase space density reaches 2.6 can be seen in the last picture.

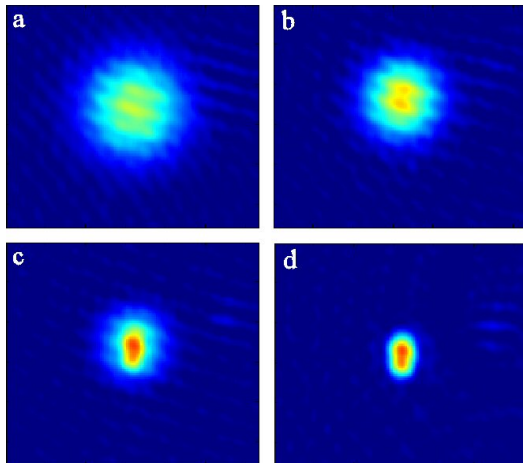


**Figure 4.4:** TOF images of the transition from a thermal cloud to a BEC. From a to d the final value of the rf-sweep is reduced in steps of 10KHz. Picture **a** shows the isotropic shape of an expanded thermal cloud. In **b** the density increase at the center can be observed. In picture **c** the elongated shape of a BEC is visible against a remaining thermal background. Picture **d** shows a pure BEC.

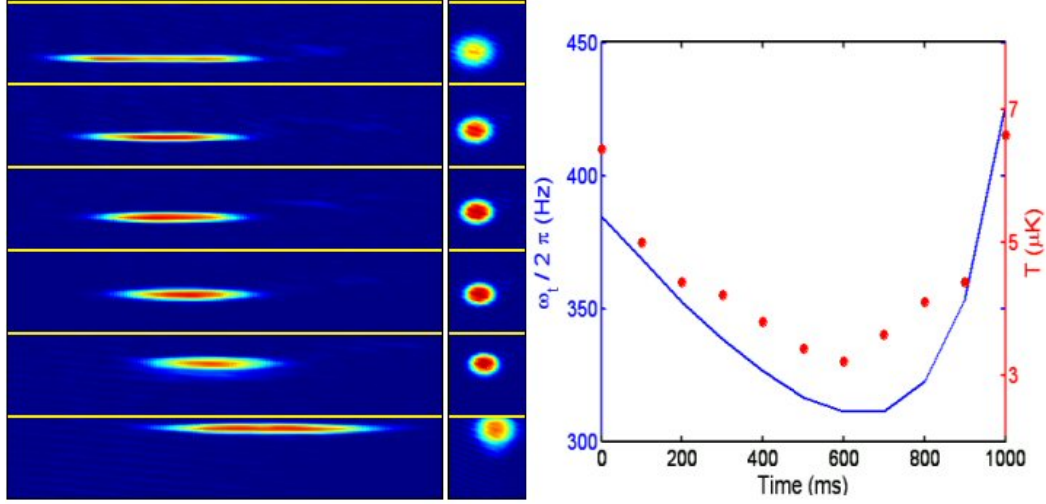


**Figure 4.5:** Sequence of images showing the transfer of atoms to the chip. **Left:** In situ images of the atom cloud. The images are magnified and stretched in the horizontal direction by a factor of four. The movement of the cloud towards the chip can be seen as well as the displacement to the right caused by the misalignment of the two wires. **Center:** TOF images corresponding to the in situ pictures. The decrease of temperature in the middle of the transfer can be seen in the smaller size of the expanded cloud. **Right:** The calculated transverse trapping frequency during the transfer is shown in blue, while the red dots show the measured temperature. The adiabatic cooling effect due to the relaxation of the trap can be seen.

pushes the trap away from the chip and increases the confinement of the potential. Also the b-f field has to be adjusted slightly to account for the additional Ioffe field created by the chip-Z.

The homogeneous fields have to be changed accordingly while the currents are ramped. The bias field is ramped linearly from 45G to 7G, while the b-f field is ramped from 32G to 2.5G in the opposite direction (this is done by reducing the field produced in the main b-f coils to 0.5G while the extra b-f coils mentioned in Section 3.1.4 keep producing an opposed field of 3G). These final values of the ramps are chosen in such a way that the trap frequencies of the resulting chip trap are comparable to the Cu-Z trap.

The transfer is slightly complicated by the fact that the centers of the two traps do not overlap. Instead the chip trap is accidentally displaced by  $200\mu\text{m}$  in the direction along the central bars of the traps. This increases the possibility of creating a field zero during the transfer because all four outer leads of the Z-wires contribute to the Ioffe field. To avoid such a hole in the potential, the direction of the b-f field is reversed during the transfer, so that it in fact adds to the contribution from the wires.

Images of the transfer are shown in Figure 4.5. The in situ images show the movement of the trap closer to the chip surface and its displacement to the side. It can also be seen that during the transfer the cloud expands radially while it



shrinks along the longitudinal direction. This is accompanied by a decrease of temperature which can be seen in the corresponding TOF images. This behavior becomes clear when the trapping potential during the transfer is calculated. While the longitudinal trap frequency remains roughly constant, the transverse frequency has a minimum during the transfer (Figure 4.5 right). The transverse relaxation of the trap causes adiabatic cooling of the atoms, reducing the temperature but also the atom density. The compression at the end of the ramp increases the atom temperature again. In total we observe a small decrease of phase space density after the transfer (from  $10^{-7}$  to  $10^{-8}$ ), which means that the process is not fully adiabatic. This does not pose a problem though, because the ensuing rf-cooling in the highly compressible chip trap is very efficient and allows the production of similarly sized BECs as in the Cu-Z despite somewhat worse starting conditions.

The transfer was tested for temperatures ranging from  $1 - 30 \mu\text{K}$ , we found it to be of equal efficiency over a range of  $2 - 20 \mu\text{K}$ . For hotter atoms the loss of atoms during the transfer increases, because the finite trap depth allows evaporation from the trap. On the other hand thermal atoms close to  $T_C$  or even condensates are much more sensitive to the small non-adiabaticity of the potential change, which leads to larger heating during the transfer. A transfer temperature of  $\sim 10 \mu\text{K}$  was established as a standard and used for most experiments. The number of transferred atoms in this case is  $1.5 - 2 \times 10^6$  (in accordance with [125]).

### 4.3.2 Adiabaticity of the transfer

From the above discussion it is clear that ensuring the adiabaticity during the transfer is crucial to avoid the loss of phase space density. Extremely non-adiabatic changes of the potential can even cause transitions to other spin states. These transitions can be made visible by a Stern-Gerlach type experiment. For this the current in the chip wire is left on during the time of flight period after the other trapping fields are switched off. This provides an inhomogeneous magnetic field strength in the direction of free fall, causing an additional state-dependent acceleration of the atoms. Hence atoms in different spin states will have moved different distances from the original trapping location at the moment of imaging. Figure 4.6 shows such an experiment for different transfer speeds. It can be seen that too rapid changes of the trapping potential cause a significant fraction of the atoms to undergo non-adiabatic spin state transitions. The transfer time of 1s results from this experiment as the shortest possible time with minimal loss of atoms. A small amount of lost atoms remains even for longer transfer times, showing that the process cannot be fully adiabatic on experimentally feasible timescales.

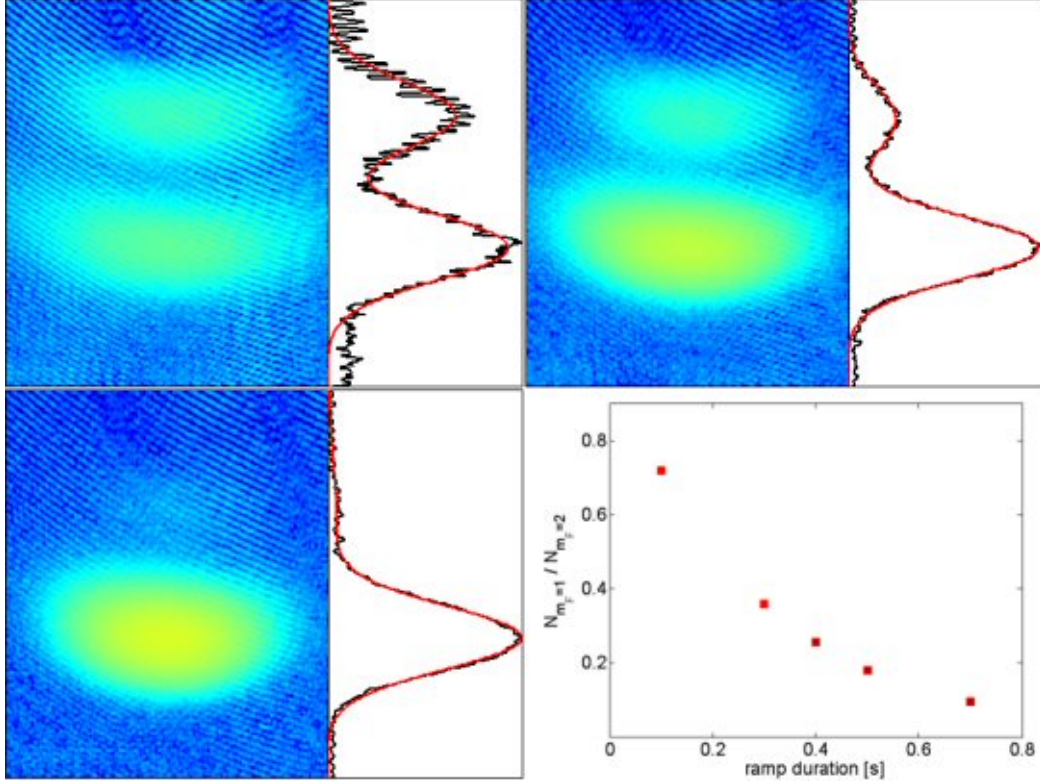


**Figure 4.6:** Stern-Gerlach experiment to test the adiabaticity of the atom transfer to the chip. The chip-Z current is left on during the time of flight of 12ms causing a state-dependent acceleration. The two clouds visible in the images correspond to atoms in the  $m_F = 2$  and  $m_F = 1$  state. Transfer times for the three images were 0.1s, 0.4s, and 0.7s respectively. The double Gaussian fits to the density profiles give the ratio of atoms in both states shown in the plot.

## 4.4 BEC in the $100\mu\text{m}$ -Z chip trap

The first goal after successful transfer to a chip trap had been accomplished was to realize BEC in this trap. The procedure is in principle equivalent to the cooling process in the Cu-Z trap, only that here the cooling can be done faster because of the steeper confinement of the trap and the lower starting temperature.

### 4.4.1 The potential

The trap formed by the chip-Z has essentially the same shape as the Cu-Z trap. The distance of the trap center to the wire is now much smaller, though ( $\sim 200\mu\text{m}$  for typical parameters). This distance is comparable to the width of the wire, so that it has to be taken into account for an accurate calculation of the potential. The wire height of  $3.1\mu\text{m}$  on the other hand can be neglected for the condensation experiments.

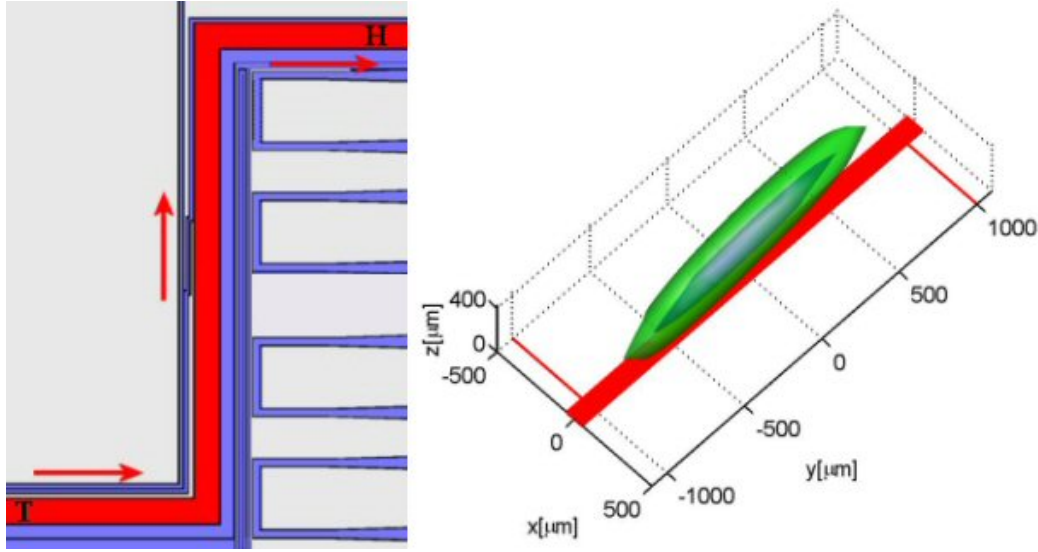


**Figure 4.7:** **Left:** Layout of the 100 $\mu$ m-Z on the chip. The arrows indicate the direction of the current flow. **Right:** Calculation of the resulting trapping potential. The red lines indicate the wires used for this model. The Z is modelled by thin wires of finite length for the outer parts and a flat broad wire of infinite length for the center part. The contours show surfaces of constant potential energy ( $E/k_B = 450\mu\text{K}$  for the green,  $E/k_B = 300\mu\text{K}$  for the blue surface).

To simplify the model only the central part of the wire is assumed to be broad, while the outer leads are approximated by thin wires. This is valid because of the distance from the outer wires to the trap center. To reduce the complexity of the potential calculation the central bar is assumed to be infinitely long, because then equations 2.17 and 2.18 can be used. Since the area of interest is directly above the central wire this does not change the result significantly.

The calculated potential is shown in Figure 4.7. While the overall shape of the potential is the same as for the Cu-Z the chip trap is much more elongated because of the stronger radial confinement. Typical transverse trap frequencies are  $\omega_t/2\pi = 1\text{kHz}$ , whereas the longitudinal frequency is of the order of  $\omega_l/2\pi = 20\text{Hz}$ . This means the aspect ratio of the atom cloud will be  $\sim 50$ . Calculated transition temperatures are  $\sim 1\mu\text{K}$  for typical number of atoms, the steeper confinement compared to the Cu-Z trap slightly raises this value.

#### 4.4.2 Cooling and condensation

Analogous to the Cu-Z trap the trap is compressed after the initial loading by ramping up the bias field from 7G to 20 – 25G in 100ms, to increase the efficiency of the evaporative cooling. The ensuing steep transverse confinement ( $\omega_t/2\pi \approx 1\text{kHz}$ ) guarantees fast rethermalization of the atoms. The b-f field is adjusted so that it points in the same direction as the Ioffe field produced by the chip wire with a field strength of 1 – 1.5G. In other words the external field is

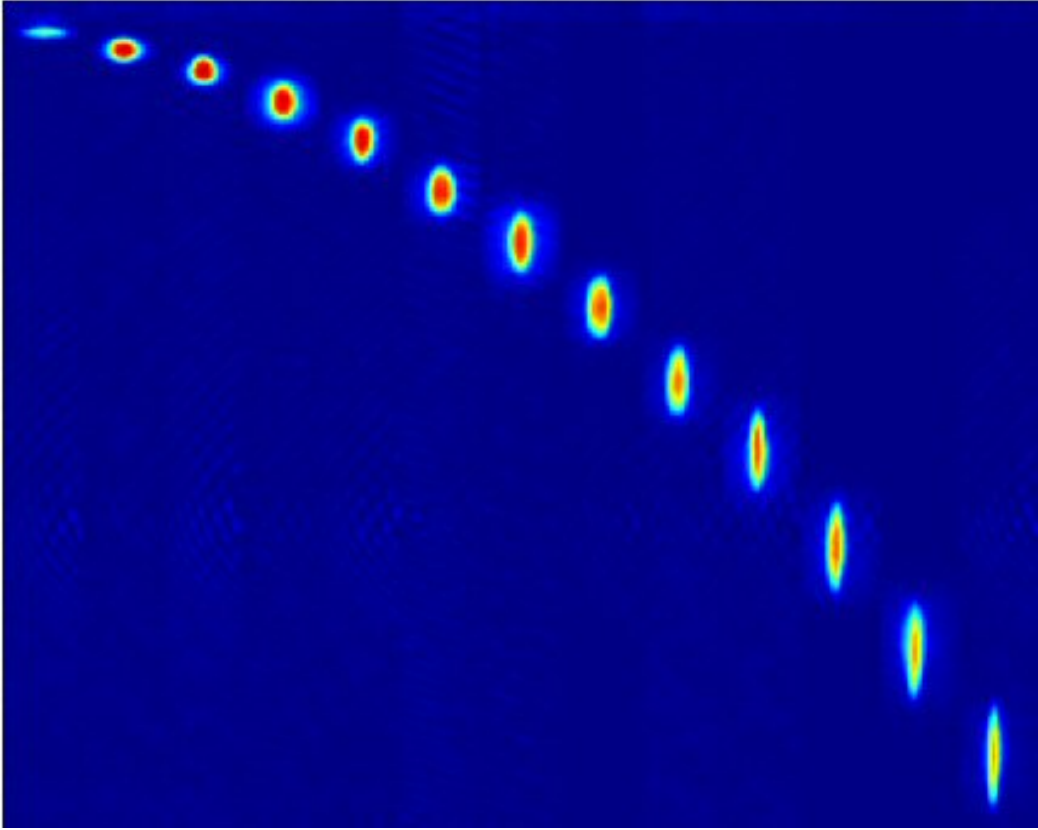


**Figure 4.8:** Evolution of a free falling condensate released from the  $100\mu\text{m}$  chip-Z trap. Sequence of images taken for increasing times of flight ( $2\text{ms}$ ... $26\text{ms}$  in steps of  $2\text{ms}$ ). The elongation in the vertical direction during the expansion, typical for a BEC, can clearly be seen.

used to raise trap bottom. It is usually set to field strengths corresponding to frequencies of  $700 - 400\text{kHz}$ . We choose not to lower the trap bottom further in this trap for two reasons. Firstly, for smaller frequencies we observe some increasing noise effects by the rf-sweep on the current in the chip wire, which make the condensates somewhat less stable. Also in too strongly confining traps three-body recombinations start to play a role as a new loss mechanism [38, 95], which also reduce the final size of the condensates.

After the compression the evaporative cooling is carried out again by an rf-sweep. Its starting frequency depends on the initial temperature at which the atoms are loaded into the trap, usually we set it  $2\text{MHz}$  above the final value of the rf-sweep in the Cu-Z trap to reliably account for any heating during the transfer and compression. The duration of the sweep also depends on the initial temperature, ranging from  $1 - 5\text{s}$ . The lifetime of this trap was measured to be above  $15\text{s}$ , so that trap losses do not play a role for these cooling times. For the typical initial temperature of  $10\mu\text{K}$  a cooling duration of  $2\text{s}$  was found as being most efficient.

The BECs produced in this chip trap are of comparable size to the ones produced in the Cu-Z trap ( $\sim 10^5$  atoms in the pure condensate). The slightly less favorable starting conditions after the transfer are balanced by the more efficient cooling. Figure 4.8 shows the expansion of a BEC released from this trap. The different expansion speeds in the horizontal and vertical direction typical for BEC can be seen in the sequence, which is caused by the asymmetry of the trap. (Section 4.1.4).

## 4.5 BEC in the $10\mu\text{m}$ -wire chip trap

To carry out experiments with specific structures on the atom chip, atoms have to be loaded into the initial potential formed by these structures. In general, cold thermal or even condensed atoms are required. To achieve this two different approaches are possible. The atoms can either be cooled to the desired temperature and then moved to the specific chip potential, or one can first transfer the atoms and then apply another cooling stage in situ.

The first method poses the same problem as the transfer of BECs from the Cu-Z trap to the chip. With decreasing temperature the atoms become much more sensitive to potential changes, resulting in stronger heating effects. Also the maximum transfer time is limited by the BEC lifetime which is much shorter ( $\leq 1\text{s}$ ) than the lifetime of thermal clouds. Even if the transfer is successful, the transfer time has to be subtracted from the remaining lifetime of the BEC in the destination potential, which reduces the maximum experiment duration.

The transfer of thermal atoms between different chip potentials on the other hand is less critical, making the second approach more effective. It must be verified though, that the destination potential is suited for efficient evaporative cooling to produce BECs. The chip potentials are generally more complex than the simple Z-trap and not designed for cooling.

Of particular interest to us is the four-wire guide with the Y-beam splitter interferometer (Section 2.3.2). To observe atom interference atom ensembles with temperatures at most slightly above  $T_C$  are needed in this potential (the interferometer potential and experiments with it are described in Chapter 6). Hence the second chip potential we tried to condense in was a trap based on this chip structure. The successful production of BEC in this trap shows that the in situ condensation in more complex chip potentials is possible.

### 4.5.1 The trapping geometry

To generate a trapping potential, we use only one of the  $10\mu\text{m}$  wide wires, instead of all four parallel wires required for the beam splitter guide. The wire together with its outer lead to the connecting pads (X - G) forms an L-shape which together with a homogeneous bias field creates a side guide potential closed off

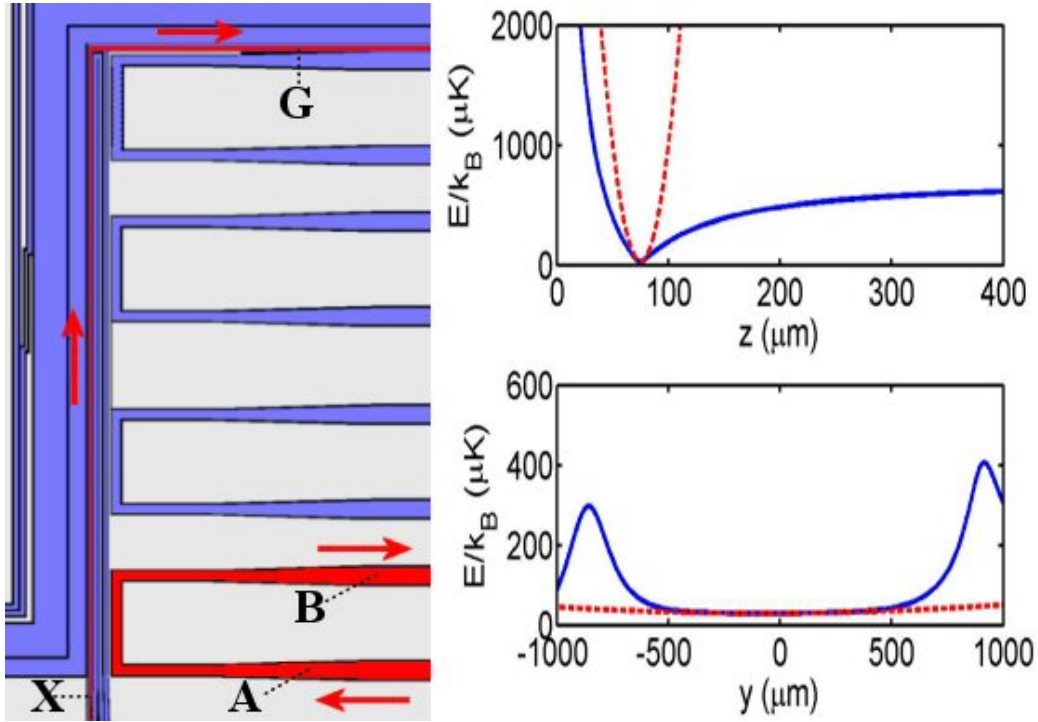


**Figure 4.9:** **Left:** Wire layout in the central area of the atom chip. Shown in red are the two separate wires used to create the  $10\mu\text{m}$ -trap. Basically the L-shaped wire and the upper horizontal bar of the U-wire form a Z-like arrangement. **Right:** Calculated potential for the  $10\mu\text{m}$ -trap in the direction perpendicular to the surface (top) and along the central wire (bottom). In contrast to the normal Z-trap the longitudinal potential is asymmetric because of the different wires used to provide the barriers. The position of the trap center is slightly shifted along the longitudinal axis because of this. The trapping potential in the  $z$ -direction shows no deviation from the standard Z-trap. The red dotted lines again give the harmonic approximation. The extreme longitudinal shallowness of the trap can be seen.

in one direction. To provide a barrier in the other direction, one of the U-shaped wires adjacent to the beam splitter guide can be used, as is shown in Figure 4.9 (left). The U-wire is connected so that the current in the horizontal part closer to the center and in the horizontal part of the L-wire are parallel. This forms a current geometry that resembles a Z-structure. The displacement of one of the outer wires to the other side of the central wire does not change the trapping configuration.

Because of the larger distance to the center the second horizontal part of the U does not destroy the Z-trap. Although the field it creates partially cancels the field created by the other horizontal bar, towards the chip center the contribution from the closer wire is dominant, so that a potential barrier exists. Because the end caps are provided by different structures, the longitudinal potential will be adjustable. This allows a shifting of the trap center from the geometric center of the structure along the central wire.

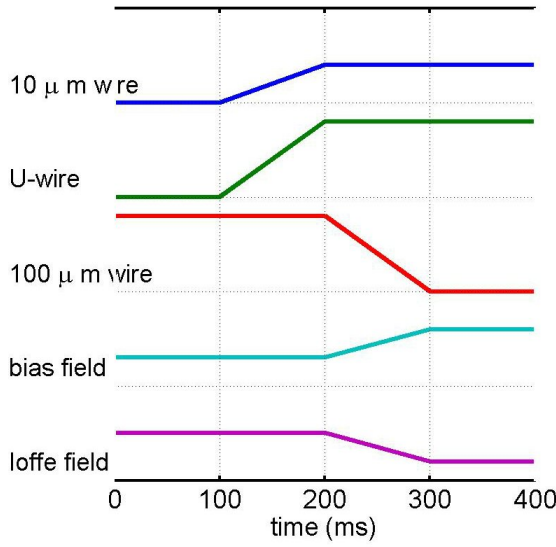


**Figure 4.10:** Typical scheme for loading atoms into the 10 $\mu$ m-trap. The current through the wires generating the final trap are ramped up to the desired values first. Then the current of the initial trap (here the 100 $\mu$ m-trap) is reduced to zero while the external fields are changed to create the desired trapping potential. Only after all changes are done and the potential remains constant, the rf-cooling sweep is started (at  $t = 300$ ms in this diagram).

To calculate the potential, again a model is used that treats the central 10 $\mu$ m-wire as flat but broad, while approximating the remaining wires as infinitely small. For typical distances of 80 $\mu$ m to the surface in the condensation experiments this gives an accurate description of the resulting potential.

This model yields trap frequencies of  $\omega_t/2\pi \approx 2$ kHz and  $\omega_l/2\pi \approx 10$ Hz for typical parameters used in the condensation experiments. The strong transverse confinement is a consequence of the scaling laws given in Section 2.2. Although the current in the chip wire is smaller than for the 100 $\mu$ m-trap the resulting field gradients are larger, because of the smaller distance of the trap to the current carrying wire. Typical field gradients in this trap reach values of  $\sim 2$ kG/cm. Even more extreme values are reached when the trap is moved closer to the surface in the experiments described in the next chapter.

### 4.5.2 Trap loading

The initial loading approach for the 10 $\mu$ m-wire trap was to first transfer the atoms to the 100 $\mu$ m-wire trap and then move them further to the 10 $\mu$ m-wire potential in a second transfer step. This procedure was used for all experiments with this trap described in this thesis. Recently we have tested to directly load atoms from the Cu-Z trap, which turned out to be of comparable efficiency. While the loss of atoms due to the potential changes is smaller for the two-stage transfer, this is compensated by the much shorter transfer time, which reduces the number of atoms lost due to lifetime-limiting effects.

In both cases the transfer procedure follows a general scheme adopted from previous experiments carried out in our group. First, the currents in the wires creating the destination trap are ramped up to the desired values (typically 0.45A in the



10 $\mu$ m-wire and 1A in the U-wire), while the initial potential remains unchanged. Only then the wire currents of the initial potential are ramped down and the external homogeneous fields are changed to the values needed for the new trap. The parameters for the currents and fields for the final potential are usually chosen in such a way that the resulting transverse trapping frequency roughly matches that of the initial trap to minimize the non-adiabaticity of the transfer. In this case that means the bias field is ramped from 7 to 12G, while the Ioffe field (which is pointing parallel to the wire Ioffe field throughout the transfer) is reduced from 2 to 0.3G.

Turning on the wire(s) of the destination trap before ramping down the initial currents guarantees that the trap center cannot move closer to the chip surface during the transfer than its final position, which avoids the crashing of the atom cloud into the chip surface. For this approach to work, it must be verified that the additional currents do not modify the initial potential in such a way as to cause loss of atoms. In this specific case the current of the 10 $\mu$ m-wire has no significant influence at the distance of the 100 $\mu$ m-trap and even less on the Cu-Z trap.

The transfer works efficiently for a temperature range of 1 – 10 $\mu$ K. For hotter atoms the loss during the transfer increases noticeably. Usually temperatures of  $\sim 5\mu$ K were used in the experiments. For both transfer methods the resulting number of atoms at this temperature typically lies between  $5 - 8 \times 10^5$ . This is a slightly worse starting condition than for the 100 $\mu$ m-trap.

### 4.5.3 Results

Once the atoms are loaded into the trap, they are evaporatively cooled to BEC. The rf-sweep in this trap can be as short as 500ms because of the high collision rate in the strongly confined potential. Typically we use a cooling time of 1s, which makes the condensation process more stable.

In the two-step transfer we normally do not add a intermediate cooling stage in the 100 $\mu$ m-trap. Instead the temperature at the end of the Cu-Z trap is set so that after both transfers the atoms have the desired temperature. Because of the more efficient cooling any heating effects from the transfer are compensated.

The Ioffe-field is tuned to produce a trap bottom equivalent to a frequency of  $\sim 700$ kHz, which we found to be the most reliable value for BEC production. Reducing the trap bottom further makes the condensation process less stable, because of atom loss due to three-body effects and increased noise effects [38, 95]. The size of condensates in this trap lies slightly below the values for the other traps. Typical pure condensates consist of up to  $8 \times 10^4$ . The measured transition temperature lies in the range of 1 – 1.5 $\mu$ K, which is consistent with the values calculated from the potential model.



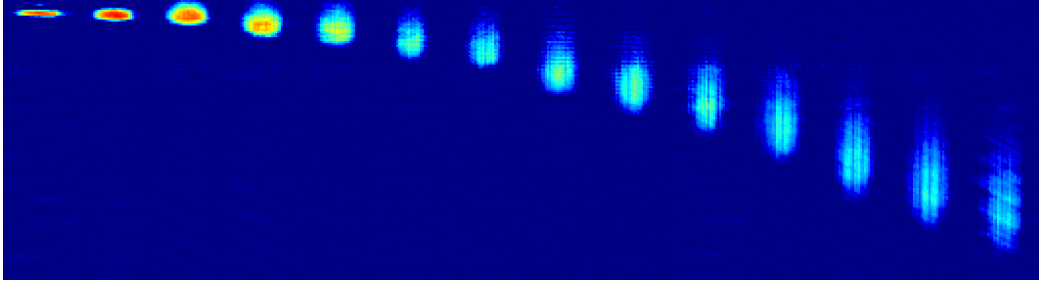


**Figure 4.11:** Series of TOF images of a condensate released from the  $10\mu\text{m}$ -trap. In these experiments a bias field of 14G was used compared to the standard of 12G used normally, which increases the transversal compression of the trap. The released BEC shows the typical vertical elongation during the expansion. In addition a fringe structure in the condensates is visible that changes over time. This may be due to the effective one-dimensionality of the trapping potential.

### One-dimensional condensates

Figure 4.11 shows a condensate released from a  $10\mu\text{m}$ -wire trap that was slightly more compressed transversally than the standard trap (14G bias field instead of 12G). While it shows the general elongation expected from a condensate, also a fringe pattern can be seen in the expanded cloud. This may be the effect of the (quasi) one-dimensionality of the trapping potential.

One speaks of a one-dimensional (1D) trap when its transverse extension is negligible compared to its longitudinal size. Depending on the relevant energy scales for the different directions such potentials are classified into different regimes [99, 105].

When the condition  $\omega_l/\omega_t \ll 1$  is fulfilled the potential is considered to be *quasi one-dimensional*. The potential used in the experiment shown in Figure 4.11 falls into this regime, here the frequency ratio was  $\omega_l/\omega_t \approx 2 \times 10^{-3}$ . In this case the condensate is not phase-coherent over its full length, instead the phase will fluctuate along the longitudinal direction of the trap [106]. After release of the condensate from the trap, this will lead to random interference patterns in the falling condensate. Such patterns have already been observed experimentally [30] and may be what we see in our images. However, the closer analysis of these images is still pending, so that other reasons cannot be excluded yet.

The regime of *1D Thomas-Fermi* condensates is reached when the energy of the transverse ground state  $\hbar\omega_t$  becomes larger than the chemical potential  $\mu$  of the condensate. In that case the Thomas-Fermi approximation is no longer valid for the transverse direction and all atoms are in the transverse single particle ground state. This condition is well fulfilled in the surface experiments described in the next chapter. In fact, even the more severe limit of  $k_B T_C \approx \hbar\omega_t$  is reached. For such strong confinement, transverse excitation do not play a role anymore, and the transverse atomic motion is completely 'frozen' to the single particle zero

point oscillations.

Of great interest is the *Tonks-Girardeau* regime [120, 45]. In this case the atoms form a 1D chain of *impenetrable* bosons, which means that because of the repulsive atom-atom interaction the atoms cannot pass each other anymore and are fixed to their positions in the trap. Interestingly, such strongly interacting bosons behave like weakly interacting fermions. Hence, this can be used to create a system with a tunable transition between bosonic and fermionic particles. Reaching this regime does not depend on the transverse confinement alone, but also on the strength of the atom-atom interaction. Surprisingly the case of strong interaction in 1D confinement is given for low atom densities, so that to produce a Tonks-Gas the number of atoms in the trap has to be reduced. So far Tonks-Gases have only been observed in optical lattices [101]. Atom chips offer a very promising alternative, the required parameters are well within reach for future chip traps [111].

## 5 Fragmentation potentials

A question of great relevance to the atom chip concept is if the proximity of the current carrying structures and the substrate, on which they are based, affect the trapped atoms. To ultimately allow the controlled quantum manipulation of individual atoms, the distance between traps and chips has to be reduced to  $1\mu\text{m}$  and below. It has to be ensured that no surface-induced effects prevent such small surface distances.

A number of such effects have so far been observed and/or predicted, that have to be eliminated to assure the usefulness of atom chips. These effects can be divided into two distinct groups. Firstly, there are dynamic perturbations of the magnetic trapping potential which lead to atom loss, heating, and decoherence. Such fluctuations are caused by thermal noise effects (Johnson or Nyquist noise [72, 97]) in the chip surface and by technical noise in the currents. Theoretical models have been developed to describe these noise effects [60, 61, 62, 59, 58], and they have been measured in various experiments [73, 56, 84]. Secondly, there are static modulations of the trapping potential, which cause a *fragmentation* of the trapped atom clouds into distinct potential minima. This effect has been observed in a number of experiments [41, 77, 73, 37] and is attributed to irregular current flow in the chip wires due to fabrication imperfections.

We have carried out experiments to measure both types of effects in our setup. Here, only the experiments regarding the fragmentation effect are discussed. The surface noise experiments will be discussed in [54].

This chapter starts with a summary of the fragmentation effects observed in other groups (Section 5.1). We also briefly discuss a theoretical model that has been developed to describe these results [123]. Before we turn to our experimental results, in Section 5.2 some aspects specific to experiments close to the chip surface ( $d \leq 1\mu\text{m}$  was realized in our experiments) are discussed. We then present our fragmentation experiments with thermal atoms (Section 5.3) and BEC (Section 5.4). In the course of our experiments it turned out that BECs near surfaces are so sensitive to magnetic field fluctuations that they may be usable as a magnetic field scanning microscope. This possible application is discussed in Section 5.5

## 5.1 Fragmentation observed in other experiments

The observation of fragmentation effects has been reported by a number of groups [41, 77, 73, 37]. Although the surface distance and the atom temperature at which the fragmentation starts to be visible vary slightly between the different experiments, the general effect is the same in all cases. When trapped atoms are moved towards the current-carrying wire that generates the trap a splitting of the atom cloud along the longitudinal direction into fragments is observed. A summary of the results that have been published so far is given in Table 5.1.

To determine the origin of the observed disorder potentials, various experiments have been carried out which proved conclusively that the fragmentation is caused by inhomogeneous current flow in the trap-generating wire. This was first shown by the Tübingen group [41], who observed that an inversion of the current direction in the wire leads to an inversion of the disorder potentials. The same potential inversion was observed in the case of inverted external Ioffe field  $B_{\parallel}$ , so that necessarily longitudinal field components generated by the wire are responsible for the disorder potentials.

Other surface effects were ruled out as a cause of fragmentation by an experiment carried out by the MIT group [78]. The comparison of a magnetic trap and an optical trap with nominally equal parameters close to a surface showed that fragmentation is only observed in the magnetic trap, while the optical trap showed the expected homogeneous density profile. This again points to the electric current as the source of the disorder potentials.

Based on these experimental results a model was developed that allows an analytical calculation of the disorder potentials [123]. In general, there are two main effects that can cause non-straight current flow in a straight wire. These effects are illustrated in Figure 5.1. The inhomogeneous current flow can be attributed either to local conductivity fluctuations in the (bulk) metal the wire is made of, or to surface roughness of the wire edges resulting from the production process. The theoretical model, which main results are briefly introduced here, only con-

Group	Surface distance	Temperature	Disorder field strength ( $\Delta B/B$ )
Tübingen	$\leq 250\mu\text{m}$	$1 - 10\mu\text{K}$	$\sim 3 \times 10^{-4}$ at $h \approx 100\mu\text{m}$
MIT	$\leq 150\mu\text{m}$	$\sim 1\mu\text{K}$	-
Sussex	$\leq 100\mu\text{m}$	$\sim 1 - 5\mu\text{K}$	$\sim 10^{-3}$ at $h = 27\mu\text{m}$
Orsay	$\leq 100\mu\text{m}$	$0.4 - 2.2\mu\text{K}$	$\sim 6 \times 10^{-4}$ at $h = 33\mu\text{m}$

**Table 5.1:** Summary of the fragmentation observations in different groups. In all experiments the surface distance at which the fragmentation starts is two orders of magnitude larger than desirable distances for future atom chip implementations. Even at such comparably large distances the strength of the observed disorder potentials severely limit a controlled manipulation of ultracold atoms.

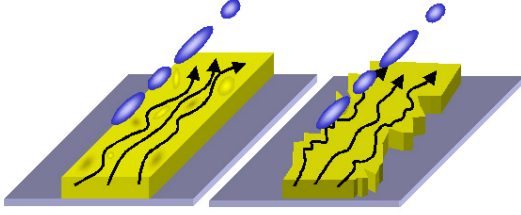


**Figure 5.1:** Different models for the inhomogeneous current flow in a straight wire. **Left:** Inhomogeneous conductivity of the bulk material gives rise to an inhomogeneous current density distribution. **Right:** Irregular surface roughness of the wire leads to strong deviations of the current flow near the wire edges.

siders the second effect, i.e. irregular wire edges.

The assumptions made in the model are small deviation of the wire edges from the ideal position compared to the width  $W$  of the wire, homogeneous conductivity of the wire material, and negligible height fluctuations of the wire whose contribution is much smaller than that of width variations. For surface distances  $h > W/2$  a scaling law for the disorder potential is obtained:

$$\Delta B(h, F_0) \propto \frac{I}{h} \left( \frac{F_0}{h^3} \right)^{1/2}. \quad (5.1)$$

Here  $F_0$  is the wire boundary fluctuation correlation function, which is constant in the case of random (white noise) fluctuations. Since the trapping field of a wire scales as  $B \propto h^{-1}$ , the relative strength of the disorder potential scales as  $\Delta B/B \propto h^{-3/2}$ .

The calculated frequency spectrum of the disorder potential is peaked at nonzero wave vectors  $k$  even under the assumption of random fluctuations (white noise). The peak position depends on the surface distance as  $k = 1.3/h$ . This is due to the fact that high frequency fluctuations are damped more quickly with distance than slow ones. On the other hand long wave length fluctuations are suppressed because uniform shifts do not contribute to the disorder potential.

These scaling laws are only valid as long as  $h > W/2$ . For a closer approach to the wire, the potential fluctuations increase less strongly, because the distance to the wire edges decreases less rapidly. The model accounts for this by a geometry factor that can only be calculated numerically.

The agreement of this model with the observed fragmentation results was verified in [37]. Here, the wire above which the fragmentation experiments had been carried out, was removed from the apparatus and the wire edge fluctuations were directly measured by means of a scanning electron microscope (see images in Figure 2.6 in Section 2.3.1). These measurements were used to calculate the disorder potentials according to the above-described model and the results were found to be in good agreement with the observed density profiles of the fragmented atom clouds.

In our experiment, however, we observe deviations from this model's predictions for small surface distances. As will be shown in Sections 5.3 and 5.4 we were able to reach surface distances  $h \ll W$ , at which conductivity fluctuations in the bulk material can no longer be neglected. We are currently in the process of using the

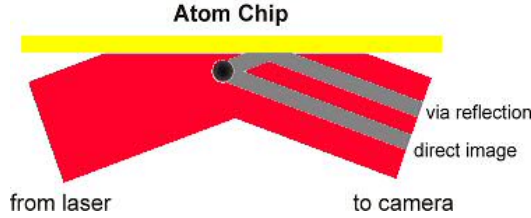


**Figure 5.2:** Absorption imaging of an atom distribution close to the chip surface. The slightly inclined imaging beam is reflected from the surface, which results in the atom cloud absorbing two different parts of it, one before the reflection and one after. The distance between the two images of the cloud is  $2h$  (times the imaging magnification). The angle between light beam and surface is exaggerated in this schematic. In the experiments it is usually of the order of 20mrad ( $\approx 1\text{deg}$ ).

obtained data to develop a refined model that takes into account both wire edge and bulk material effects.

## 5.2 Atom distributions near the chip surface

Before we turn to the analysis of our results, we will briefly discuss the experimental procedure of bringing atom clouds close to the chip surface and some techniques that we developed to reliably measure quantities like the surface distance and the atom temperature for very small samples.

It follows from the scaling law for the height of a wire trap  $h \propto I/B_{bias}$  (Equation 2.12), that both a decrease of the wire current and an increase of the bias field strength allow a linear decrease of the surface distance. From Equation 2.13 it can be seen that the field gradient scales as  $B' \propto B_{bias}^2/I$ . This implies that the trap frequency  $\omega_t$  increases as the surface is approached in either case, but more strongly if  $B_{bias}$  is increased than if  $I$  is reduced. Hence, in most of our experiments, we chose  $I$  as the parameter to be varied to bring atoms close to the chip surface. Limiting the increase of  $\omega_t$  is desirable, because otherwise density-dependent loss mechanism, such as three-body recombination processes, potentially mask height dependent effects.

In principle it is possible to simultaneously vary  $I$  and  $B_{bias}$ , so that  $\omega_t$  remains constant for all heights. The reason why we chose not to use such a combined approach is to minimize the error in the height determination process. While it is possible to measure the current in the wire directly with high precision, the bias field strength can only be calculated from the current through the coils and the coil geometry, which results in a much larger inherent error. If  $B_{bias}$  is left constant during the approach to the surface, a method exists to determine it indirectly, which will be explained in Section 5.2.2. Hence the sole variation of the wire current allows the most precise determination of the surface distance  $h$ .

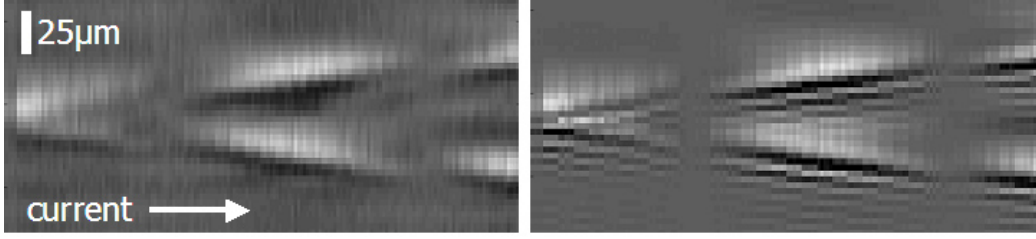


**Figure 5.3:** **Left:** Experimentally observed in situ transverse absorption profiles of BECs during a current (height) scan. Every column corresponds to a different current, the profiles are obtained by integrating over the longitudinal direction (parallel to the surface). The increasing distance between direct and reflected image can be seen. **Right:** Numerically determined profiles with atomic density and surface distance  $h$  as free fitting parameters. The good agreement to the experiment allows to use the fitted values of  $h$  as height measure. The higher resolution in the calculated image is due to the limited resolution of the imaging.

### 5.2.1 Imaging near reflecting surfaces

The presence of a reflecting surface near the trapped atoms allows the direct measurement of the surface distance if it is larger than the imaging resolution. By slightly inclining the imaging beam so that it is reflected from the chip surface, both the atom cloud and its mirror image become visible. This mechanism is illustrated in Figure 5.2.

However, the presence of the chip surface also leads to optical effects hindering the absorption imaging. The inclination of the imaging beam results in a standing wave type interference pattern at the atom plane. In addition, Fresnel diffraction from the sharp chip edge modifies the intensity profile. In the dark fringes of this pattern the absorption signals vanish, because the light level is too low. Hence for certain distances  $h$  no observation of the atom cloud is possible. This is not problematic, since a slight rotation of the imaging beam results in a shift of the interference pattern so that formerly dark regions become bright and vice versa. At the imaging plane (the CCD chip), the beam that is reflected before the absorption and that reflected after the absorption interfere again.

We use a numerical simulation of wave propagation that takes into account these effects as well as specific properties of the imaging lenses to calibrate the exact imaging beam inclination angle  $\alpha$ . Once  $\alpha$  is known, the measured density profiles can be compared to numerical wave propagation simulations that are calculated for an absorber positioned at varying  $h$ . An example of such a numerical determination of the surface height  $h$  is shown in Figure 5.3. The result of this procedure can be used to determine the bias field strength  $B_{bias}$ .

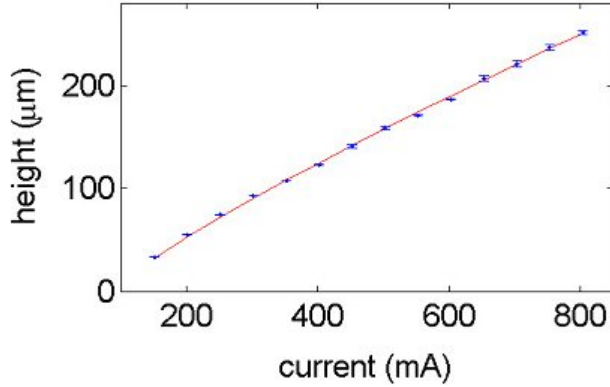


**Figure 5.4:** Bias field calibration using the surface heights obtained by the reflection imaging technique. The surface height predicted by a potential model is fitted to the experimental data with  $B_{bias}$  as fit parameter. It can be seen that the model accurately reproduces the height dependence on the wire current.

### 5.2.2 Bias field strength determination

The surface distance obtained from the reflection images allows a calculation of the bias field strength. For this, the surface distance is measured as a function of the wire current  $I$  for distances at which two clearly separated images are visible ( $h = 20 - 400\mu\text{m}$ ).  $B_{bias}$  is then obtained by entering these values into a model potential of the wire trap, which in turn allows to infer  $h$  for small atom-surface distances where a direct measurement is not possible.

To enhance the accuracy of the bias field determination the wire models used to calculate the potentials are refined. The simple trap models introduced in the last chapter do not describe the potential shape accurately enough for the small  $h$  we achieve in these experiments. The more complex models used here include the finite length of the central wire and field contributions from the leads that connect the Z-shaped wire to the contact pads on the chip edge.

An example of such a bias field calibration is shown in Figure 5.4. The accurate reproduction of the surface height dependence on the current  $I$  by the potential models can be seen. A detailed account of this calibration procedure and the model calculations will be given in [54].

### 5.2.3 Temperature measurement from in situ images

For small surface distances ( $h < 5\mu\text{m}$ ) the temperature determination from time-of-flight (TOF) images can also become difficult. The high compression and lifetime limiting surface effects reduce the number of atoms remaining in the trap when it is brought this close to the surface, so that the density of the expanding cloud in the TOF images becomes too small to yield reliable fitting results.

In that case we determine the temperature directly from the cloud extension in the in situ images. For this a calculated density distribution is fitted to the measured longitudinal density profile with the atom temperature  $T$  as fit parameter. The theoretical density distribution in the trap is obtained by assuming the (thermal) atoms follow the Boltzmann distribution  $n \sim \exp(-U/kT)$  in the



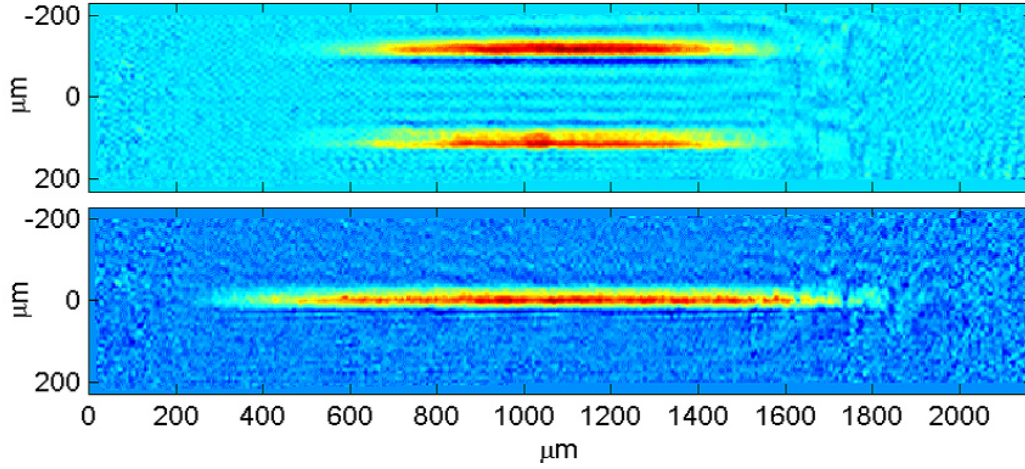


**Figure 5.5:** Absorption images of thermal atoms near the chip surface (100 $\mu\text{m}$ -trap in this example). **Top:** At a surface distance of  $h = 100\mu\text{m}$  two distinct images of the atom cloud are visible. **Bottom:** Even for a surface distance of  $h = 1\mu\text{m}$  the density is homogeneous throughout the trap. The cloud is elongated compared to the distant cloud because of the reduced longitudinal confinement in traps close to the surface. The atom temperature in these experiments was calculated directly from the in situ images to be  $T = 2\mu\text{K}$ . The fluctuations of the absorption signal on the right end of the cloud stem from bonding wires obstructing the imaging light rather than from atomic density modulations.

model potential  $U$ .

This method was compared with the conventional TOF method for traps with sufficiently high atom numbers at various temperatures. The agreement between both methods was good in all cases, so that we conclude the in situ method is valid. As a further consistency check of the potential models, we have compared the calculated value for  $T_C$  with the experimentally observable onset of condensation, and again found them to be in good agreement.

### 5.3 Experiments with thermal atoms

In order to characterize the disorder potentials present in our experiment we have brought both cold thermal atoms and BECs close to the chip surface. This was done in the 100 $\mu\text{m}$ -wire trap (Section 4.4) as well as the 10 $\mu\text{m}$ -wire trap (Section 4.5).

In contrast to the other experiments (Section 5.1), for thermal atoms we observe no fragmentation effects at all down to a surface distance of  $h = 1\mu\text{m}$  (Figure 5.5) in either of the two traps.

To detect the presence of disorder potentials, a density profile calculated from the potential model as described in the last section is subtracted from the observed profile. Any remaining fluctuations would indicate the presence of unexpected

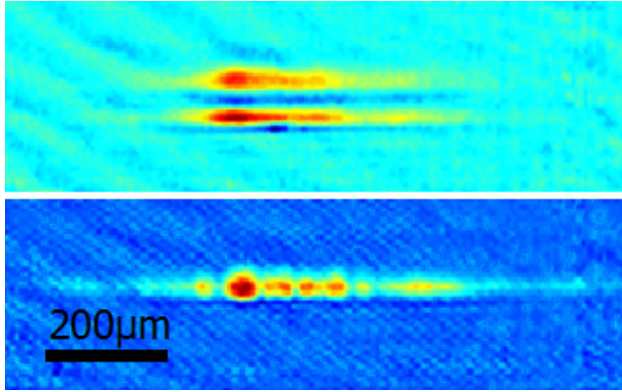


**Figure 5.6:** In situ images of BECs near the surface of the 100 $\mu$ m-wire. **Top:** Even a BEC remains essentially un-fragmented at a distance of 20 $\mu$ m from the wire. **Bottom:** For close distances ( $h < 5\mu$ m) the fragmentation becomes clearly visible.

potential modulations. In the case of thermal atoms we find a flat zero line with a residual experimental noise for both traps and all surface heights. The root mean square of this noise can be considered as measure of the detection sensitivity.

At the closest approach of  $h = 1\mu$ m above the 10 $\mu$ m-wire, where disorder potentials caused by the wire edges are expected to play a larger role than above the 100 $\mu$ m-wire, and for an atom temperature of  $T = 1.7\mu$ K we measure a rms-noise of the potential of  $U/k_B < 200$ nK. This yields a variation of the longitudinal field component along the trap of  $\Delta B/B < 3 \times 10^{-4}$  in units of the trapping field  $B$ . For the 100 $\mu$ m-wire we find similar numbers.

Our upper bound for  $\Delta B/B$  is significantly smaller than the values observed in other experiments. Considering the theoretically predicted and experimentally confirmed height scaling of the disorder effects, and taking into account that our upper bound is valid for  $h = 1\mu$ m compared to  $h \sim 30\mu$ m in other experiments, we can conclude that the disorder potentials in our experiment are at least two orders of magnitude smaller than in other cases. This is most likely due to the fabrication process of the atom chips used in the different experiments. Our atom chip is the only one fabricated with lithography techniques, all other groups use the wet-chemical technique of electro-plating (see Section 2.3.1). Our experimental results confirm that the lithographic fabrication process allows the production of significantly smoother structures, which was already observed by the direct microscopic examination of the chip structures (Figure 2.6).

## 5.4 Experiments with BEC

Ensembles of Bose-condensed atoms are more sensitive to potential roughness than thermal atoms. Hence, we use BECs to probe our potentials more thoroughly for disorder effects. In this case, we observe fragmentation of the atom cloud above both wires that were examined for  $h \leq 20\mu$ m. An example of this effect is shown in Figure 5.6. For small surface distances ( $h < 5\mu$ m) a clear fragmentation into distinct potential wells can be seen.

In the Thomas-Fermi approximation (Section 4.1.3), the condensate density is

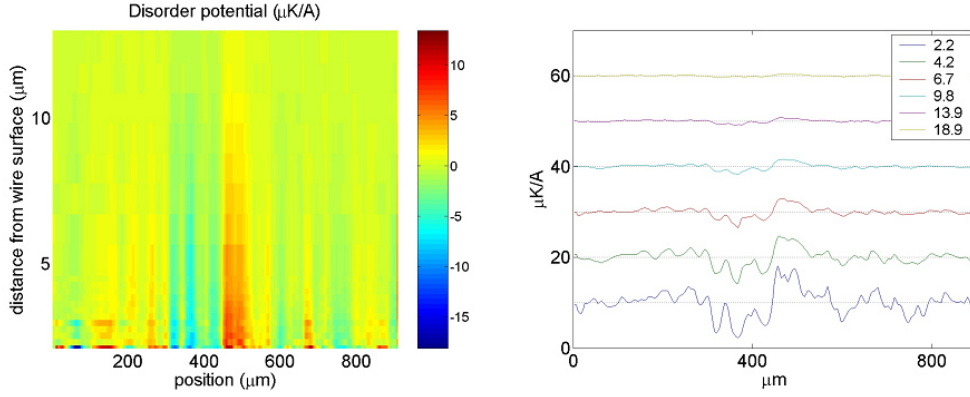


**Figure 5.7:** Disorder potential profiles for a height scan above the  $10\mu\text{m}$ -wire. For comparison with previously published data, the units are given in  $\mu\text{K}/\text{A}$  and not in the universal  $\Delta B/B$ . **Left:** False color image of the disorder potential as a function of position along the wire and height above the wire center. **Right:** Longitudinal profiles of the disorder potential for selected  $h$  (given in  $\mu\text{m}$  in the legend). Each curve has been shifted by  $10\mu\text{K}/\text{A}$ , the dotted lines represent the respective zero potential level.

given by the difference of the (global) chemical potential  $\mu$  and the external potential  $U$ . It is important to note that in our case this approximation is only valid in the longitudinal trap direction. For the transverse directions the single particle ground state energy far exceeds  $\mu$  for all values of  $h$  that we consider. The transverse extension of the cloud is thus solely determined by the transverse single particle ground state size. We obtain  $\mu$  from the total atom number  $N$ , the longitudinal density profile and the (calculated) transverse ground state sizes.  $N$  is derived directly from the in situ absorption images (calibrated with numbers obtained from TOF images). After the subtraction of the calculated density profile and the conversion from density distribution to potential, we again obtain the disorder potential.

A result of this calculation procedure is shown in Figure 5.7. The increase of the disorder potentials for smaller surface distances and the resulting fragmentation can be seen. The observed disorder potentials are stable both in time and position. We have confirmed this by changing the longitudinal position of the trap above the  $10\mu\text{m}$ -wire (this is possible because of the different wires providing the end caps for this trap). Also, the gradual damping of the disorder potentials with growing surface distance is observed as expected.

The spectral composition of the measured disorder potentials is shown in Figure 5.8. As expected, high frequency components are relevant only for small  $h$  and drop off more quickly with  $h$  as the larger scale (small  $k$ ) variations. Also shown is the scaling of the root mean square disorder potential strength with  $h$ . A power law fit yields  $\Delta B/B \propto h^{-1.2}$ , which is close to the predicted  $\Delta B/B \propto h^{-3/2}$ . An

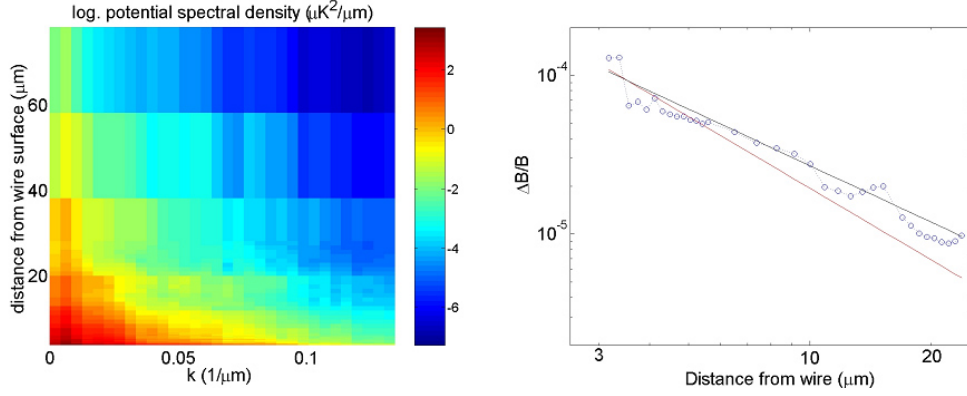


**Figure 5.8:** **Left:** Spectral composition of the disorder potentials as a function of the surface distance  $h$ . For increasing  $h$  the high frequency components are damped more quickly than the slow ones, as predicted in [123]. **Right:** Integrated (rms) disorder potential strength as a function of  $h$  in units  $\Delta B/B$ . A power law fit to the data (black line) yields an exponent (-1.2), which is close to the predicted (-3/2) (red line).

extrapolation to the heights where other experiments observed fragmentation<sup>1</sup> ( $h \sim 50\mu m$ ) shows an approximately 100-fold reduction of the disorder potentials above lithographically fabricated wires compared to electro-plated wires. For  $h < W$  we observe deviations from the predictions made in [123]. In this regime the scaling with  $h$  of the disorder potentials should level off, because the distance to the wire edges does not change significantly. We should be able to observe this in particular above the  $100\mu m$ -wire, as the condition  $h \ll W$  is definitely fulfilled there. In Figure 5.9 the longitudinal absorption profiles for various trap heights above this wire are shown. For the span of this height scan neither the transverse trapping frequencies nor the number of atoms vary significantly, so that the density profile is a direct measure of the trapping potential. Instead of a levelling-off we observe a permanent increase of the disorder potentials even for very small distances. This indicates an effect that cannot be explained exclusively by the wire edge roughness. Instead, bulk conductivity fluctuations must be responsible (at least partially) for the disorder potentials at these distances. A future model describing the role of wire imperfections on the resulting trapping potential must include this effect.

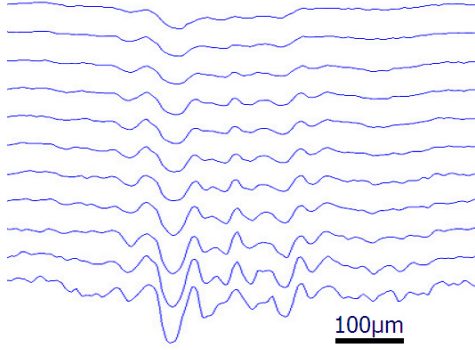


**Figure 5.9:** Longitudinal absorption profiles for equidistant heights between  $15\mu\text{m}$  and  $3\mu\text{m}$  (top to bottom) above the  $100\mu\text{m}$ -wire. Although  $h \ll W$  is fulfilled, the disorder potential strength increases. This is an indication of a bulk effect.

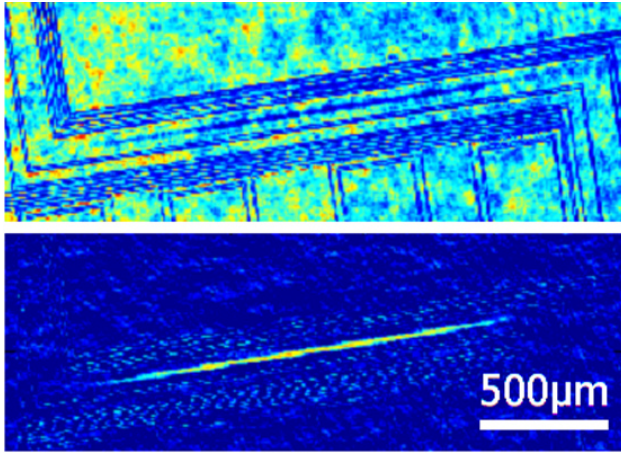


**Figure 5.10:** The position of an atom cloud above the  $100\mu\text{m}$  wire can be shifted by rotating the bias field. **Top:** The vertical imaging allows a direct determination of the atom cloud position in relation to the wire, because both the atoms and the chip structure are visible in the images. **Bottom:** In processed absorption pictures the visibility of the chip structure is reduced while the signal of the atom cloud is clearly visible.

## 5.5 BEC as ultra-sensitive magnetic surface microscope

The experiments described in the last section showed that BECs are sensitive to extremely small potential variations. This may turn out to be a useful tool for studying the magnetic properties of (current-carrying) surfaces. Moving the BEC over the surface allows to reconstruct a three-dimensional map of the magnetic field produced by the surface.

The sensitivity of this technique is only limited by the chemical potential  $\mu$  of the BEC. In our experimental situation,  $\mu$  can be as small as  $k_B \times 100\text{nK}$  at a  $h \approx 1\mu\text{m}$  above the  $100\mu\text{m}$ -wire which corresponds to a magnetic field difference of  $\Delta B_\mu \approx 1\text{mG}$ . Density fluctuations caused by field variations of about a tenth of  $\Delta B_\mu$  are still detectable, which results in a resolution for relative magnetic field fluctuations of  $\Delta B/B \sim 10^{-5}$ . The further reduction of the chemical potential is mainly restricted by the tight transverse confinement (large  $\omega_t$ ) in our traps. Above broader current ‘sheets’ less compressed traps can be realized to further

<sup>1</sup>A direct comparison is not possible, because we do not measure any fragmentation effects at these heights.



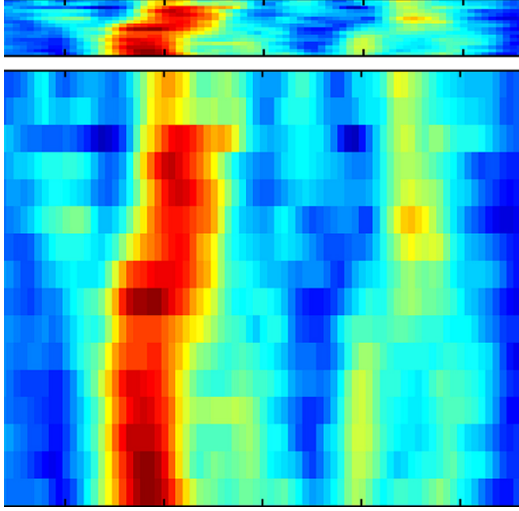


**Figure 5.11:** Potential reconstructed from a transverse BEC scan of the  $100\mu\text{m}$ -wire surface at a height of  $h = 3\mu\text{m}$ . The scanned area has a size of  $30 \times 250\mu\text{m}^2$ . Red false color shades correspond to potential wells, blue shades to barriers. **Top:** Image to scale. **Bottom:** The same image with exaggerated transverse direction to increase the visibility of the potential modulations.

reduce  $\mu$  and thus to improve the achieved resolution of magnetic field variations. Translated to current densities, the sensitivity we already achieve is sufficient to resolve angular deviations of the current flow of  $< 10^{-2}\text{mrad}$ , which corresponds to a current path that differs from the nominal path by a single micron over a length of  $10\text{cm}$ .

The spatial resolution of this technique is mainly limited by the optical imaging. The diffraction limit of our current imaging system (Section 3.1.5) is  $\sim 3\mu\text{m}$ . This could be improved if appropriate optics with smaller working distances were used, but this is momentarily prevented by the size of our vacuum chamber. A different approach to enhance the spatial resolution may be to analyze interference patterns that arise from optically unresolved BEC density modulations during time-of-flight expansion when the condensate is released from the trap.

Another limitation to the spatial resolution are lifetime-limiting surface effects. The BEC must approach the investigated surface to a distance of the order of the spatial resolution. For  $h < 1\mu\text{m}$ , attractive surface potentials start to dominate, which prevent an even closer approach to the surface [84].

We have tested this microscopy method by scanning the surface of the  $100\mu\text{m}$ -wire. The position of the trap center can be shifted in the horizontal direction perpendicular to the current flow by tilting the bias field, which is done by adding a vertical field component with the u-d coils. To produce a horizontal movement at constant surface distance  $h$ , the total bias field strength has to be adjusted carefully. This becomes especially important near the wire edges. Alternatively a scan along a curve of varying surface height can be calibrated by the known scaling behavior of the frequency components of the disorder potential.

An example of a magnetic potential reconstructed from such a scan is shown in Figure 5.11. To obtain the data for this result a BEC was moved over the  $100\mu\text{m}$ -wire at a surface distance of  $h = 3\mu\text{m}$ . We observe a structuring of the potential over the whole wire, with no apparent difference between the edge and center

regions. This again is an indication that these field fluctuations are caused by a bulk effect and not solely by wire edge roughness. The exact knowledge of the disorder potentials near our chip wires makes it possible to think about using the observed potential irregularities in a controlled way. For example, the potential shown in Figure 5.11 shows a double-well structure in the longitudinal direction, in which a BEC could be split for free expansion interference experiments.

These first experimental results show the feasibility of a ‘BEC microscopy’ technique. The combination of good spatial resolution and ultra-high relative magnetic resolution promises to make this a useful tool for precision measurements of conductor or magnetic material properties. Existing methods either have the disadvantage of low  $\Delta B/B$  resolution (magnetic force microscope) or of low spatial resolution (high precision magnetometers). An example application one can think of is the quality control of semiconductor materials where local dopant concentrations could be precisely measured.

Also of great interest would be the reconstruction of the local current density in the wire from the measured potential structure. The experimental data contains only information about the modulus of the magnetic field, which does not allow an unique mapping to a current density vector field. A model for the current flow in the wire requires additional information obtained by detailed (conventional) microscopic analysis of the wire structures and certain assumptions about the conductivity properties of the wire material. We are currently in the process of developing a consistent model that incorporates all our experimental results so far and detailed microscopic analysis of lithographically produced test chips.





## 6 Atom chip interferometer

Interference of particles with finite size and mass is a field of great interest, both for fundamental studies and for practical applications. It is proof for the quantum-mechanical nature of matter and allows the examination of fundamental decoherence mechanisms [22]. The extension of interference experiments to molecules of growing size and complexity tests the boundary between classic and quantum physics [4]. On the other hand, matter wave interferometers can be used in precision metrology and as highly sensitive acceleration and rotation sensors [79, 102]. A thorough treatment of atom interferometry can be found for example in [11].

Integration of matter wave interferometers on atom chips allows the miniaturization of the experimental setup, which may lead to portable devices for applications. Also the combination of the interferometer with other chip elements opens the possibility of using interference effects to study more complex phenomena [98, 18].

In the context of current atom chip experiments the observation of matter wave interference is intended to demonstrate the general feasibility of coherent atom manipulation with chip-based potentials. Coherence-preserving guiding, splitting and recombining of an atom cloud are important steps towards the realization of complex atom chip operations. Also, an interferometer can be used for sensitive studies of surface noise effects, which will affect the observed interference patterns. Especially the effect of phase noise can only be measured in interference experiments.

In the first part of this chapter (section 6.1), the general concept of a guided matter wave interferometer consisting of two identical beam splitters is introduced. In section 6.2 the implementation of such an interferometer on our atom chip is described. First experiments carried out to test this interferometer are discussed in section 6.3.

### 6.1 Guided matter wave interferometer

A theoretical model for an interferometer for guided atoms consisting of two Y-shaped beam splitters is given in [3]. To form the interferometer, two identical beam splitters are joined back to back as shown in Figure 6.1(a). The model treats the wave guide as two-dimensional with a harmonic transverse confinement. Although such 2-d guides have been realized [43, 64, 116], the magnetic

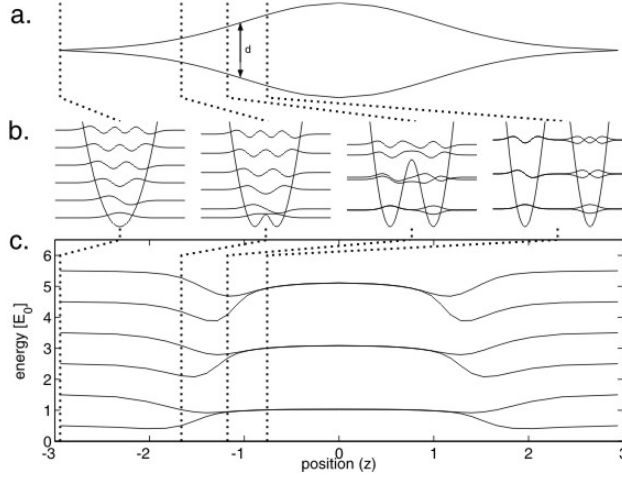


**Figure 6.1:** Guided matter wave interferometer: (a) The interferometer is formed by combining two identical Y-beam splitters. (b) Transverse eigenfunctions of the guiding potential at the indicated positions along the interferometer. (c) Energy eigenvalues for the lowest transverse modes along the interferometer potential. It can be seen that pairs of transverse eigenstates form disjunct interferometers.

potential we employ is three-dimensional. This significantly complicates the level structure of the transverse modes of the guide and it remains to be investigated how this changes the interferometer behavior. Still, the 2-d model is adequate to demonstrate the general principle of our interferometer.

The symmetry of the guiding potential guarantees coherent 50/50 splitting of incoming matter wave packets, independent of the transverse mode [20]. This was confirmed by numerical simulation of the wave-packet propagation for the lowest 35 modes. In figure 6.1(c) the eigenenergies of the lowest transverse modes along the interferometer are shown. It can be seen that there are many disjunct interferometers in Fock space. Each of them has two input modes  $|2n\rangle$  and  $|2n+1\rangle$ , where  $n$  is the energy quantum number of the transverse harmonic oscillation. In the splitting region, the waves propagate as a superposition of  $|n\rangle_l$  and  $|n\rangle_r$ , in the left and right arm, respectively. For an ideal splitting potential all interferometers are identical (This especially requires  $\omega_{split} = 2\omega_{comb}$ , i.e. that the transverse frequency in the splitting region is twice as large as in the input guide).

After the recombination the wave packet will again be in a superposition of the  $|2n\rangle$  and  $|2n+1\rangle$  modes. This superposition is altered by any phase difference between  $|n\rangle_l$  and  $|n\rangle_r$  acquired during the spatial separation of the wave function. Such a phase shift between the arms can be introduced either by a path length of the two arms or by adjusting the potentials to be slightly different in the two arms.

A particle in an outgoing mode different from its incoming mode has experienced a transverse (de)-excitation which translates into a changed longitudinal propagation velocity ( $\Delta v = \pm\omega_t/k$ , where  $\hbar k$  is the particle momentum and  $\omega_t/2\pi$  is the transverse trapping frequency), since transverse oscillation energy is transferred to longitudinal kinetic energy, and vice versa. This in turn leads to a longitudinal interference pattern observable as an atomic density modulation in the outgoing atom cloud. The equity of all interferometers guarantees the vis-

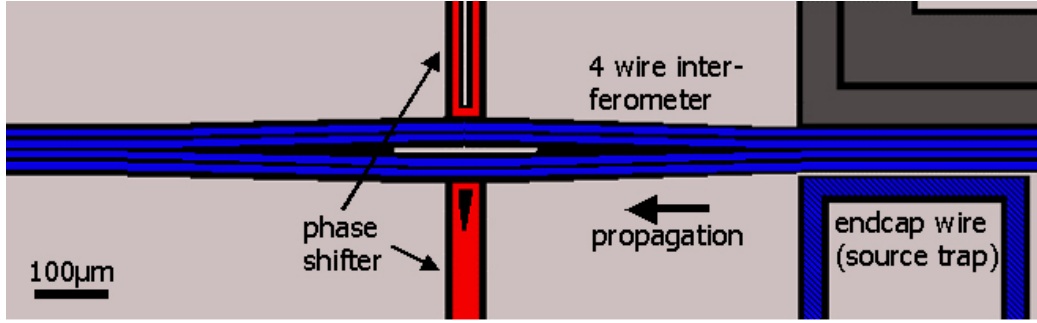


**Figure 6.2:** Implementation of the guided matter wave interferometer on the atom chip. The consecutive widening and narrowing of a four-wire guide creates the two combined Y-beam splitters (blue wires). The red wires can be used as electrostatic and/or magnetic phase shifters. The shown U-wire (hatched blue) provides the endcap of the initial trap from which the atoms are released into the interferometer (similar to the  $10\mu\text{m}$ -trap discussed in section 4.5).

ibility of these fringes even for an incoherent sum over many input momentum states (wave packets of thermal atoms) for a sufficiently narrow source.

It is important to note that to obtain this result a number of idealizations were made in the model. The reduction to two dimensions and the assumed exact symmetry between the two arms have already been mentioned. Further idealizations are for example the assumption of a perfectly harmonic transverse potential, a pointlike source of the wave packet, and a perfect transition from the guide potential to the split double well potential with exactly  $\omega_{split} = 2\omega_{comb}$ . All of these requirements cannot be strictly fulfilled in an experimental realization. The deviations from the theoretical model and their implications are discussed in detail for our implementation of this interferometer scheme in [75] and [44]. What effect these deviations will have on the observed fringe patterns remains to be seen, but one has to expect a reduction of the fringe contrast at least.

## 6.2 Implementation on our chip

An implementation based on magnetic potentials of the interferometer proposal outlined above is realized on our atom chip. Alternatively optical potentials have been used to create such guided matter wave interferometers [68, 33].

The interferometer on our atom chip is formed by the combination of two four-wire beam splitters of the type introduced in Section 2.2.4. The wire layout on the chip is shown in Figure 6.2.

As has been discussed in Section 2.2.4 the guiding potential is formed by combining the field created by the four wires with a vertical bias field. For constant bias field and current in the wires the positions of the potential minima depend only on the wire separation. The bias field is chosen so that in the area outside

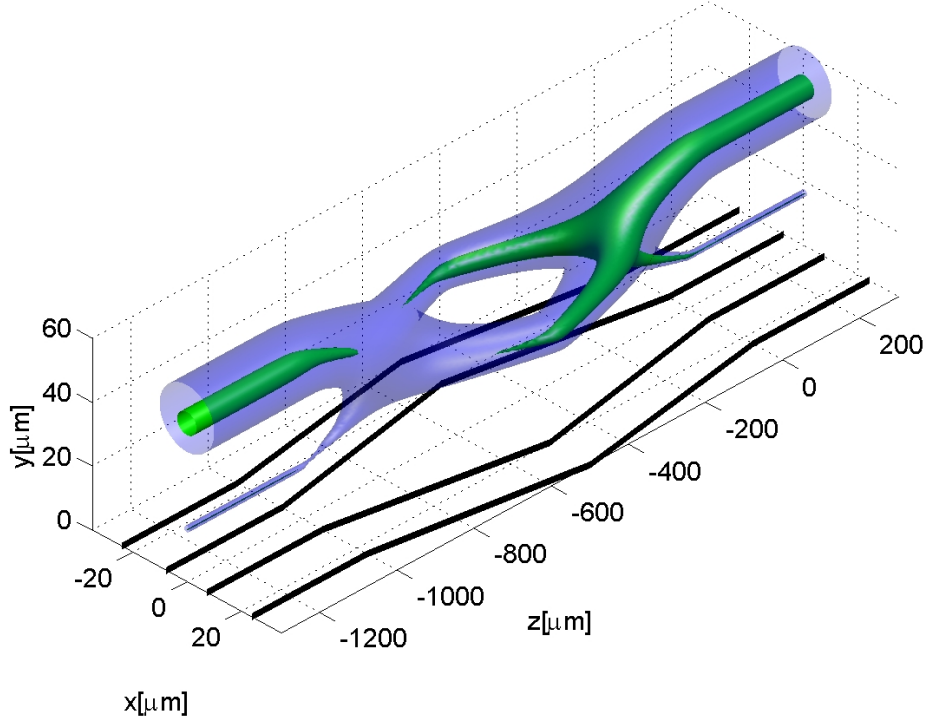


**Figure 6.3:** Interferometer potential realized with two four-wire beam splitters. The black lines indicate the wires on the chip surface, the contour plots show equipotential surfaces for  $E/K_B = 100\mu\text{K}$  (blue) and  $E/K_B = 20\mu\text{K}$ . In the regions before and after the interferometer two asymmetric vertically separated minima exist, while in the center there are two symmetric horizontally separated minima. The points where the minima orientation changes are the beam splitters.

The variation of the longitudinal field component along the guide caused by the splitting of the wires leads to the formation of a barrier that prevents cold atoms from traversing the interferometer (closed green equipotential surface). The parameters used in this calculation were  $I = 0.4\text{A}$ ,  $B_{\perp} = 8\text{G}$ , and  $B_{\parallel} = 1\text{G}$ .

of the interferometer region the case of two vertically separated minima is given, of which the lower one with its strong confinement is practically inaccessible. In the central region the increased distance between the two wire pairs changes the potential to the case of two horizontally separated minima. Splitting occurs at the points where the vertical splitting changes to horizontal splitting (Figure 6.3). The splitting angle and the wire separation are chosen so that the condition  $\omega_{split} = 2\omega_{comb}$  can be realized for experimentally realistic parameters.

Additionally an external Ioffe-field parallel to the four wires is used to avoid field zeros along the guide. While this field does not destroy the splitting symmetry of each beam splitter, it causes a difference between the two splitters. In the splitting region the orientation of the wires results in contributions of the wire

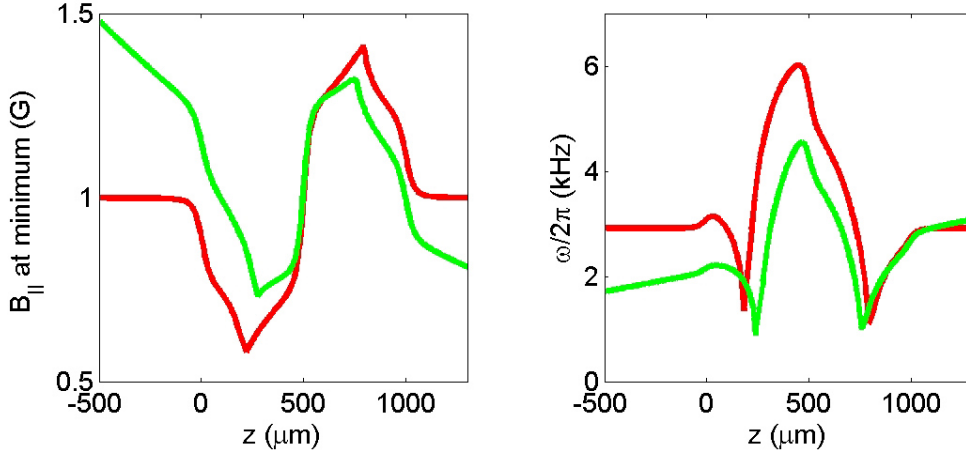


**Figure 6.4:** **Left:** Field strength of the longitudinal field component  $B_{\parallel}$  at the potential minimum plotted as a function of location along the interferometer guide with (green curve) and without (red curve) additional pushing field. ( $z = 0$  marks the position of the first beam splitter). The red curve shows a potential barrier, which cannot be overcome by atoms with kinetic energy below this barrier height. The green curve still shows the modulation of the field caused by the wire guide, but the extra field ‘tilts’ the potential so that all atoms have sufficient energy to pass the barrier. **Right:** Transverse trap frequency along the guide. Without the extra field (red curve) the frequency at the point of maximal separation is approximately twice as large as in the input guide. This behavior is altered by the extra field (green curve) which slightly changes the compression inhomogeneously. The parameters used for these calculations were  $I_{wire} = 400\text{mA}$ ,  $B_v = 8\text{G}$  (13G), and  $B_{\parallel} = 1\text{G}$  (0.1G) in the case of  $I_{push} = 0\text{A}$  (20A).

fields to the longitudinal field components, which are opposite for the two splitters because of their head to head arrangement. Together with the external field this leads to a potential barrier near one beam splitter and a potential trough near the other, as can be seen in the green equipotential surface in Figure 6.3. The height of the barrier depends on the wire current and the (fixed) splitting angle  $\alpha$ , not on the external homogeneous field. In our case ( $\alpha \approx 50\text{mrad}$ ), it is approximately  $1\text{G/A}$  current through each of the wires. Typical currents we used in the experiment were  $\sim 400\text{mA}$ , which means the potential barrier has a height of  $E/k_B = 27\mu\text{K}$ .

This problem of cold atoms being unable to travel through the interferometer can be solved by applying an *inhomogeneous* additional longitudinal field, which ‘pushes’ the atoms through the guide. In our setup, such a field can be created by the Cu-structures underneath the chip (Section 3.1.4). We used a straight wire that runs perpendicular to the four-wire guide. This wire is located  $6\text{mm}$  from the interferometer in the longitudinal direction and  $1.2\text{mm}$  below the chip surface. Because of this comparably large distance, currents of  $> 20\text{A}$  are required to produce a sufficient pushing effect, as is illustrated in Figure 6.4(left). The inhomogeneous longitudinal field produced by this wire effectively ‘tilts’ the Ioffe

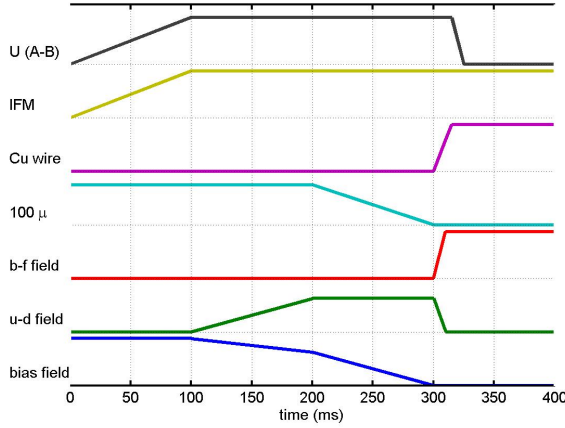


**Figure 6.5:** Schematic of a typical experimental control sequence for the interferometer pushing experiments. The lines show the modification of the applied currents and external fields as functions of time (not to scale). Both the loading (0-300ms) and the guiding phase (300-400ms) of the interferometer are shown. See text for the description of the experiment.

field of the wire guide, to give the atoms in the guide additional energy to pass the interferometer.

The additional wire also adds an inhomogeneous component to the vertical field direction. This alters the transverse shape of the potential along the whole guide, as is shown in Figure 6.4(right). The symmetry of the input and output guides is slightly affected by this modification, but it should be uncritical for the general functionality of the interferometer.

## 6.3 Present experimental status

In the course of this thesis first experiments were carried out to test the interferometer described above. The goal of these initial tests was to verify the general functionality of the potential and to establish an experimental procedure for guiding atoms through the interferometer.

### 6.3.1 Potential testing with thermal atoms

The first loading and testing of the interferometer was carried out with thermal atoms at relatively high temperature ( $T \approx 20\mu\text{K}$ ). This guarantees a large number of atoms ( $3 \times 10^6$ ) loaded into the guide, which makes the observation of the atoms moving in the guide easier. Also atoms at this temperature are less sensitive to potential changes than colder atoms.

The first step of the interferometer experiment is the loading of the four-wire guide from the  $100\mu\text{m}$ -trap. The loading procedure is illustrated in Figure 6.5. It follows the standard approach of first ramping up the destination trap without changing the source trap. Within the first 100ms the current in the four-wire guide (IFM) is ramped up to 400mA in each wire. To initially close off the guide in the direction of the interferometer the chip U-wire (A-B) closest to the splitting region is used. This forms an end cap to the guide potential similar to the

10 $\mu$ m-trap (Section 4.5). The U-wire is ramped up to 300mA together with the IFM. The potential barrier in the other direction along the guide is given by the small horizontal connections between the four wires.

During the transfer the bias field direction has to change from vertical to horizontal. This is done in a two-stage process. First the bias field is ramped down from 7G to 5G within 100ms while at the same time the u-d field is ramped from zero to 5G. The resulting homogeneous field is orientated under an angle of 45° with respect to the chip surface. This rotates the center of the 100 $\mu$ m-trap to a position above the IFM wires. In a second 100ms ramp the bias field is turned off, as is the current in the 100 $\mu$ m-wire. The atoms are now trapped in the guide potential.

At this point the U-wire current is ramped down within 10ms to release the atoms into the guide. Initial experiments without an additional pushing field confirmed the calculated strength of the potential barrier created by the splitting wires. The atoms experience a small acceleration due to the end cap of the four wires and start to move along the guide, but most atoms are stopped at the first beam splitter. The percentage of atoms passing through the IFM agreed well with our calculations of a potential barrier of  $U/k_B \approx 27\mu\text{K}$ . This was confirmed by experiments with varied temperature of the guided atoms.

The pushing field is applied by sending a current through one of the Cu-wires underneath the chip. This current is ramped up to 30A in 10ms before the chip-U is turned off. To compensate the effect of this additional field on the trap bottom the b-f field is also increased to 1G at the same time. We found that the vertical field created by this wire for a current of 30A is sufficient to act as the bias field of the IFM guide. Hence we ramp down the u-d field completely when we the Cu-wire is ramped up. To increase the pushing effect, the Cu-wire current is subsequently increased to 45A (within 5ms). It is interesting to note that at this point the complex IFM potential is formed completely (with the exception of a small external Ioffe field) by wire structures.

The result of such a pushing experiment is shown in Figure 6.6. A time sequence of absorption images taken with the vertical camera shows the propagation of the atoms along the IFM ( $t = 0$  marks the time when all ramps are completed, corresponding to  $t = 315\text{ms}$  in Figure 6.5, accordingly the moment of release from the initial trap is  $t = -5\text{ms}$ ). It can be seen that all atoms are pushed out of the starting region by the pushing field. A fraction of atoms remains trapped at the IFM barrier though, probably those (cold) atoms that were closest to the IFM before release and consequently experienced the weakest acceleration by the pushing field. To completely overcome the barrier the strength of the push field has to be increased.

The figure also shows an image of the atoms in the IFM taken with the horizontal camera. The smaller surface distance of the guide in the splitting region can be seen. The (fixed) wire spacing determines the heights for which the condition  $\omega_{split} = 2\omega_{comb}$  is fulfilled, these are 45 $\mu\text{m}$  for the input/output guide and 32 $\mu\text{m}$



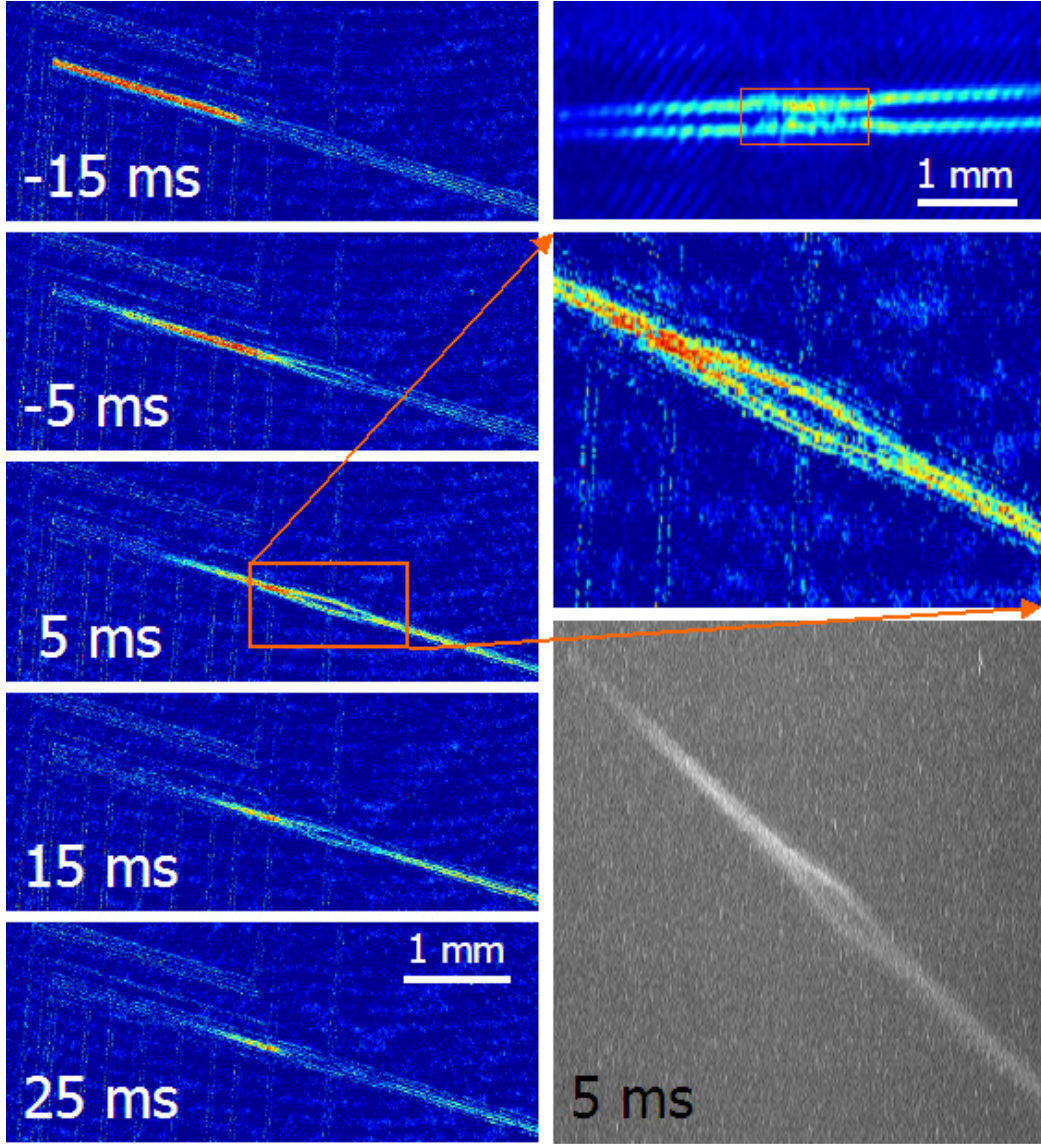


**Figure 6.6:** Thermal atoms ( $T \approx 20\mu\text{K}$ ) propagating through the interferometer. **Left:** Time sequence of absorption images taken with the vertical camera ( $t = 0$  marks the completion of the ramping up of the pushing field). **Top right:** Absorption image taken with the horizontal camera while most atoms are in the interferometer. Two images are visible because of the reflection from the chip surface, the two different arms cannot be seen in this image. The distance to the surface is slightly lower in the splitting region than in the output guide. The optical access is partly obstructed by bonding wires in the splitting region (orange box). **Center right:** Enlarged detail of the splitting region, showing the atoms in the two arms. **Bottom right:** Fluorescence image of atoms in the interferometer taken with the vertical camera. This technique allows the imaging of the atoms without the chip surface in the background. The direction of propagation is from left to right in all images.



for the splitting region. The vertical bias field and the wire current have to be tuned accordingly to realize these values. This fact may limit the experimental flexibility, both for applying a pushing field and for using the IFM for height scans to study surface influences. It is hoped that deviations from the correct compression ( $\omega$ ) ratio only smear out the interference pattern instead of destroying it. It should then be possible to account for such effects in the analysis of the observed atom density distribution.

In addition to the relatively large temperature of the atoms, the main reason why we did not expect to observe any type of interference pattern in these experiments was that the source trap was not (close to) pointlike, but had a longitudinal extension of over 2mm. Longitudinal compression is planned to be achieved by using an appropriate combination of the chip U-wires as described in [44]. A first test of this scheme, the ramping up of the outermost U-wire (F-E), lead to the unexpected splitting off of part of the atom cloud into a separate minimum created by the U-wire and the vertical field. This was due to the fact that the atom cloud extended beyond the position where the potential barrier created by the additional U-wire is situated. Colder atoms should be confined to a smaller area around the longitudinal center of the initial guide trap, so that the problem should not arise in that case. An alternative approach that we have studied recently [54] is to use an electric field to create a longitudinally strongly confining potential dimple in the guide potential into which the atoms are collected.

### 6.3.2 BEC in a guide

While the experiments with thermal atoms described above demonstrated the general feasibility of the interferometer potential, the number of populated transverse states has to be reduced to observe the expected interference pattern, i.e. the atoms have to be cooled before they are released into the interferometer.

When a BEC is used only the transverse ground state is occupied and a single input mode is realized. In that case, the observation of a fringe pattern does not depend on the exact overlap of multiple interferometers. Hence the condition  $\omega_{split} = 2\omega_{comb}$  need not be fulfilled, which on first sight simplifies the situation. Other than for thermal atoms, in a BEC the atom-atom interaction can play an important role though. Atoms in the guide cannot be treated as single particles anymore; instead modifications to the splitting process due to many-particle effects are to be expected [92]. A theoretical description of interacting Bose-gases in guided matter wave interferometers is currently being developed [96].

In addition to such fundamental aspects, the guiding of a BEC (and also of cold thermal atoms) poses an experimental challenge. To avoid the destruction of the BEC all potential barriers have to be smaller than the chemical potential  $\mu$  of the condensate. Also any change of the transverse trapping frequency has to be considered, because even a small raising of the guide ground level can be an effective potential barrier for a BEC.

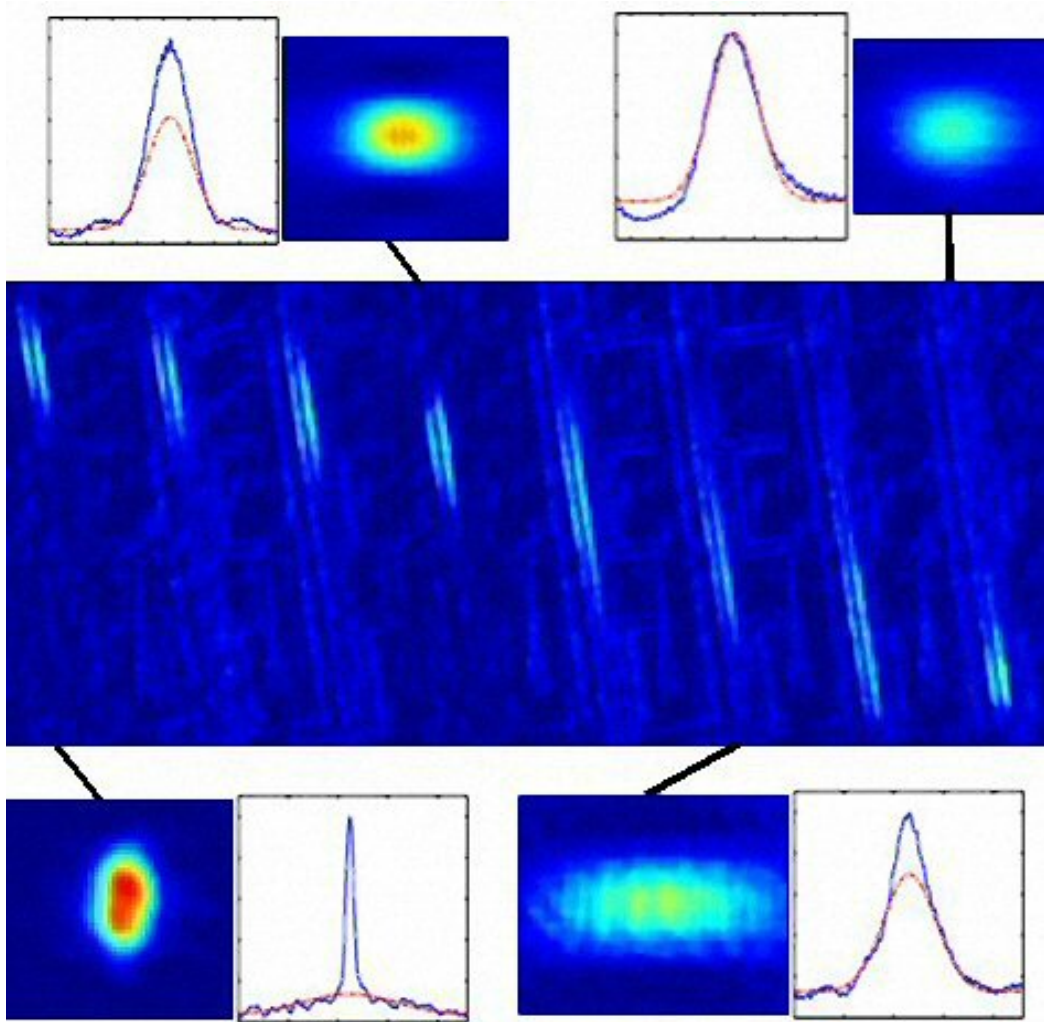


**Figure 6.7:** Time sequence of a BEC released from a trap into a guide. The center row shows a sequence of images (time step 10ms) taken with the vertical camera. The movement of the BEC (and its reflection) along the guide can be seen. The top and bottom row show corresponding TOF (10ms) images taken with the horizontal camera. The gradual transition from a pure condensate to a thermal cloud during the movement can be seen in the 1D density plots: The red curves are the Gaussian part of a bimodal fit, which give an indication of the size of the thermal fraction of the cloud. The second (bottom right) and third (top left) TOF image show fringe pattern similar to those observed in Figure 4.11.

We have started to test the evolution of a BEC in a guide based on chip-wires. To simplify the situation, these experiments were not carried out in the four-wire guide, but instead in the  $10\mu\text{m}$ -trap (Section 4.5). After the production of a BEC in this trap, the current in the U-shaped wire is ramped to zero to remove the potential barrier on one side of the trap. The atoms are pushed along the guide by a longitudinal field gradient produced by the outer lead of the  $10\mu\text{m}$ -wire.

The movement of the BEC in the guide is shown in Figure 6.7. The atom cloud can be seen to move along the wire guide, also an elongation of the cloud is observed. After 70ms of expansion the atom cloud reaches the splitting region of the interferometer wires, where the small longitudinal field produced by the wire bent provides a potential barrier that is enough to stop the movement of the atoms. Here the cloud is compressed again.

The corresponding TOF images show the transition from BEC to thermal cloud during the transfer. The thermal fraction of the atom cloud continually grows, until at the end of the sequence only thermal atoms remain. The TOF images also show the elongation of the cloud during the transfer. Additionally indications of abnormal density fluctuations similar to those observed previously after the release of condensates from traps with large aspect ratios are visible (Figure 4.11). This again is a sign of a (quasi)-1D effect.

While this experiment was carried out to test the use of BEC in guided matter wave interferometers, the study of BEC transport in itself are of great interest. Experiments of this kind allow the controlled simulation of transport mechanisms in mesoscopic electronic systems [69]. The atom chip environment is especially well suited for this task, as the presence of a tunable (via the surface distance  $h$  of the guide) random potential roughness opens the possibility of studying a large variety of transport phenomena, for example Anderson localization effects [2].



## 7 Summary and outlook

In this thesis the first experiments carried out with a new  $^{87}\text{Rb}$  atom chip setup were described. The initial steps of the experiment were characterized and optimized (Chapter 3). These optimizations include a reduction of the MOT-loading time from over 50s to 22s, which almost doubles the number of experimental cycles in a fixed amount of time, and the improvement of the optical pumping process. Over the last year, various enhancements of the setup were implemented, for example additional coil pairs that allow a reversal of the homogeneous magnetic fields, the new vertical imaging system, a new self-built slave laser for the repumper laser system, and the coupling of the radio-frequency generator to the Cu-Z wire. The better understanding and the improved functionality of the initial experimental steps now allow us to create BECs in the Cu-Z trap within a few experimental cycles after starting the experiment.

As the start of the atom chip experiments, a loading scheme was devised to transfer atoms to chip-based potentials. This scheme was extensively tested and improved, resulting in a virtually loss-free transfer of atoms from the Cu-Z trap to the atom chip. Benchmark numbers are now  $2 \times 10^6$  transferred atoms at  $T \approx 10\mu\text{K}$ . The on-chip BEC creation laid the groundwork for further chip experiments. We now routinely produce chip-BECs with  $\sim 10^5$  atoms. The dependence of this number on the transfer temperature, the duration of the cooling phase, and the trap parameters was examined and an optimal procedure was developed (Chapter 4).

To examine the effect of wire irregularities on our atom chip, we have brought both BECs and thermal atoms close to the chip surface (Chapter 5). The total absence of any fragmentation effects in thermal clouds and the comparably small effects on BECs show a reduction of disorder potentials by two orders of magnitude in comparison to other experiments. This can be attributed to the greater precision of the lithographic production method used for our chips compared to the electroplating technique used by other groups. The ability to bring BECs to surfaces distances of  $\sim 1\mu\text{m}$  allows a probing of the current density distribution in the surface with a precision and spatial resolution that may be superior to existing methods, letting one think of a ‘BEC microscope’.

First steps were taken in the direction of atom interferometry with a guided matter wave interferometer (Chapter 6). We demonstrated the splitting and recombining of thermal atoms and examined the behavior of a BEC in a guide. Based on these results it is now possible to use the interferometer potential with considerably colder thermal atoms or even with BECs to observe the expected

interference pattern.

The results presented in this thesis open the way for a wide range of new experiments. The reliability of the BEC production process and the weakness of the observed fragmentation effects now allow us to consider advanced chip experiments. Here, a short overview of the current plans and possibilities for the short to mid term future is given.

- *Fragmentation:* The recent installation of new imaging optics has improved the magnification of the horizontal imaging system from 1.7 to 3.5. We now achieve a resolution of  $3.5\mu\text{m}$  per pixel, which is close to the diffraction limit  $3\mu\text{m}$ . This enables us to investigate the disorder potential effects on BECs with even more precision. We are currently in the process of mapping the potentials above different wires, with the goal of using this data to develop a consistent model of the current flow in the chip wires, that includes both edge and bulk effects.
- *Noise effects:* We have already studied the dependence of the trap lifetime on the surface distance in detail, the results will be presented in [54]. At the small surface distances ( $d < 1\mu\text{m}$ ) we can now achieve, new surface effects should start to play a role. For  $d < 3\mu\text{m}$  an attractive surface potential caused by Casimir-Polder forces [19] between the trapped atoms and the surface becomes strong enough to provide a loss channel towards the chip surface, which results in a drastic reduction of the trap lifetime. The ability to accurately vary the surface distance of trapped BECs should enable a precise study of this surface effect, for example allowing an observation of the transition between the Casimir-Polder and the van-der-Waals regime. A new surface effect that has been observed recently is the formation of a polarized layer of adsorbed Rb atoms on the surface [91]. This results in an attractive electric potential near the surface in addition to the Casimir-Polder potential. It remains to be seen if this will play a role for our atom chip and if we can differentiate between the different effects. Again, the sensitivity of BECs near surfaces may provide new insights into the process of atom adsorption.
- *Atom interference:* All necessary steps to use the guided matter wave interferometer with cold thermal atoms have been tested, the experiment can be carried out as soon as the surface disorder experiments are completed. Guiding a BEC through the interferometer will pose more difficulties, but also provides an interesting topic by itself. Here it will be possible to study transport mechanisms in a strongly correlated quantum system.
- *One dimensional BECs* The extreme aspect ratios that can be realized with atom chip traps make them ideally suited for studying one-dimensional

systems, as has been described in Section 4.5.3. We have observed effects in highly compressed traps that seem to be first indications of phase-fluctuations in elongated condensates (Figure 4.11), and the analysis of the surface experiments has clearly shown that we reach the 1D-Thomas-Fermi regime. This opens the way for comprehensive studies of 1D-BECs with our current atom chip. The precise tunability of the aspect ratio via the trap height especially gives access to the highly interesting (and hard to realize in conventional experiments) crossover between 3D and 1D regimes.

- *Tunnelling:* A first experiment towards the controlled manipulation of a quantum state on the atom chip would be the observation of atom tunnelling between different potential wells. In this case, the two localized states in the separated potential wells form a qubit. By controlling the timing of the tunnel interaction, the atom can be put into any desired superposition state (single qubit gate). We are planning to use the double well interferometer structure on our current chip (connections K, M, P, R, Q, L in Figure 2.7) for such an experiment. Another possibility is to use neighboring potential wells created by wire imperfections, like those shown in Figure 5.11.
- *Internal states:* A qubit can also be formed by two different internal levels of an atom. Different schemes for implementing QIP with such internal qubits exist. For example, a collisional two-qubit gate based on the combination of magnetic and electric fields is proposed in [119]. Here the fact is exploited that the coupling of an atom to an external magnetic field depends on the magnetic quantum number, while for an electric field atoms in all magnetic levels experience the same Stark shift. The principle viability of using electric fields for state-selective manipulation of atoms has been demonstrated in our group [75]. We are currently developing concepts of implementing this proposal with our atom chip.

It is also possible to use only magnetic fields for state-selective manipulation. For the  $|5^2S_{1/2}, F=1\rangle$  ground level of  $^{87}\text{Rb}$  the  $m_F = -1$  magnetic state is a low-field seeker. We can trap atoms in this state by turning off the repumper laser shortly before the end of the MOT phase (Section 3.2.1). First tests have demonstrated that we can evaporatively cool these atoms in the usual potential formed by the Cu-Z trap, down to  $T = 2\mu\text{K}$ . To increase the number of atoms, a different optical pumping beam is required with the correct polarization to accumulate atoms in the  $m_F = -1$  sublevel. Transitions between the two different levels can be induced by microwave radiation, this has recently been demonstrated on an atom chip [121]. We are currently planning the necessary hardware additions to our setup that will allow us to carry out this experiment.





# Bibliography

- [1] M. H. Anderson, J. R. Ensher, M. R. Matthews, C. E. Wieman, and E. A. Cornell. Observation of Bose-Einstein condensation in a dilute atomic vapor. *Science*, 269:198, 1995.
- [2] P. W. Anderson. Absence of diffusion in certain random lattices. *Phys. Rev.*, 109:1492, 1958.
- [3] E. Andersson, T. Calarco, R. Folman, M. Andersson, B. Hessmo, and J. Schmiedmayer. Multi mode interferometer for guided matter waves. *Phys. Rev. Lett.*, 88:100401, 2002.
- [4] M. Arndt, O. Nairz, J. Voss-Andreae, C. Keller, G. Van der Zouw, and A. Zeilinger. Wave-particle duality of  $C_{60}$  molecules. *Nature*, 401:680, 1999.
- [5] V. S. Bagnato, D. E. Pritchard, and D. Kleppner. Bose-Einstein condensation in an external potential. *Phys. Rev. A*, 35:4354, 1987.
- [6] J. Bardeen, L. N. Cooper, and J. R. Schrieffer. Theory of superconductivity. *Phys. Rev.*, 108:1175, 1957.
- [7] A. H. Barnett, S. P. Smith, M. Olshanii, K. S. Johnson, A. W. Adams, and M. Prentiss. Substrate-based atom waveguide using guided two-color evanescent light fields. *Phys. Rev. A*, 61:023608, 2000.
- [8] M. Bartenstein, A. Altmeyer, S. Riedl, S. Jochim, C. Chin, J. Hecker Denschlag, and R. Grimm. Crossover from a molecular Bose-Einstein condensate to a degenerate Fermi gas. *Phys. Rev. Lett.*, 92:120401, 2004.
- [9] C. Becker. *Eine neuartige magneto-optische Falle für Atomchip-Experimente*. Diploma thesis, Universität Heidelberg, 2002.
- [10] T. Bergeman, G. Erez, and H. J. Metcalf. Magnetostatic trapping fields for neutral atoms. *Phys. Rev. A*, 35:1535, 1987.
- [11] P. Berman, editor. *Atom Interferometry*, volume 37 of *Adv. At. Mol. Opt. Phys.* Academic Press, New York, 1997.

- [12] G. Birkel, F. B. J. Buchkremer, R. Dumke, and W. Ertmer. Atom optics with microfabricated optical elements. *Opt. Commun.*, 191:67, 2001.
- [13] C. J. Borde, A. Karasiewicz, and Ph. Tournenc. General relativistic framework for atomic interferometry. *Journal of Modern Physics D*, 3:157–161, 1994.
- [14] S. Bose. Plancks Gesetz und Lichtquantenhypothese. *Z. Phys.*, 26:178, 1924.
- [15] C. C. Bradley, C. A. Sackett, J. J. Tollett, and R. G. Hulet. Evidence of Bose-Einstein condensation in an atomic gas with attractive interactions. *Phys. Rev. Lett.*, 75:1687, 1995.
- [16] M. Brajdic. *Entwicklung einer Computersteuerung und ihre Anwendung in einem Experiment zur vereinfachten Bose-Einstein Kondensation in einer Oberflächenfalle*. Diploma thesis, Universität Heidelberg, 2003.
- [17] K. Brugger, P. Krüger, X. Luo, S. Wildermuth, H. Gimpel, M. Klein, S. Groth, R. Folman, I. Bar-Joseph, and J. Schmiedmayer. Two wire guides and traps with vertical bias field on atom chips. 2004. To be submitted to *Phys. Rev. A*.
- [18] E. Buks, R. Schuster, M. Heilblum, D. Mahalu, and V. Umansky. Dephasing in electron interference by ‘which-path’ detector. *Nature*, 391:871, 1998.
- [19] H. B. G. Casimir and D. Polder. The influence of retardation on the London-van der Waals forces. *Phys. Rev.*, 73:360, 1948.
- [20] D. Cassettari, B. Hessmo, R. Folman, T. Maier, and J. Schmiedmayer. Beam splitter for guided atoms. *Phys. Rev. Lett.*, 85:5483, 2000.
- [21] Y. Castin and R. Dum. Bose-Einstein condensates in time dependent traps. *Phys. Rev. Lett.*, 77:5315, 1996.
- [22] M. S. Chapman, T. D. Hammond, A. Lenef, J. Schmiedmayer, R. A. Rubenstein, E. Smith, and D. E. Pritchard. Photon scattering from atoms in an atom interferometer: Coherence lost and regained. *Phys. Rev. Lett.*, 75:3783, 1995.
- [23] D. G. Cory, R. Laflamme, E. Knill, L. Violay, T. F. Havel, N. Boulant, G. Boutis, E. Fortunato, S. Lloyd, R. Martinez, C. Negrevergne, M. Pravia, Y. Sharf, G. Teklemariam, Y. S. Weinstein, and W. H. Zurek. NMR based quantum information processing: Achievements and prospects. *Fort. Phys.*, 48:875, 2000.

- [24] K. B. Davis, M.-O. Mewes, M. R. Andrews, N. J. van Druten, D. S. Durfee, D. M. Kurn, and W. Ketterle. Bose-Einstein condensation in a gas of sodium atoms. *Phys. Rev. Lett.*, 75:3969, 1995.
- [25] K. B. Davis, M.-O. Mewes, M. A. Ioffe, M. R. Andrews, and W. Ketterle. Evaporative cooling of sodium atoms. *Phys. Rev. Lett.*, 74:5202, 1995.
- [26] K.B. Davis, M.-O. Mewes, and W. Ketterle. An analytical model for evaporative cooling of atoms. *Appl. Phys. B*, 60:155, 1995.
- [27] T. J. Davis. 2D magnetic traps for ultra-cold atoms: A simple theory using complex numbers. *Eur. Phys. J. D*, 18:27, 2002.
- [28] J. Denschlag, D. Cassettari, A. Chenet, S. Schneider, and J. Schmiedmayer. A neutral atom and a wire: towards mesoscopic atom optics. *Appl. Phys. B*, 69:291, 1999.
- [29] J. Denschlag, D. Cassettari, and J. Schmiedmayer. Guiding neutral atoms with a wire. *Phys. Rev. Lett.*, 82:2014, 1999.
- [30] S. Dettmer, D. Hellweg, P. Ryytty, J. J. Arlt, W. Ertmer, K. Sengstock, D. S. Petrov, G. V. Shlyapnikov, H. Kreutzmann, L. Santos, and M. Lewenstein. Observation of phase fluctuations in elongated Bose-Einstein condensates. *Phys. Rev. Lett.*, 87:160406, 2001.
- [31] D. Deutsch. Quantum theory, the Church-Turing principle and the universal quantum computer. *Proc. Roy. Soc. London, Ser. A*, 400:97, 1985.
- [32] M. Drndić, G. Zabow, C. S. Lee, J. H. Thywissen, M. Prentiss, K. S. Johnson, R. M. Westervelt, P. D. Featonby, V. Savalli, L. Cognet, K. Helmersson, N. Westbrook, C. I. Westbrook, W. D. Phillips, and A. Aspect. Properties of microelectromagnet mirrors as reflectors of cold Rb atoms. *Phys. Rev. A*, 60:4012, 1999.
- [33] R. Dumke, T. Mütther, M. Volk, W. Ertmer, and G. Birkl. Interferometer-type structures for guided atoms. *Phys. Rev. Lett.*, 89:220402, 2002.
- [34] S. Earnshaw. On the nature of the molecular forces which regulate the constitution of the luminiferous ether. *Trans. Camb. Phil. Soc.*, 7:97, 1842.
- [35] A. Einstein. Quantentheorie des einatomigen idealen gases. *Sitz. Ber. Preuss. Akad. Wiss.*, 1924.
- [36] B. Engeser. *Optische Abbildung einer atomaren Dichteverteilung*. Diploma thesis, Universität Heidelberg, 2002.

- [37] J. Estève, C. Aussibal, T. Schumm, C. Figl, D. Mailly, I. Bouchoule, C. I. Westbrook, and A. Aspect. The role of wire imperfections in micro magnetic traps for atoms. 2004. physics/043020.
- [38] P. O. Fedichev, M. W. Reynolds, and G. V. Shlyapnikov. Three-body recombination of ultracold atoms to a weakly bound s level. *Phys. Rev. Lett.*, 77:2921, 1996.
- [39] R. Folman, P. Krüger, D. Cassettari, B. Hessmo, T. Maier, and J. Schmiedmayer. Controlling cold atoms using nanofabricated surfaces: Atom chips. *Phys. Rev. Lett.*, 84:4749, 2000.
- [40] R. Folman, P. Krüger, J. Schmiedmayer, J. Denschlag, and C. Henkel. Microscopic atom optics: from wires to an atom chip. *Adv. At. Mol. Opt. Phys.*, 48:263, 2002.
- [41] J. Fortagh, H. Ott, S. Kraft, A. Günther, and C. Zimmermann. Surface effects in magnetic microtraps. *Phys. Rev. A*, 66:041604(R), 2002.
- [42] R. Frisch and E. Segrè. *Zeitung. für Physik*, 75:610, 1933.
- [43] H. Gauck, M. Hartl, D. Schneble, H. Schnitzler, T. Pfau, and J. Mlynek. Quasi-2D gas of laser cooled atoms in a planar matter waveguide. *Phys. Rev. Lett.*, 81:5298, 1998.
- [44] H. Gimpel. *Magnetische Oberflächenfallen für Atom-Interferometer*. Diploma thesis, Universität Heidelberg, 2002.
- [45] M. Girardeau. Relationship between systems of impenetrable bosons and fermions in one dimension. *J. Math. Ph.*, 1:516, 1960.
- [46] Y. V. Gott, M. S. Ioffe, and V. G. Tel'kovskii. *Nucl. Fusion Supplement*, 3:1045, 1962.
- [47] S. Gov, S. Shtrikman, and H. Thomas. Magnetic trapping of neutral particles: Classical and quantum-mechanical study of a Ioffe-Pritchard type trap. *J. Appl. Phys.*, 87:3989–3998, 2000.
- [48] M. Greiner, O. Mandel, T. Esslinger, T. W. Hänsch, and I. Bloch. Quantum phase transition from a superfluid to a Mott insulator in a gas of ultracold atoms. *Nature*, 415:39, 2002.
- [49] M. Greiner, C. A. Regal, and D. S. Jin. Emergence of a molecular Bose-Einstein condensate from a Fermi gas. *Nature*, 426:537, 2003.
- [50] R. Grimm, M. Weidemüller, and Y. B. Ovchinnikov. Optical dipole traps for neutral atoms. *Adv. At. Mol. Opt. Phys.*, 42:95, 2000.

- [51] S. Groth, P. Krüger, S. Wildermuth, R. Folman, T. Fernholz, D. Mahalu, I. Bar-Joseph, and J. Schmiedmayer. Atom chips: Fabrication and thermal properties. 2004. cond-mat/0404141.
- [52] L. K. Grover. Quantum mechanics helps in searching for a needle in a haystack. *Phys. Rev. Lett.*, 79:325, 1997.
- [53] T. L. Gustavson, A. Landragin, and M. A. Kasevich. Rotation sensing with a dual atom-interferometer sagnac gyroscope. *Classical Quantum Gravity*, 17:2385, 2000.
- [54] E. Haller. Diplomarbeit, Universität Heidelberg, to be published 2004.
- [55] W. Hänsel, P. Hommelhoff, T. W. Hänsch, and J. Reichel. Bose-Einstein condensation on a microelectronic chip. *Nature*, 413:498, 2001.
- [56] D. M. Harber, J. M. McGuirk, J. M. Obrecht, and E. A. Cornell. Thermally induced losses in ultra-cold atoms magnetically trapped near room-temperature surfaces. *J. Low. Temp. Phys.*, 133:229, 2003. cond-mat/0307546.
- [57] S. Haupt. *Setup of a New Experiment with Ultracold  $^{87}\text{Rb}$  Atoms: Towards Quantum Information Processing on an Atom Chip*. Diploma thesis, Universität Heidelberg, 2003.
- [58] C. Henkel and S. A. Gardiner. Decoherence of Bose-Einstein condensates in microtraps. *Phys. Rev. A*, 69:043602, 2004.
- [59] C. Henkel, P. Krüger, R. Folman, and J. Schmiedmayer. Fundamental limits for coherent manipulation on atom chips. *Appl. Phys. B*, 76:173, 2003.
- [60] C. Henkel, S. Pötting, and M. Wilkens. Loss and heating of particles in small and noisy traps. *Appl. Phys. B*, 69:379, 1999.
- [61] C. Henkel and M. Wilkens. Heating of trapped atoms near thermal surfaces. *Europhys. Lett.*, 47:414, 1999.
- [62] C. Henkel and M. Wilkens. Heating of trapped particles close to surfaces — blackbody and beyond. *Acta Phys. Slov.*, 50:293, 2000.
- [63] H. F. Hess. Evaporative cooling of magnetically trapped and compressed spin-polarized hydrogen. *Phys. Rev. B*, 34:3476, 1986.
- [64] E. A. Hinds, C. J. Vale, and M. G. Boshier. Two-wire waveguide and interferometer for cold atoms. *Phys. Rev. Lett.*, 86:1462, 2001.

- [65] C. Hock. Aufbau und Charakterisierung eines Resonators zur Detektion einzelner Atome. Master's thesis, University of Heidelberg, 2003. Diploma Thesis, University of Heidelberg.
- [66] M. J. Holland, C. Menotti, and L. Viverit. The role of boson-fermion correlations in the resonance theory of superfluids. 2004. cond- mat/ 0404234.
- [67] P. Horak, B. G. Klappauf, A. Haase, R. Folman, J. Schmiedmayer, P. Domokos, and E. A. Hinds. Possibility of single-atom detection on a chip. *Phys. Rev. A*, 67:043806, 2003.
- [68] O. Houde, D. Kadio, and L. Pruvost. Cold atom beam splitter realized with two crossing dipole guides. *Phys. Rev. Lett.*, 85:5543, 2000.
- [69] Y. Imry. *Introduction to Mesoscopic Physics*. Oxford University Press, Oxford, 1987.
- [70] S. Jochim, M. Bartenstein, A. Altmeyer, G. Hendl, S. Riedl, C. Chin, J. Hecker Denschlag, and R. Grimm. Bose-Einstein condensation of molecules. *Science Express*, 13 November 2003 (10.1126/science.1093280), 2003.
- [71] S. Jochim, M. Bartenstein, G. Hendl, J. Hecker Denschlag, R. Grimm, A. Mosk, and M. Weidemüller. Magnetic field control of elastic scattering in a cold gas of fermionic lithium atoms. *Phys. Rev. Lett.*, 89:273202, 2002.
- [72] J. B. Johnson. Thermal agitation of electricity in conductors. *Phys. Rev.*, 32:97–109, 1928.
- [73] M. P. A. Jones, C. J. Vale, D. Sahagun, B. V. Hall, and E. A. Hinds. Spin coupling between cold atoms and the thermal fluctuations of a metal surface. *Phys. Rev. Lett.*, 91:080401, 2003.
- [74] W. Ketterle, D. S. Durfee, and D. M. Stamper-Kurn. Making, probing and understanding Bose-Einstein condensates. In *Proceedings of the International School of Physics “Enrico Fermi” Ed. M. Inguscio, S. Stringari and C.E. Wieman*, page 67, IOS Press, Amsterdam, 1999.
- [75] P. Krüger. *Coherent matter waves near surfaces*. PhD thesis, 2004. PhD Thesis, University of Heidelberg.
- [76] P. Krüger, X. Luo, M. W. Klein, K. Brugger, A. Haase, S. Wildermuth, S. Groth, I. Bar-Joseph, R. Folman, and J. Schmiedmayer. Trapping and manipulating neutral atoms with electrostatic fields. *Phys. Rev. Lett.*, 91:233201, 2003.

- [77] A. E. Leanhardt, A. P. Chikkatur, D. Kielpinski, Y. Shin, T. L. Gustavson, W. Ketterle, and D. E. Pritchard. Propagation of Bose-Einstein condensates in a magnetic waveguide. *Phys. Rev. Lett.*, 89:040401, 2002.
- [78] A. E. Leanhardt, Y. Shin, A. P. Chikkatur, D. Kielpinski, W. Ketterle, and D. E. Pritchard. Bose-Einstein condensates near a microfabricated surface. *Phys. Rev. Lett.*, 90:100404, 2003.
- [79] A. Lenef, T. D. Hammond, E. T. Smith, M. S. Chapman, R. A. Rubenstein, and D. E. Pritchard. Rotation sensing with an atom interferometer. *Phys. Rev. Lett.*, 78:760, 1997.
- [80] I. Lesanovsky. Rydberg-Atome in magnetischen Quadrupol-Fallen. Master's thesis, 2003. Diploma Thesis, Universität Heidelberg.
- [81] I. Lesanovsky. 2004. In preparation.
- [82] I. Lesanovsky, J. Schmiedmayer, and P. Schmelcher. Rydberg atoms in magnetic quadrupole traps. *Euro. Phys. Lett.*, 65, 4:478, 2003.
- [83] B. Lev. Fabrication of micro-magnetic traps for cold neutral atoms. *Quant. Inf. Comp.*, 3:450–464, 2003. quant-ph/0305067.
- [84] Y. Lin, I. Teper, C. Chin, and V. Vuletić. Impact of the Casimir-Polder potential and Johnson noise on Bose-Einstein condensate stability near surfaces. *Phys. Rev. Lett.*, 92:050404, 2004.
- [85] R. Long, T. Steinmetz, P. Hommelhoff, W. Hänsel, T. W. Hänsch, and J. Reichel. Magnetic microchip traps and single atom detection. *Phil. Trans. R. Soc. Lond. A*, 361:1375, 2003.
- [86] O. J. Luiten, M. W. Reynolds, and J. T. M. Walraven. Kinetic theory of the evaporative cooling of a trapped gas. *Phys. Rev. A*, 53:381, 1996.
- [87] X. Luo, P. Krüger, K. Brugger, S. Wildermuth, H. Gimpel, M. Klein, S. Groth, R. Folman, I. Bar-Joseph, and J. Schmiedmayer. An atom fiber for guiding cold neutral atoms. 2004. quant-ph/0311174.
- [88] E. Majorana. Atomi orientati incampo magnetico variabile. *Nuovo Cimento*, 9:43, 1932.
- [89] O. Mandel, M. Greiner, A. Widera, T. Rom, T. W. Hänsch, and I. Bloch. Controlled collisions for multi-particle entanglement of optically trapped atoms. *Nature*, 425:937–940, 2003.
- [90] I. Marcikic, H. de Riedmatten, W. Tittel, H. Zbinden, and N. Gisin. Long-distance teleportation of qubits at telecommunication wavelengths. *Nature*, 421:509, 2003.

- [91] J. M. McGuirk, D. M. Harber, J. M. Obrecht, and E. A. Cornell. Alkali adsorbate polarization on conducting and insulating surfaces probed with Bose-Einstein condensates. *cond-mat/0403254*, 2004.
- [92] C. Menotti, J. R. Anglin, J. I. Cirac, and P. Zoller. Dynamic splitting of a Bose-Einstein condensate. *Phys. Rev. A*, 63:023601, 2001.
- [93] H. J. Metcalf. *Laser Cooling and Trapping*. Springer Verlag, Heidelberg Berlin New York, 1999.
- [94] A. L. Migdall, J. V. Prodan, W. D. Phillips, T. H. Bergeman, and H. J. Metcalf. First observation of magnetically trapped neutral atoms. *Phys. Rev. Lett.*, 54:2596, 1985.
- [95] A. J. Moerdijk and B. J. Verhaar. Collisional two- and three-body decay rates of dilute quantum gases at ultralow temperatures. *Phys. Rev. A*, 53:R19, 1996.
- [96] A. Negretti, T. Calarco, and C. Henkel. Unpublished, 2004.
- [97] H. Nyquist. Thermal agitation of electric charge in conductors. *Phys. Rev.*, 32:110–113, 1928.
- [98] D. O’Dell, S. Giovanazzi, G. Kurizki, and V. M. Akulin. Bose-Einstein condensates with  $1/r$  interatomic attraction: Electromagnetically induced “gravity”. *Phys. Rev. Lett.*, 84:5687, 2000.
- [99] M. Olshanii. Atomic scattering in the presence of an external confinement and a gas of impenetrable bosons. *Phys. Rev. Lett.*, 81:938, 1998.
- [100] H. Ott, J. Fortagh, G. Schlotterbeck, A. Grossmann, and C. Zimmermann. Bose-Einstein condensation in a surface microtrap. *Phys. Rev. Lett.*, 87:230401, 2001.
- [101] B. Parades, A. Widera, V. Murg, O. Mandel, S. Fölling, I. Cirac, G. V. Shlyapnikov, T. W. Hänsch, and I. Bloch. Tonks-Girardeau gas of ultracold atoms in an optical lattice. *Nature*, 429:277, 2004.
- [102] A. Peters, K. Y. Chung, and S. Chu. Measurement of gravitational acceleration by dropping atoms. *Nature*, 400:849, 1999.
- [103] C. J. Pethick and H. Smith. *Bose-Einstein Condensation in Dilute Gases*. Cambridge University Press, 2002.
- [104] W. Petrich, M. H. Anderson, J. R. Ensher, and E. A. Cornell. A stable, tightly confining magnetic trap for evaporative cooling of neutral atoms. *Phys. Rev. Lett.*, 74:3352, 1995.



- [105] D. S. Petrov, G. V. Shlyapnikov, and J. T. M. Walraven. Regimes of quantum degeneracy in trapped 1D gases. *Phys. Rev. Lett.*, 85:3745, 2000.
- [106] D. S. Petrov, G. V. Shlyapnikov, and J. T. M. Walraven. Phase-fluctuating 3D Bose-Einstein condensates in elongated traps. *Phys. Rev. Lett.*, 87:050404, 2001.
- [107] D. Pritchard. Cooling neutral atoms in a magnetic trap for precision spectroscopy. *Phys. Rev. Lett.*, 51:1336, 1983.
- [108] E. L. Raab, M. Prentiss, A. Cable, S. Chu, and D. E. Pritchard. Trapping of neutral sodium atoms with radiation pressure. *Phys. Rev. Lett.*, 59:2631, 1987.
- [109] J. Reichel. Microchip traps and Bose-Einstein condensation. *Appl. Phys. B*, 74:469, 2002.
- [110] J. Reichel, W. Hänsel, and T. W. Hänsch. Atomic micromanipulation with magnetic surface traps. *Phys. Rev. Lett.*, 83:3398, 1999.
- [111] J. Reichel and J. H. Thywissen. Using magnetic chip traps to study tonks-girardeau quantum gases. arXiv:cond-mat/0310330 (2003).
- [112] L. E. Reichl. *A Modern Course In Statistical Physics*. John Wiley & Sons, 1998.
- [113] P. Rosenbusch, B. V. Hall, I. G. Hughes, C. V. Saba, and E. A. Hinds. Manipulation of cold atoms using a corrugated magnetic reflector. *Phys. Rev. A*, 61:31404(R), 2000.
- [114] S. Schneider. *Bose-Einstein Kondensation in einer magnetischen Z-Falle*. PhD thesis, Universität Heidelberg, 2003.
- [115] P. W. Shor. Algorithms for quantum computation: Discrete logarithms and factoring. *Proceedings of the 35th Annual Symposium on Foundations of Computer Science, IEEE Comput. Soc. Press*, page 124, 1994.
- [116] R. J. C. Spreeuw, D. Voigt, B. T. Wolschrijn, and H. B. van Linden van den Heuvell. Creating a low-dimensional quantum gas using dark states in an inelastic evanescent-wave mirror. *Phys. Rev. A*, 61:053604, 2000.
- [117] L. Stodolsky. Matter and light wave interferometry in gravitational fields. *General Relativity and Gravitation*, 11:391–405, 1979.
- [118] C. V. Sukumar and D. M. Brink. Spin-flip transitions in a magnetic trap. *Phys. Rev. A*, 56:2451, 1997.

- [119] T. Calarco, E. A. Hinds, D. Jaksch, J. Schmiedmayer, J. I. Cirac, and P. Zoller. Quantum gates with neutral atoms: Controlling collisional interactions in time-dependent traps. *Phys. Rev. A*, 61:022304, 2000.
- [120] L. Tonks. The complete equation of state of one, two and three-dimensional gases of hard elastic spheres. *Phys. Rev.*, 50:955, 1936.
- [121] P. Treutlein, P. Hommelhoff, T. Steinmetz, T. W. Hänsch, and J. Reichel. Coherence in Microchip Traps. *Phys. Rev. Lett.*, 92:203005, 2004.
- [122] M. Vengalattore, W. Rooijakkers, and M. Prentiss. Ferromagnetic atom guide with in situ loading. *Phys. Rev. A*, 66:053403, 2002.
- [123] D.-W. Wang, M. D. Lukin, and E. Demler. Disordered Bose-Einstein condensates in quasi-one-dimensional magnetic microtraps. *Phys. Rev. Lett.*, 92, 2004.
- [124] J. D. Weinstein and K. G. Libbrecht. Microscopic magnetic traps for neutral atoms. *Phys. Rev. A*, 52:4004, 1995.
- [125] S. Wildermuss and P. Kröger. Universal lab rule 3. 2003.
- [126] S. Wildermuth, P. Krüger, C. Becker, M. Brajdic, S. Haupt, A. Kasper, R. Folman, and J. Schmiedmayer. Optimized mageto-optical trap for experiments with ultracold atoms near surfaces. *Phys. Rev. A*, 69:030901(R), 2004.
- [127] M. Wilzbach. PhD thesis, Universität Heidelberg, to be published 2005.
- [128] W. H. Wing. On neutral particle trapping in quasistatic electromagnetic fields. *Prog. Quant. Electr.*, 8:181, 1984.